RICE UNIVERSITY

Geometrical Optics for Quasi-P Waves: Theories and Numerical Methods

by

Jianliang Qian

A Thesis Submitted
in Partial Fulfillment of the
Requirements for the Degree

Doctor of Philosophy

Approved, Thesis Committee:

William W. Symes
Professor, Chair
Computational & Applied Mathematics

Steven J. Cox
Professor
Computational & Applied Mathematics

Matthias Heinkenschloss
Associate Professor
Computational & Applied Mathematics

Liliana Borcea
Assistant Professor
Computational & Applied Mathematics

Colin A. Zelt
Assistant Professor
Geology and Geophysics

Houston, Texas

April, 2000

Abstract

Geometrical Optics for Quasi-P Waves: Theories and Numerical Methods

by

Jianliang Qian

The quasi-P wave in anisotropic solids is of practical importance in obtaining maximal imaging resolution in seismic exploration. The geometrical optics term in the asymptotic expansion for the wave characterizes the high frequency part of the quasi-P wave by using two functions: a phase (traveltime) function satisfying an eikonal equation and an amplitude function satisfying a transport equation.

I develop theories and numerical methods for constructing the geometrical optics term of quasi-P waves in general anisotropic solids. The traveltime corresponding to the downgoing wave satisfies a paraxial eikonal equation, an evolution equation in depth. This paraxial eikonal equation takes into account the convexity of the quasi-P slowness surface and thus has a built-in reliable indicator of the ray velocity direction. Therefore, high-order finite-difference eikonal solvers are easily constructed by utilizing Weighted Essentially NonOscillating (WENO) schemes.

Because the amplitude function is related to second-order derivatives of the traveltime, a third-order accurate eikonal solver for traveltimes is necessary to get a first-order accurate amplitude. However, the eikonal equation with a point source has an upwind singularity at the source which renders all finite-difference eikonal solvers

to be first-order accurate near the source. A new approach combining an adaptive-gridding strategy with WENO schemes can treat this singularity efficiently and can yield highly accurate traveltimes and amplitudes for both isotropic and anisotropic solids.

A variety of numerical experiments verify that the new paraxial eikonal solver and adaptive-gridding-WENO approach are accurate and efficient for capturing the anisotropy. Therefore, the two new methods provide tools for constructing the geometrical optics term of the quasi-P wave in general anisotropic solids.

Acknowledgments

There are many people I would like to acknowledge for support and help throughout my stay at Rice University. My supervisor Bill Symes has helped me tremendously by sharing his knowledge, intuition and enthusiasm for mathematics. During his sabbatical year at Stanford Exploration Project (September, 1998 to August, 1999), he invited me to study with him at Stanford University. Without his support and supervision, I couldn't have had four years of happy and fruitful stay at Rice and Stanford. I am very grateful to him for all of these. My thesis committee members, Dr. Steven Cox, Dr. Matthias Heinkenschloss, Dr. Liliana Borcea and Dr. Colin Zelt, have also helped me over the past years and I thank them for their willingness to serve as my committee members.

I dedicate this dissertation to my wife Xijun (Lucy) Lu for her love, patience and understanding. To my parents, siblings and teachers (especially Prof. Jiaqi Liu), I am grateful for the love and care they have given me. I also thank Dr. Jan Hewitt who helped me edit this dissertation.

I have been fortunate to be a member of The Rice Inversion Project (TRIP). I have benefited from interaction with various current or former members of TRIP: Chaoming Zhang, Seongjai Kim, Senren Liu, S. Minkoff, Hua Song, M. Gockenbach, K. Araya, C. Nolan, Nate Winslow, Shannon Scott, D. Williams, R. Hill, Z. Castillo, P. Ecoublet. Dr. Chaoming Zhang has always treated me like his young brother, and I will remember what he has done for me. Dr. Seongjai Kim has always encouraged me to push forward my research and develop my academic career, and I will never forget his kind comments and criticism.

My stay as a visiting scholar at Stanford from September, 1998 to June, 1999 is an invaluable experience for me, therefore I would like to thank my host Prof. Jon Claerbout for his courtesy. Also I would like to thank M. Brown, N. Chemingui, R. Clapp, S. Crawley, S. Fomel, A. Guitton, M. Prucha, J. Rickett, Yalei Sun, L. Valliant, Yi Zhao, and Haibin Xu for their help during my stay at Silicon Valley.

In addition, I would like to thank Dr. Hongkai Zhao, Dr. Bee Bednar and Dr. Joe Dellinger for a lot of fruitful discussion, Dr. Steven Ruuth and Dr. Dangping Peng for kindly answering my technical questions.

This work was partially supported by the National Science Foundation under grant numbers DMS 9627355, the Office of Naval Research under grant number N00014-96-1-0156, the U. S. Department of Energy under grant number DE-FG07-97 ER14827 and The Rice Inversion Project. TRIP Sponsors for 1999 are Amerada Hess, Amoco Research, Conoco Inc., Exxon Production Research Co., Geophysical Development Corporation, Landmark Graphics, Mobil, and Western Geophysical.

Contents

Tables

Illustrations

To my wife Lucy Lu and my parents.

Chapter 1

Introduction

In modern seismic exploration for hydrocarbon reserves, one takes surface reflection surveys at increasingly larger distances both for image enhancement and for improved estimation of elastic parameters. However, in order to obtain a better imaging resolution as well as better understanding of the subsurface structure from solving inverse problems (i.e., inverting these surface reflection data), one must take into consideration the anisotropy at different length scales in the subsurface because shales are almost always anisotropic, and they make up over 70 percent of hydrocarbon exploration targets.

Two kinds of techniques are used to solve these inverse problems: one is the search-based iterative (optimization) techniques (Tarantola [Tar86], Mora [Mor89], Symes and Kern [SK94], Debski and Tarantola [DT95]); the other is the direct linearized method which seeks direct, closed-form solutions (Beylkin [Bey85], Beylkin and Burridge [BB90], Symes et. al. [SVST94], Burridge et. al. [BdHMS98], de Hoop et. al. [dHSB99]). Because the computation cost of the direct linearized method is cheaper than that of the search-based optimization technique, the industry favors the direct linearized inversion method. To construct the closed-form expressions for the inverse problem solution, the majority of the direct methods utilize the Born (or Rytov) approximation and the asymptotic ray theory to model the wave scattering and propagation (de Hoop et. al. [dHSB99]). Solutions are then obtained by mappings, such as generalized Radon transform (GRT), which require further asymptotic approximations (de Hoop and Bleistein [dHB97], Symes [Sym95]). Because the asymptotic theory originated in the field of geometrical optics (Born and

Wolf [BW64]), the better way to understand this is to put it in the context of geometrical optics. In the first place, the relation between the geometrical optics and the asymptotic method is reviewed.

1.1 Geometrical optics and asymptotic methods for wave equations

What is the geometrical optics? Born and Wolf ([BW64], p 109) defined the **geometrical optics** as "the branch of optics which is characterized by the neglect of the wavelength, i.e. that corresponding to the limiting case (wavelength) $\lambda_0 \to 0$, since in this approximation the optical laws may be formulated in the language of geometry." This definition is based on the short wavelength assumption of light and can be generalized to deal with other wave phenomena as well. The linear or nonlinear partial differential equations describing these wave propagations involve a parameter, such as the wavelength λ, which is small compared to all other lengths in the problem (Keller and Lewis [KL95], White [Whi99]). The **asymptotic method** is for the asymptotic solution of partial differential equations governing these wave propagations (Keller and Lewis [KL95]).

The asymptotic method is based on progressing wave expansions (Courant and Hilbert [CH62]) and is used to construct an asymptotic expansion of the solution which is valid near $\lambda = 0$ ("short wavelength"), or equivalently for the wave number $k = \dfrac{2\pi}{\lambda}$ near infinity ("high frequency") (Keller and Lewis [KL95]). Because, on the one hand, the solutions of these equations oscillate with the small wavelength λ; on the other hand, the short wavelength λ may be thousands of times smaller than the length scale of interest, it is often expensive and impractical to find these solutions by direct numerical discretizations of the related partial differential equations.

The progressing wave expansion for the asymptotic method involves a "phase function" and an infinite sequence of "amplitude functions." The phase function satisfies a nonlinear partial differential equation of first-order called the eikonal equation; the amplitude functions satisfy a sequence of successive "transport equations" (Courant and Hilbert [CH62], Keller and Lewis [KL95]). The leading term in the progressing wave expansion can be constructed in terms of quantities which occur in the geometrical optics; therefore, the leading term is called the **geometrical optics term** by Keller and Lewis [KL95]. The asymptotic method has been successfully used to construct the asymptotic solution for acoustic wave equations (Keller and Lewis [KL95], Symes [Sym95]), deep-water wave equations (White [Whi99]), Maxwell's equations (Born and Wolf [BW64], Cornbleet [Cor83], Keller and Lewis [KL95]) and linear elastodynamic wave equations (Fedorov [Fed68], Musgrave [Mus70], Cerveny [Cer72], Berryman [Ber79], Burridge et. al. [BdHMS98], de Hoop et. al. [dHSB99], Fuki et. al. [FKN98]).

For the linear elastodynamic wave equation in elastic anisotropic solids, three different waves, i.e., quasi-longitudinal (**quasi-P**) and two transverse waves, are coupled together (Fedorov [Fed68], Musgrave [Mus70]). Because the quasi-P wave is of practical importance in obtaining maximal imaging resolution in seismic exploration (Thomsen [Tho86], Tsvankin and Thomsen [TT95], Anderson [And96], Pratt and Chapman [PC92], Cherret and Singh [CS98]), this dissertation is devoted to developing theories and numerical methods for constructing the geometrical optics term (the leading term) in the asymptotic expansions for quasi-P waves in anisotropic solids, where the phase function is the so-called **traveltime**.

To obtain the phase and amplitude function, I will solve the quasi-P eikonal and transport equations by finite-difference methods.

1.2 Finite-difference methods for quasi-P eikonal equations

The eikonal equation can be solved by the method of characteristics (Courant and Hilbert [CH62], Evans [Eva94]) which constructs the characteristic curves called "rays." The phase (traveltime) function and the amplitude function satisfy linear ordinary differential equations along the rays. The methods based on the characteristic equations are called "ray-tracing methods" (Cerveny [Cer72], Shearer and Chapman [SC88], Pereyra [Per92]), and they work for both **isotropic** and **anisotropic** solids. But ray-tracing methods have some drawbacks. The nonuniform distribution of traveltime data from ray-tracing methods gives rise to cumbersome and expensive interpolations for the application in seismic imaging. Therefore, many researchers appeal to finite-difference methods for solving the eikonal equation directly on regular Cartesian grids.

The finite-difference eikonal solvers compute the approximate first-arrival times directly on a prespecified grid, involve rather simple data structures, and are easy to code efficiently (Reshef and Kosloff [RK86], Vidale [Vid88], van Trier and Symes [vTS91], Schneider et. al [SRBK92], Qin et. al. [QLO+92], Schneider [Sch95], El-Mageed [EM96], Sethian and Popvicci [SP99], Kim and Cook [KC99]). However, the methods cited describe only finite-difference traveltime algorithms for isotropic solids. Extension of these methods to anisotropic wave propagations is not entirely straightforward. Qin and Schuster [QS93] and Eaton [Eat93] extended the expanding-wavefront scheme developed by Qin et. al. [QLO+92] to the anisotropic medium; but their extensions work only for 2-D cases and have first-order accuracy only.

The finite-difference eikonal solvers mentioned above depend on the fact that for isotropic media the ray velocity vector, i.e., the *group velocity*, has the same direction as the traveltime gradient, i.e., the *phase velocity*, so that we can use the traveltime gradient as a reliable indicator of energy flow (and thus causality, a.k.a stability) in extrapolating the traveltime field. However, this is not true for anisotropic media (Dellinger and Symes [DS97]). One of the goals of this dissertation is establishing a reliable indicator of quasi-P ray velocity direction for finite-difference eikonal solvers by formulating a relation between the group velocity direction and the phase velocity direction. Furthermore, the dissertation will present theoretical formulations, implementation details, and illustrative applications of finite-difference methods for traveltimes of first-arriving quasi-P waves in heterogeneous anisotropic solids.

The mathematical foundation of the finite difference approach to traveltime computation is the observation of Lions [Lio82]: the first-arrival traveltime is a generalized solution of the eikonal equation. A generalized solution concept is necessary because the eikonal equation does not generally have solutions in the ordinary sense throughout its domain. However, generalized solutions are not unique because of the existence of several branches of traveltime in the presence of strong refraction. Lions and others abstractly characterized a particular generalized solution, the so-called **viscosity solution**, which turns out to be the first-arrival. Because of its stability with respect to the medium parameters and the source location, this generalized solution is computable by finite-difference approximation.

Lions' findings [Lio82] pertain to isotropic media, but the central hypothesis of this dissertaion is that the first-arrival quasi-P traveltime is also a stable generalized solution and therefore computable by suitable finite-difference schemes. Also by analogy with the isotropic case, the so-called upwind scheme is expected to be particularly successful. Dellinger and Symes [Del91] [DS97] investigated this possibility but did not give full details of a workable algorithm. This dissertation presents a family of workable algorithms of Essentially NonOscillatory (ENO) type (Osher and Sethian [OS88], Osher and Shu [OS91]), applied to a depth-evolution ("paraxial") form of the eikonal equation. The computed solution gives an accurate approximation of the traveltime at every point of a Cartesian grid, which is connected to the source by a first-arriving ray whose velocity vector makes an angle less than a prescribed angle with the vertical. A similar approach has proven quite successful for the isotropic traveltime (and amplitude) computation for use in prestack modeling, migration, and inversion for seismic data processing (Symes et. al. [SVST94], El-Mageed [EMKS97], Qian et. al. [QBS99]).

Because the transport equation for the amplitude in the geometrical optics term involves the second-order derivatives of the phase (traveltime) function, which in turn is obtained by numerical computations, it follows that to obtain first-order accurate amplitudes the computed traveltime function itself must have at least third-order accuracy. However, the eikonal equation with a point source has an upwind singularity at the source. To obtain highly accurate traveltime functions, I have to treat this singularity first.

1.3 Adaptive treatment for the upwind singularity at the source

The traveltime field is mostly smooth, and the use of upwind differencing in the eikonal solvers confines the errors due to singularities which develop away from the source point (Reshef and Kosloff [RK86], Vidale [Vid88], van Trier and Symes [vTS91], Schneider et. al [SRBK92], Schneider [Sch95], El-Mageed [EM96], Sethian and Popvicci [SP99], Kim and Cook [KC99]). The source point itself is, however, also an upwind singularity. The truncation error of a pth order method is dominated by the product of $(p+1)$st derivatives of the traveltime field and the $(p+1)$st power of the step(s). The $(p+1)$st derivatives of the traveltime field, however, behave like the $(-p+1)$th power of the distance to the source. Therefore, near the source – when the distance is on the order of the step – the truncation error is quadratic in the step, i.e., first-order. This inaccuracy spreads throughout the computation and renders all higher-order methods first-order convergent. Moreover, the resultant inaccuracy in traveltimes prevents reliable computation of auxiliary quantities such as takeoff angles and amplitudes.

This inaccuracy afflicts all point source traveltime computations using gridded eikonal solvers. In the few published convergence tests, implementers have resorted to imposing a grid-independent region of constant velocity near the source, in which the traveltimes are initialized analytically. This is the approach taken, for instance, by Sethian [Set99b] in demonstrating second-order convergence for a version of his fast marching method. This approach has two obvious drawbacks: (1) the velocity may not be homogeneous near the source; and (2) the size of the region of analytic computation must be set by the user and bears no obvious relation to the grid parameters. In principle, highly accurate ray-tracing methods could be used to alleviate the first difficulty, but the second remains: it introduces a "magic number" into the use of eikonal solvers. Kim and Cook [KC99] take a different approach, similar to the one we advocate: they refine the grid several times near the source so that the reduced grid spacing compensates for the increased truncation error. However, their grid refinement strategy appears to be *ad-hoc*, and once again involves a "magic number," namely the number of grid refinements near the source, without a clearcut selection criterion.

In this dissertation, I show how to use adaptive-gridding concepts commonplace in the numerical solution of ordinary differential equations (Gear [Gea71]) to resolve the difficulty caused by this inaccuracy, for both isotropic and anisotropic media. The adaptive-gridding has already been used in numerical solutions of PDEs (Berger and Oliger [BO84], Berger and LeVeque [BL97]). Generally, the grid refinement must be localized in several dimensions, leading to complex data structures. Fortunately, the nature of the traveltime field for isotropic media permits a relatively straightforward adaptive-gridding strategy as first established in Belfi and Symes [BS98]. I improve the algorithm of Belfi and Symes through the use of the more accurate Weighted Essentially NonOscillating (WENO) difference schemes and extend it to solutions of advection equations for various geometrical optics quantities in both isotropic and anisotropic media. The efficiencies achieved by the adaptive-gridding are considerable – usually more than an order of magnitude reduction in computation time for problems of typical exploration size, compared to the fixed-grid method giving the same level of accuracy. I also obtain significant improvements in the accuracy of computed geometrical optics quantities, such as takeoff angles and geometrical amplitudes.

The essential principle of the adaptive gridding is simple and is based on a hierarchy of difference schemes of various orders. Presumably a higher-order step is more accurate than a lower-order step, so that the higher-order step can serve as a substitute for the exact solution in evaluating the local error in the lower-order step. Therefore, one can combine the step computations of two different orders to obtain a so-called *a posteriori* estimate of the truncation error for the lower-order step. Since the lower- and higher- order truncation errors stand in a known asymptotic relation, this permits an estimate of the higher-order truncation error as well. The asymptotic form of the truncation error then permits prediction of a step that will result in a lower-order truncation error less than a user-specified tolerance. So long as the steps are selected to maintain this local error, standard theory predicts that the higher-order global error, i.e., the actual error in the solution computed using the higher-order scheme, will be proportional to the user-specified tolerance. This straightforward idea is embedded in most modern software packages for solutions of ordinary differential equations (Gear [Gea71]). Its use for partial differential equations is a little more complicated because it is usually necessary to adjust the grid of the non-evolution variables along with the evolution step. However, as shown by computational experiments in Belfi and Symes [BS98], the solution of the (paraxial) eikonal equation changes in a sufficiently predictable way to make grid adjustment practical.

1.4 Outline of the dissertation

This chapter has given an overview of geometrical optics and asymptotic methods for wave propagations and how the geometrical optics term is computed in seismic explorations. Because of its practical importance, the finite-difference method for computing the geometrical optics term is emphasized. The difficulties are identified in designing finite-difference schemes for general anisotropic solids, i.e., the reliable indicator of the group velocity direction and the upwind singularity at the point source. To overcome these difficulties I propose a paraxial eikonal equation which has a built-in indicator of the group velocity direction for quasi-P waves and an adaptive-gridding WENO approach to treating the upwind singularity at the source. The rest of the dissertation is devoted to constructing paraxial eikonal equations, developing new algorithms for solving these equations, implementing these algorithms and the new adaptive-gridding WENO approach, and verifying these new numerical methods on various anisotropic solids.

Chapter 2 presents the theories of the geometrical optics for quasi-P waves in anisotropic solids. In section 2.1, the eikonal equation for traveltimes and the transport equation for amplitudes are derived by applying the high frequency asymptotics to the linear elastic wave equations. Section 2.2 constructs the paraxial eikonal equation for the quasi-P wave traveltime by making use of the convexity of the slowness surface, and the existence of the construction is proved in Appendix A. Section 2.3 derives the amplitude formula in Cartesian coordinates from the one in ray coordinates, including two new advection equations for ray parameters.

Chapter 3 describes the numerical methods of the geometrical optics for quasi-P waves in anisotropic solids. Section 3.1 presents algorithms for computing the paraxial Hamiltonian needed in solving the paraxial eikonal equation, along with a new algorithm for initializing traveltimes in finite-difference schemes. Section 3.2 gives a new derivation of a first-order Godunov scheme by using a local paraxial ray-tracing technique. Section 3.3 details high-order ENO and WENO finite-difference schemes, which are used to solve the paraxial eikonal equation for traveltimes and the advection equation for take-off angles.

In Chapter 4, the theories and numerical methods developed in Chapters 2 and 3 are applied to solving the paraxial eikonal equation in transversely isotropic (TI) solids. Section 4.1 gives a simplified paraxial Hamiltonian for TI solids with a vertical symmetry axis (VTI). Section 4.2 builds an inclined TI (ITI) model by rotating a VTI model. In Section 4.3, extensive numerical experiments are performed to verify the feasibility of the theory and the efficiency and accuracy of the numerical algorithms, including examples for 2-D VTI solids, 3-D VTI solids, and isotropic and anisotropic Marmousi models. Because of the generality of inclined TI solids, Section 4.4 consisting of numerical examples for ITI solids is specialized in illustrating the efficiency and accuracy of the algorithms developed in Chapter 3 for general anisotropic solids.

In Chapter 5, the adaptive-gridding WENO approach is proposed to compute the amplitude function in isotropic and VTI solids. Section 5.1 formulates the geometrical optics term for isotropic solids, including the paraxial eikonal equation for traveltimes and the advection equation for take-off angles. Section 5.2 briefly mentions the high-order WENO schemes for traveltimes and take-off angles, with details presented in

Chapter 3 and Appendix C. Section 5.3 describes in detail the adaptive-gridding WENO approach for the upwind singularity at the source, including an algorithm framework. In Section 5.4, some numerical experiments are performed to show that the adaptive-gridding WENO approach is efficient and accurate. In Section 5.5 and 5.6, the adaptive-gridding WENO approach is applied to computing the traveltime and amplitude in VTI solids, along with some examples showing that the approach works for anisotropic solids as well.

Finally, Chapter 6 concludes the dissertation, summarizing contributions of the dissertation and suggesting some research directions which merit further investigation.

Chapter 2

Geometrical Optics for Quasi-P Waves: Theories

In velocity structures with mild lateral heterogeneity, most reflected wave energy propagates down to the target, then up to the surface. That is, the energy in such a wavefield propagates along downgoing rays: the x_3 ("z") component of the ray velocity vector remains positive from source to target. The traveltime along such downgoing rays increases with depth and should be the solution of an evolution system in depth. For isotropic wave propagation, Gray and May [GM94] suggest modifying the eikonal equation in such a way that (i) the modified equation defines a depth evolution of traveltime, and (ii) solutions of the modified and original eikonal equation are identical at every point connected to the source by a first-arriving ray making a angle with the vertical less than 90 degrees. The principal purpose of this chapter is to explain such a modification, resulting in a *paraxial eikonal equation*, for anisotropic wave propagation. Solving the paraxial eikonal equation yields the phase function for the geometrical optics term. To finish the construction of geometrical optics term, two new advection equations for ray parameters have to be solved to obtain the amplitude term.

2.1 High frequency asymptotics

In this section the Einstein summation convention is assumed (Musgrave [Mus70]).

Hooke's law states that stress σ_{ij} is related to strain e_{kl} by a stiffness tensor C_{ijkl},

$$\sigma_{ij} \quad = \quad C_{ijkl} e_{kl}.$$

Therefore, the motion equation without body force is

$$\rho \frac{\partial^2 \mathbf{U}}{\partial t^2} = \nabla \cdot \sigma, \tag{2.1}$$

where $\mathbf{U} = (U_i)$ is the displacement vector.

By the symmetry of the stiffness tensor, the motion (wave) equation is

$$\rho \frac{\partial^2 U_j}{\partial t^2} = \frac{\partial}{\partial x_i}(C_{ijkl} \frac{\partial U_k}{\partial x_l}). \tag{2.2}$$

The progressing wave expansion (Courant and Hilbert [CH62]; Cerveny [Cer72]; Burridge et. al. [BdHMS98]) assumes that the solution is of the form

$$\begin{aligned} \mathbf{U}(x,t) &= \sum_{n=0}^{\infty} \mathbf{A}^{(n)}(\mathbf{x}) f_n(t - \tau(\mathbf{x})), \\ f'_{n+1} &= f_n, \end{aligned} \tag{2.3}$$

where the wavefront is

$$t = \tau(\mathbf{x}). \tag{2.4}$$

Upon inserting the *ansatz* (2.3) into the wave equation and equating individual coefficients of f_{n-2} to zero successively, starting with the most singular term $n = 0$, I have a recursive system for the phase τ and amplitudes $\mathbf{A}^{(n)}$. Because the **geometrical optics** term consisting of the phase and amplitude function is determined by the zeroth-order term ($n = 0$) and the first-order term ($n = 1$), I am interested in only these two terms.

Equating the zeroth-order term to zero gives rise to the Christoffel's equation,

$$(\Gamma_{jk} - \delta_{jk}) A_k^{(0)} = 0, \tag{2.5}$$

which leads to the eikonal equation for the phase function τ,

$$\begin{aligned} \det(\Gamma_{jk} - \delta_{jk}) &= 0, \\ \det(a_{ijkl} p_i p_l - \delta_{jk}) &= 0, \end{aligned} \tag{2.6}$$

where $\mathbf{p} = (p_i) = \nabla\tau$ is the slowness vector normal to the wavefront (2.4); τ is the traveltime or phase of the wave mode; $a_{ijkl} = \dfrac{C_{ijkl}}{\rho}$ are the density-normalized elastic parameters; $\Gamma_{jk} = a_{ijkl}p_ip_l$; δ_{jk} is the Kronecker delta, $\delta_{jk} = 1$ if $j = k$, $\delta_{jk} = 0$ otherwise. Note that all of these quantities depend on the spatial coordinate vector $\mathbf{x} = (x_1, x_2, x_3)$, though in this and some of the following displays this dependence has been suppressed for the sake of clarity.

Next equating the first-order term to zero yields

$$(a_{ijkl}p_ip_l - \delta_{jk})A_k^{(1)} + p_ia_{ijkl}\frac{\partial A_k^{(0)}}{\partial x_l} + \rho^{-1}\frac{\partial}{\partial x_i}(\rho a_{ijkl}p_lA_k^{(0)}) \quad = \quad 0. \tag{2.7}$$

By the symmetry of the stiffness tensor a_{ijkl} and equation (2.5), equation (2.7) is reduced to a divergence form (Burridge et. al. [BdHMS98]),

$$\frac{\partial(a_{ijkl}A_i^{(0)}A_k^{(0)}p_l)}{\partial x_j} \quad = \quad 0. \tag{2.8}$$

By equation (2.5), $\mathbf{A}^{(0)}$ is a multiple of the normalized eigenvector $\mathbf{g}$ of matrix (Γ_{jk}), so $\mathbf{A}^{(0)} = A^{(0)}\mathbf{g}$ in equation (2.8) leads to

$$\frac{\partial\left(a_{ijkl}g_ig_k(A^{(0)})^2p_l\right)}{\partial x_j} \quad = \quad \frac{\partial\left(v_j(A^{(0)})^2\right)}{\partial x_j} = 0, \tag{2.9}$$

where the group (ray) velocity vector $\mathbf{v} = (v_j)$ is used,

$$\frac{dx_j}{dt} = v_j \quad = \quad a_{ijkl}g_ig_kp_l. \tag{2.10}$$

Finally, the transport equation for the amplitude function is

$$\nabla\cdot\left((A^{(0)})^2\mathbf{v}\right) \quad = \quad 0. \tag{2.11}$$

Equation (2.6) is a sextic polynomial equation in the slowness vector $\mathbf{p}$; that is, the slowness vector $\mathbf{p}$ lies on a sextic surface, which consists of three sheets, each surrounding the origin (Figure 2.1). To understand this, introduce

$$p_i \quad = \quad \frac{n_i}{V} \tag{2.12}$$

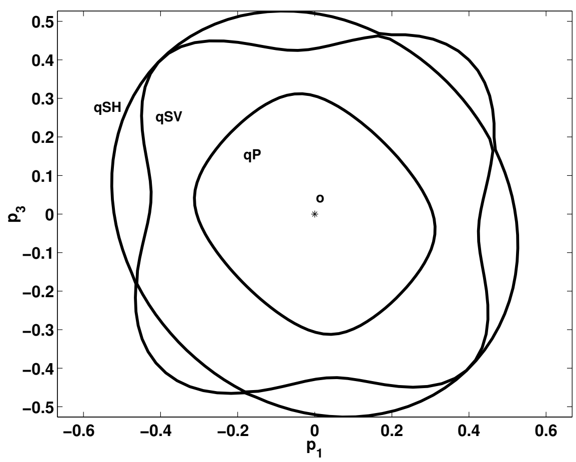

Figure 2.1 The slowness surface for typical anisotropic media: a sextic surface which consists of three slowness sheets.

where $\mathbf{n} = (n_i)$ is the unit normal vector to the wavefront and V is the normal or phase speed of the wavefront. Then equation (2.6) yields

$$det(a_{ijkl}n_i n_l - V^2\delta_{jk}) = 0, \tag{2.13}$$

which is a cubic characteristic polynomial equation with respect to V^2, hence it has three eigenvalues corresponding to a quasi-longitudinal ("quasi-P" or "qP") and two transverse waves. Moreover, experiment shows that the velocity of the quasi-P wave is always greater than those of the transverse waves (Fedorov [Fed68], p 95). Hence the largest eigenvalue of equation (2.13) corresponding to the quasi-P wave propagation is simple (uniquely defined), and the quasi-P slowness sheet is the innermost one detached from other two sheets. Furthermore, the quasi-P slowness sheet is **convex** by the following simple argument (Musgrave [Mus70], p 92): if the inner detached slowness sheet is not wholly strict convex, a straight line could intersect the inner sheet at 4 or more points and yet make at least 4 further intersections with the remaining sheets; but any straight line must intersect the slowness surface at only 6 points, real or imaginary because the slowness surface is sextic.

The convexity of quasi-P slowness sheet is essential in constructing the paraxial approximation for the quasi-P eikonal equation.

2.2 The Paraxial eikonal equation for quasi-P waves

The Christoffel matrix $\Gamma_{jk} = \sum_{i,l} a_{ijkl} p_i p_l$ is positive definite and scales as $p^2 = \mathbf{p} \cdot \mathbf{p}$. Therefore each eigenvalue takes the form $v^2(\mathbf{x}, \mathbf{p}) p^2$, where v is a homogeneous function of degree zero in $\mathbf{p}$. Because the largest eigenvalue, denoted $v_{qP}^2(\mathbf{x}, \mathbf{p})$, is simple (Fedorov [Fed68], p 95), it depends smoothly on the components of the Christoffel matrix, i.e., on $\mathbf{p}$ and the Hooke tensor. The slowness vector $\mathbf{p}$ for which

$$S(\mathbf{x}, \mathbf{p}) \equiv |\mathbf{p}| v_{qP}(\mathbf{x}, \mathbf{p}) = 1, \tag{2.14}$$

forms the **qP slowness surface**, and v_{qP} is the qP phase velocity. Note that these vectors solve the Christoffel equation (2.6).

The qP wave eikonal equation results from combining the slowness surface condition (2.14) with the slowness identity $\mathbf{p} = \nabla \tau$:

$$S(\mathbf{x}, \nabla \tau) = 1. \tag{2.15}$$

The method of characteristics relates its solution τ of the slowness surface equation (2.15) to the rays of geometrical optics, which are the solutions of the ordinary differential equations

$$\frac{d\mathbf{x}}{dt} = \nabla_{\mathbf{p}} S(\mathbf{x}, \mathbf{p}), \tag{2.16}$$

$$\frac{d\mathbf{p}}{dt} = -\nabla_{\mathbf{x}} S(\mathbf{x}, \mathbf{p}), \tag{2.17}$$

where the homogeneity of the eigenvalue v_{qP} in $\mathbf{p}$ is used, so that $\tau = t$ has dimension of time.

Downgoing rays correspond to the part of the slowness surface on which $\frac{dx_3}{dt} > 0$. A useful description of this part of the surface follows from its **convexity** (Musgrave [Mus70], p 92). Theorem A.1 shows that

- for each $\mathbf{x}$ and horizontal slowness vector (p_1, p_2), there are at most two choices of p_3 for which $\mathbf{p} = (p_1, p_2, p_3)$ solves slowness surface equation (2.15);
- when two distinct solutions exist, only one satisfies (Figure 2.2)

$$\frac{dx_3}{dt} = \frac{\partial S(\mathbf{x}, \mathbf{p})}{\partial p_3}(\mathbf{x}, \mathbf{p}) \geq 0.$$

By Definition A.1, this choice defines p_3 as a function of $\mathbf{x}, p_1, p_2$:

$$p_3 = H(\mathbf{x}, p_1, p_2), \tag{2.18}$$

which is also a partial differential equation for τ.

The characteristics (rays) of eikonal equation (2.18) are downgoing, so they can be parameterized by $x_3 = z$ and satisfy

$$\begin{aligned} \frac{dx_i}{dx_3} &= -\frac{\partial H}{\partial p_i}, \ i = 1, 2; & (2.19) \\ \frac{d\tau}{dx_3} &= H - p_1 \frac{\partial H}{\partial p_1} - p_2 \frac{\partial H}{\partial p_2}. & (2.20) \end{aligned}$$

The ray group velocity is

$$v_g = \frac{\sqrt{\left(\frac{\partial H}{\partial p_1}\right)^2 + \left(\frac{\partial H}{\partial p_2}\right)^2 + 1}}{H(p_1, p_2) - \frac{\partial H}{\partial p_1} p_1 - \frac{\partial H}{\partial p_2} p_2}, \tag{2.21}$$

where

$$\begin{aligned} \frac{\partial H}{\partial p_1} &= -\frac{a_{1jkl} p_l g_j g_k}{a_{3jkl} p_l g_j g_k}, & (2.22) \\ \frac{\partial H}{\partial p_2} &= -\frac{a_{2jkl} p_l g_j g_k}{a_{3jkl} p_l g_j g_k}, & (2.23) \end{aligned}$$

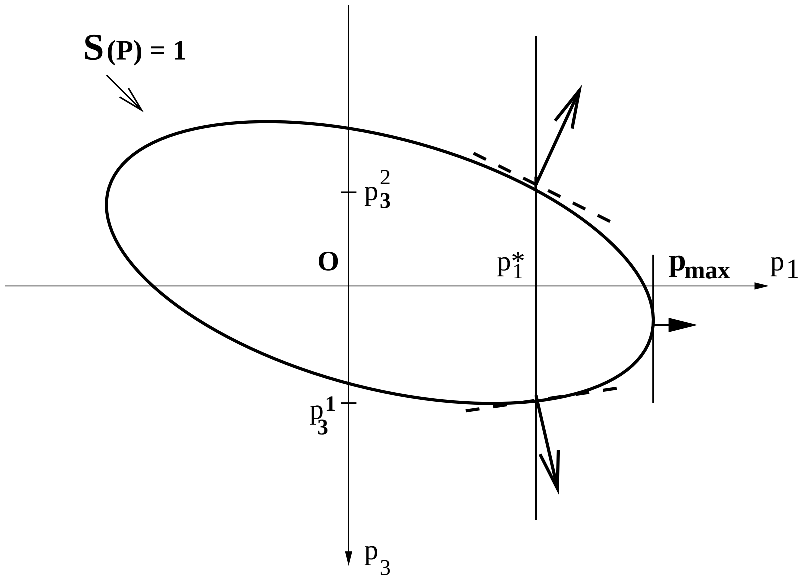

Figure 2.2 The p_3 components of outward normals at the two intersections on the convex slowness surface have opposite signs.

with g_j the eigenvector corresponding to v_{qP}; the Einstein summation convention is assumed in equations (2.22) and (2.23).

However, neither the partial differential equation (2.18) nor its rays are well-defined for all p_1, p_2. To remedy this defect, by Theorem A.3, I introduce another family of Hamiltonian functions H_Δ (Definition A.2 and A.3), each of which is identical to H along "safely downgoing" rays and defined everywhere in phase space. It is convenient to parametrize the horizontal variables (p_1, p_2) by polar coordinates: $(p_1, p_2) = (p\cos\phi, p\sin\phi)$. Corollary A.1 says that for each planar angle ϕ, the family of planes perpendicular to $(\cos\phi, \sin\phi, 0)$ is tangent to the slowness surface at exactly one point $(p_{\max}(\phi)\cos\phi, p_{\max}(\phi)\sin\phi, p_3(\phi))$. By Definition A.3, choose $0 < \Delta < 1$, for $\phi, p \le (1-\Delta)p_{\max}(\phi)$, set $H_\Delta(p\cos\phi, p\sin\phi) = H(p\cos\phi, p\sin\phi)$; this is the unique root of $S = 1$ with $p_3 > p_3(\phi)$; for $\phi, p > (1-\Delta)p_{\max}(\phi)$, set $H_\Delta(p\cos\phi, p\sin\phi) = H((1-\Delta)p_{\max}(\phi)\cos\phi, (1-\Delta)p_{\max}(\phi)\sin\phi)$. By construction, rays of H_Δ are rays of H, and hence of the anisotropic elastic model, so long as their horizontal slowness components $(p\cos\phi, p\sin\phi)$ satisfy $p \leq (1-\Delta)p_{\max}(\phi)$.

By convexity of quasi-P slowness surface and Corollary A.2, the ray angle ψ with the vertical axis stays safely away from 90 degrees:

$$\begin{aligned} \tan\psi &= \frac{\sqrt{\left(\frac{\partial x_1}{\partial \tau}\right)^2 + \left(\frac{\partial x_2}{\partial \tau}\right)^2}}{\frac{\partial x_3}{\partial \tau}} \\ &= \sqrt{\left(\frac{\partial H_\Delta}{\partial p_1}\right)^2 + \left(\frac{\partial H_\Delta}{\partial p_2}\right)^2} \leq O(\frac{1}{\Delta}). \end{aligned} \tag{2.24}$$

Numerical algorithms for the **paraxial eikonal equation**

$$\frac{\partial \tau}{\partial x_3} = H_\Delta\left(\mathbf{x}, \frac{\partial \tau}{\partial x_1}, \frac{\partial \tau}{\partial x_2}\right), \tag{2.25}$$

require explicit bounds on $\tan\psi$. Because of the convexity of the slowness surface, I need only look for these at the boundary of the region where $H_\Delta = H$, i.e., where $p = (1-\Delta)p_{\max}(\phi)$. Since H_Δ is radially constant outside this region, the required bound is simply the maximum length of the 2-vector $\left(\frac{\partial H_\Delta}{\partial p_1}, \frac{\partial H_\Delta}{\partial p_2}\right)$ over the set $\{p = (1-\Delta)p_{\max}(\phi)\}$. The solution of the paraxial eikonal equation is the same as the solution of the original eikonal equation so long as the horizontal slowness components $(p\cos\phi, p\sin\phi)$ satisfy $p \leq (1-\Delta)p_{\max}(\phi)$.

In Chapter 3 I will develop numerical algorithms for the construction of the paraxial Hamiltonian in general anisotropic solids.

2.3 Quasi-P wave amplitudes in Cartesian coordinates

If rays start from the point source, the amplitude $A \equiv A^{(0)}$ satisfies that (Burridge et. al. [BdHMS98], de Hoop and Bleistein [dHB97])

$$A(\tau) = \frac{1}{4\pi(\rho(\mathbf{s})\rho(\mathbf{x}))^{\frac{1}{2}} M^{\frac{1}{2}}} \tag{2.26}$$

with

$$M = |v(\mathbf{s})|V(\mathbf{x})\frac{dW(\mathbf{x},\mathbf{s})|_{\mathbf{x}}}{dS(\mathbf{s})|_{\mathbf{s}}}. \tag{2.27}$$

Here $V(\mathbf{x})$ is the qP phase velocity at $\mathbf{x}$; dS($\mathbf{s}$) and dW($\mathbf{x},\mathbf{s}$) are surface area elements of the slowness surface Ω at $\mathbf{s}$ and the wavefront W at $\mathbf{x}$, respectively. The mapping from $\Omega(\mathbf{s})$ to W($\mathbf{x},\mathbf{s}$) is defined by integrating the ray-tracing equations from $(\mathbf{s},\mathbf{p}(0))$ at $\tau = 0$ to $(\bar{\mathbf{x}},\mathbf{p}(\tau))$ at $\tau = \tau(\mathbf{x},\mathbf{s})$, where $\mathbf{p}(\tau)$ is the slowness vector. For the source $\mathbf{s}$ fixed, $\bar{\mathbf{x}}$ varies on $W(\mathbf{x},\mathbf{s})$ as $\mathbf{p}(0)$ varies on $\Omega(\mathbf{s})$, and $\bar{\mathbf{x}}(\tau(\mathbf{x},\mathbf{s})) = \mathbf{x}$ for some $\mathbf{p}(0)$ on $\Omega(\mathbf{s})$.

To expedite the numerical implementation, I introduce the so-called ray coordinates τ, q_1, q_2, where q_1 and q_2 are the ray parameters of the ray. In the case of a point source, q_1 and q_2 can be taken as take-off angles of the ray at the source. q_1 and q_2 characterize the given ray, and τ characterizes the position of the point on the ray. τ, q_1 and q_2 can be considered the curvilinear coordinates on the wavefront; that is,

$$x_i = x_i(\tau, q_1, q_2). \tag{2.28}$$

Also, q_1 and q_2 parametrize the slowness surface $\Omega(\mathbf{s})$,

$$p_i = p_i(q_1, q_2),\ \ i = 1, 2, 3, \tag{2.29}$$

for $\mathbf{p} = (p_1, p_2, p_3)$ on $\Omega(\mathbf{s})$.

By ray coordinates, the surface area elements on the wavefront and slowness surface are, respectively,

$$dW(\mathbf{x},\mathbf{s}) = \left|\frac{\partial \mathbf{x}}{\partial q_1} \times \frac{\partial \mathbf{x}}{\partial q_2}\right| dq_1 dq_2 \tag{2.30}$$

and

$$dS = \left|\frac{\partial \mathbf{p}}{\partial q_1} \times \frac{\partial \mathbf{p}}{\partial q_2}\right| dq_1 dq_2. \tag{2.31}$$

So finally I have

$$M = |v(\mathbf{s})| V(\mathbf{x}) \frac{\left|\frac{\partial \mathbf{x}}{\partial q_1} \times \frac{\partial \mathbf{x}}{\partial q_2}\right|_{\mathbf{x}}}{\left|\frac{\partial \mathbf{p}}{\partial q_1} \times \frac{\partial \mathbf{p}}{\partial q_2}\right|_{\mathbf{s}}}. \tag{2.32}$$

Because I want to compute the amplitude by finite-difference methods in Cartesian coordinates rather than in ray coordinates, I have to reformulate the amplitude formula in Cartesian coordinates.

To do so, note that the Jacobian from ray coordinates (τ, q_1, q_2) to Cartesian coordinates satisfies that

$$\frac{\partial(\mathbf{x})}{\partial(\tau, q_1, q_2)} = \left|\frac{\partial \mathbf{x}}{\partial \tau} \cdot \left(\frac{\partial \mathbf{x}}{\partial q_1} \times \frac{\partial \mathbf{x}}{\partial q_2}\right)\right| \tag{2.33}$$

$$= V(\mathbf{x}) \left|\frac{\partial \mathbf{x}}{\partial q_1} \times \frac{\partial \mathbf{x}}{\partial q_2}\right|; \tag{2.34}$$

then it follows that

$$\left|\frac{\partial \mathbf{x}}{\partial q_1} \times \frac{\partial \mathbf{x}}{\partial q_2}\right| = \frac{1}{V(\mathbf{x})} \left(\frac{\partial(\tau, q_1, q_2)}{\partial(\mathbf{x})}\right)^{-1} \tag{2.35}$$

$$= \frac{1}{V(\mathbf{x})} \frac{1}{|\nabla \tau \cdot (\nabla q_1 \times \nabla q_2)|} \tag{2.36}$$

where ∇ is the gradient operator with respect to $\mathbf{x}$. Therefore,

$$A(\mathbf{x}; \mathbf{s}) = R(q_1(\mathbf{x}; \mathbf{s}), q_2(\mathbf{x}; \mathbf{s})) \left(|\nabla \tau \cdot (\nabla q_1 \times \nabla q_2)|\right)^{\frac{1}{2}}, \tag{2.37}$$

where the anisotropic radiation pattern is

$$R(q_1(\mathbf{x}; \mathbf{s}), q_2(\mathbf{x}; \mathbf{s})) = \frac{1}{4\pi \left(\rho(\mathbf{s}) \rho(\mathbf{x}) |v(\mathbf{s})|\right)^{\frac{1}{2}}} \left(\left|\frac{\partial \mathbf{p}}{\partial q_1} \times \frac{\partial \mathbf{p}}{\partial q_2}\right|_{\mathbf{s}}\right)^{\frac{1}{2}}. \tag{2.38}$$

In the above formula, the traveltime τ comes from the finite-difference solution of the paraxial eikonal equation introduced in the last section. Now I will derive two new advection equations to compute ∇q_1 and ∇q_2. Because along a ray the two ray parameters are constant, the derivatives of q_1 and q_2 with respect to τ vanish,

$$\frac{dq_1}{d\tau} = \frac{\partial q_1}{\partial x_1}\frac{\partial x_1}{\partial \tau} + \frac{\partial q_1}{\partial x_2}\frac{\partial x_2}{\partial \tau} + \frac{\partial q_1}{\partial x_3}\frac{\partial x_3}{\partial \tau} = 0, \tag{2.39}$$

$$\frac{dq_2}{d\tau} = \frac{\partial q_2}{\partial x_1}\frac{\partial x_1}{\partial \tau} + \frac{\partial q_2}{\partial x_2}\frac{\partial x_2}{\partial \tau} + \frac{\partial q_2}{\partial x_3}\frac{\partial x_3}{\partial \tau} = 0. \tag{2.40}$$

Once the traveltime τ is known, $v_i = \dfrac{\partial x_i}{\partial \tau}(i = 1, 2, 3)$ can be computed from the ray equations,

$$v_i = \frac{\partial x_i}{\partial \tau} = a_{ijkl} g_k g_j \frac{\partial \tau}{\partial x_l}. \tag{2.41}$$

Therefore, equations (2.39) and (2.40) are advection equations in Cartesian coordinates for the two ray parameters q_1 and q_2,

$$v_1 \frac{\partial q_1}{\partial x_1} + v_2 \frac{\partial q_1}{\partial x_2} + v_3 \frac{\partial q_1}{\partial x_3} = 0, \tag{2.42}$$

$$v_1 \frac{\partial q_2}{\partial x_1} + v_2 \frac{\partial q_2}{\partial x_2} + v_3 \frac{\partial q_2}{\partial x_3} = 0. \tag{2.43}$$

Because the paraxial eikonal equation characterizes the traveltime along downgoing rays, v_3 always has a positive lower bound; therefore, I can have evolution equations in depth direction $x_3 = z$ for the two ray parameters,

$$\frac{\partial q_1}{\partial x_3} = -\frac{v_1}{v_3}\frac{\partial q_1}{\partial x_1} - \frac{v_2}{v_3}\frac{\partial q_1}{\partial x_2}, \tag{2.44}$$

$$\frac{\partial q_2}{\partial x_3} = -\frac{v_1}{v_3}\frac{\partial q_2}{\partial x_1} - \frac{v_2}{v_3}\frac{\partial q_2}{\partial x_2}. \tag{2.45}$$

To finish the amplitude computation I still need to compute $\dfrac{\partial \mathbf{p}}{\partial q_1}$ and $\dfrac{\partial \mathbf{p}}{\partial q_2}$. Because the quasi-P slowness surface is convex, the mapping from the slowness vector to the group velocity vector is one to one; therefore, $\mathbf{p}$ is uniquely determined from known q_1 and q_2. Because the mapping from the slowness vector to the ray direction is explicit, I can solve a nonlinear system to obtain $\mathbf{p}^0$ from known q_1^0 and q_2^0 at a point $\mathbf{x}$,

$$q_1\left(p_1, p_2, H_\Delta(\mathbf{x}, p_1, p_2)\right) = q_1^0, \tag{2.46}$$

$$q_2\left(p_1, p_2, H_\Delta(\mathbf{x}, p_1, p_2)\right) = q_2^0; \tag{2.47}$$

for example, Newton method can solve this system effectively (Dennis and Schnabel [DS83]). Later I will design an algorithm to solve this nonlinear system.

2.4 Final words

The *geometrical optics term* was first derived from the reduced wave equation in the frequency domain by Sommerfeld and Runge in 1916, and it was intended to provide an asymptotic approximation to the exact solution of the wave equation (Keller and Lewis [KL95]). In this chapter, the term is derived in the temporal domain by applying the progressing wave expansion (Courant and Hilbert [CH62]) to the wave equation; the latter approach is equivalent to the former after the Fourier transform. However, a question remains to be answered: assuming that the solution of the wave equation exists and is unique, is the constructed "asymptotic expansion" indeed the asymptotic expansion of the exact solution? The modern theory of linear partial differential equations has proved that the answer is true for large classes of problems, and the proofs have required new concepts and techniques such as Fourier Intergral Operators, wave front sets (Keller and Lewis [KL95], Taylor [Tay96]).

The solution of the eikonal equation (2.6) can be understood as a geodesic on a region with a general Riemannian metric (Taylor [Tay96]). These equations appear in a variety of applications, including problems in shape offsetting, shape-from-shading, optimal path planning around obstacles and computer vision; see Sethian [Set99a] for an excellent review.

In anticipation of the subsequent algorithm development for computing paraxial Hamiltonians, a few more comments are in order.

First of all, the group (ray) velocity direction coincides with the energy flux direction (Musgrave [Mus70]), which is essential in extrapolating the traveltime field by finite-difference schemes. In isotropic solids, the group velocity direction is the same as the wave front normal which appears in the eikonal equation explicitly, so the energy flux direction can be easily determined in order to extrapolate the traveltime field. However, in anisotropic solids the situation is completely different as shown in this chapter. Consequently, I have to incorporate the information of the group velocity direction into the paraxial Hamiltonian by some strategy. Naturally, at the outset I imposed an explicit aperture limitation on the group velocity vector, and this limitation in turn implied an implicit restriction on the slowness vector. However, the mapping from the group velocity vector to the slowness vector is implicit and the only readily available information is the slowness vector, so the explicit limitation on the group velocity vector cannot give rise to an efficient algorithm for the paraxial Hamiltonian. Thanks to the strict convexity of the slowness surface, the explicit limitation on the slowness surface as done here also implies an implicit one on the group velocity vector. Therefore, this way leads to an efficient algorithm, and the resultant Hamiltonian has a built-in reliable indicator of the group velocity direction.

Chapter 3

Geometrical Optics for Quasi-P Waves: Methods

In Chapter 2 I presented the theoretical formulation of paraxial eikonal equations for traveltimes and related advection equations for amplitudes. However, due to the complexity of wave propagations in anisotropic solids, in general it is difficult to find an explicit form of the paraxial Hamiltonian. Therefore I have devised some numerical algorithms for computing the paraxial Hamiltonian. Since the theoretical results proved in Appendix A are constructive, the design of the algorithms basically follows those constructions. As a by-product, an algorithm is also designed for initializing the traveltime in finite-difference schemes. Once the paraxial Hamiltonian is in place, I can use upwind finite-difference schemes to solve the paraxial eikonal equation. To motivate the design of the finite-difference schemes, I present a new derivation of a first-order Godunov's scheme. In addition, high-order schemes can be constructed by using this first-order scheme as a building block.

3.1 Algorithms for computing paraxial Hamiltonian H_Δ

The slowness surface equation (2.6) is a sextic polynomial equation in $p_i (i = 1, 2, 3)$, which characterizes three wave modes; that is, the slowness surface is sextic and consists of three sheets. The innermost sheet is convex and corresponds to the quasi-P wave mode. By introducing the planar polar coordinates, I have transformed this sextic polynomial equation into a sextic polynomial equation in p and p_3 for each planar angle ϕ; hence I now have a two-dimensional problem to deal with. In the following development of algorithms, I will concentrate on the numerical construction of the paraxial quasi-P Hamiltonian for the two-dimensional general anisotropic media.

Suppose that the two-dimensional slowness surface is given by

$$F(p_1, p_3) \quad = \quad 0, \tag{3.1}$$

where F is a sextic or quartic polynomial in p_1 and p_3, respectively. The sextic case corresponds to three wave modes coupled, namely, quasi-P and two transverse waves (see Figure 2.1). The quartic case corresponds to two wave modes coupled, namely, quasi-P and one transverse wave modes (see Figure 3.1). Specifically, in this section I assume that F is a sextic polynomial in p_1 and p_3; the quartic case can be treated similarly.

For arbitrary p_1^* there are four possiblities for the roots p_3 of sextic polynomial equation $F(p_1^*, p_3) = 0$: (1) no real roots at all; (2) two real roots; (3) four real roots; (4) six real roots; see Figure 2.1. I am especially interested in case (4) since this case means that among the six roots there are two roots corresponding to the quasi-P wave. Because the quasi-P slowness surface is convex, separated from and nested inside other two ovoid surfaces, the straight line $p_1 = p_1^*$ has two intersection points with the quasi-P slowness surface if $p_1 = p_1^*$ belongs to the quasi-P slowness surface. Since the origin $(p_1, p_3) = (0, 0)$ is in the domain enclosed by the quasi-P slowness surface, p_1^* can be chosen small enough to guarantee that the straight line $p_1 = p_1^*$ has six real intersection points with the slowness surface $F(p_1, p_3) = 0$, among which two intersection points are on the quasi-P slowness surface. The six real roots can be sorted into ascending order; moreover, the third and fourth roots correspond to the two intersection points with the quasi-P slowness surface, denoted as p_3^{up} and p_3^{dn}. I use Algorithm 3.1 to find $(p_1^*, p_3^{\mathrm{up}})$ and $(p_1^*, p_3^{\mathrm{dn}})$:

Algorithm 3.1

- Input: α $(0 < \alpha < 1)$, $\sigma = 0.0000001$ and a quasi-P slowness vector with first component p_1^o nonzero.

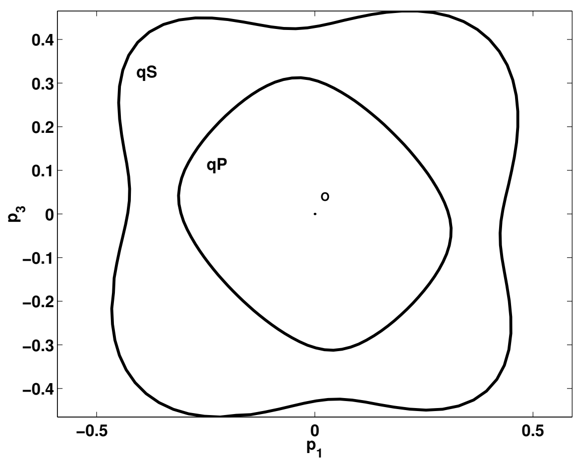

Figure 3.1 The decoupled slowness surface for typical anisotropic media: a quartic surface which consists of two slowness sheets.

- Set $p_1^* = p_1^o$.
- Set the norm of imaginary parts of roots: $norm\_imag\_p_3 = 10.0$.
- While $norm\_imag\_p_3 > \sigma$ do
  - $p_1^* \leftarrow \alpha p_1^*$;
  - $root\_p_3 \leftarrow$ all roots of $F(p_1^*, p_3) = 0.0$.
  - $norm\_imag\_p_3 \leftarrow$ Norm of imaginary parts of $root\_p_3$.
- Sort the roots in ascending order: $root\_p_3 \leftarrow \mathrm{sort}(root\_p_3)$.
- Output: p_1^*,
  - if F is sextic: $p_3^{\mathrm{up}} \leftarrow root\_p_3(4)$, $p_3^{\mathrm{dn}} \leftarrow root\_p_3(3)$.
  - if F is quartic: $p_3^{\mathrm{up}} \leftarrow root\_p_3(3)$, $p_3^{\mathrm{dn}} \leftarrow root\_p_3(2)$.

Because the quasi-P slowness surface is strictly convex and closed, there are two extreme points at which $F = 0$ and $\dfrac{\partial F}{\partial p_3} = 0$. To locate such points, as shown in

Appendix A, I need two pairs of intersection points $(p_1^*, p_3^{\rm dn})$ and $(p_1^*, p_3^{\rm up})$, which can be produced by Algorithm 3.1 with p_1^o chosen as positive and negative, respectively.

Assuming that $(p_1^*, p_3^{\rm dn})$ and $(p_1^*, p_3^{\rm up})$ are known on the quasi-P slowness surface, I can find on the quasi-P slowness surface a point $(p_1^{\rm m}, p_3^{\rm m})$ at which $\dfrac{\partial F}{\partial p_3}(p_1^{\rm m}, p_3^{\rm m}) = 0$, and Algorithm 3.2 achieves this goal.

Algorithm 3.2

- Input: p_1^*, $p_3^{\rm dn}$, $p_3^{\rm up}$ and $\sigma = 0.00001$.
- Set $p_3^{\rm a} \leftarrow p_3^{\rm up}$, $p_3^{\rm b} \leftarrow p_3^{\rm dn}$ and $\dfrac{\partial F}{\partial p_3} \leftarrow 10\sigma$.
- Compute: $p_3^{\rm c} \leftarrow \frac{1}{2}(p_3^{\rm a} + p_3^{\rm b})$.
- While $\left|\dfrac{\partial F}{\partial p_3}\right| > \sigma$ do
  - $root\_p_1 \leftarrow$ all roots of $F(p_1, p_3^{\rm c}) = 0.0$.
  - Sort the roots in ascending order: $root\_p_1 \leftarrow {\rm sort}(root\_p_1)$.
  - If F is sextic:
    - If $p_1^* > 0$, then $p_1^{\rm c} \leftarrow root\_p_1(4)$; else $p_1^{\rm c} \leftarrow root\_p_1(3)$; end.
  - If F is quartic:
    - If $p_1^* > 0$, then $p_1^{\rm c} \leftarrow root\_p_1(3)$; else $p_1^{\rm c} \leftarrow root\_p_1(2)$; end.
  - Compute $\dfrac{\partial F}{\partial p_3}$ at $(p_1^{\rm c}, p_3^{\rm c})$
  - If $\dfrac{\partial F}{\partial p_3} > \sigma$; then $p_3^{\rm b} \leftarrow p_3^{\rm c}$, $p_3^{\rm c} \leftarrow 0.5(p_3^{\rm a} + p_3^{\rm b})$; end.
  - If $\dfrac{\partial F}{\partial p_3} < -\sigma$; then $p_3^{\rm a} \leftarrow p_3^{\rm c}$, $p_3^{\rm c} \leftarrow 0.5(p_3^{\rm a} + p_3^{\rm b})$; end.
- Output: $p_1^{\rm m} \leftarrow p_1^{\rm c}$ and $p_3^{\rm m} \leftarrow p_3^{\rm c}$.

Algorithm 3.2 is a bisection method for the root of a monotonic function (the first-order derivative of a convex function), so it has only linear convergence; nevertheless, in practice it converges very fast. To obtain quadratic convergence for the root of the first-order derivative induced equation, I have to use the information of the second-order derivative. Therefore, I embed Newton's method into the algorithm, and the algorithm reads:

Algorithm 3.3

- Input: p_1^*, p_3^{dn}, p_3^{up} and $\sigma = 0.00001$.
- Set $p_3^{\mathrm{a}} \leftarrow p_3^{\mathrm{up}}$, $p_3^{\mathrm{b}} \leftarrow p_3^{\mathrm{dn}}$ and $\dfrac{\partial F}{\partial p_3} \leftarrow 10\sigma$.
- Compute: $p_3^{\mathrm{c}} \leftarrow \frac{1}{2}(p_3^{\mathrm{a}} + p_3^{\mathrm{b}})$.
- While $\left|\dfrac{\partial F}{\partial p_3}\right| > \sigma$ do
  - $root\_p_1 \leftarrow$ all roots of $F(p_1, p_3^{\mathrm{c}}) = 0.0$.
  - Sort the roots in ascending order: $root\_p_1 \leftarrow \mathrm{sort}(root\_p_1)$.
  - If F is sextic:
    - If $p_1^* > 0$, then $p_1^{\mathrm{c}} \leftarrow root\_p_1(4)$; else $p_1^{\mathrm{c}} \leftarrow root\_p_1(3)$; end.
  - If F is quartic:
    - If $p_1^* > 0$, then $p_1^{\mathrm{c}} \leftarrow root\_p_1(3)$; else $p_1^{\mathrm{c}} \leftarrow root\_p_1(2)$; end.
  - Compute $\dfrac{\partial F}{\partial p_3}$ and $\dfrac{\partial^2 F}{\partial p_3^2}$ at $(p_1^{\mathrm{c}}, p_3^{\mathrm{c}})$
  - $p_3^{\mathrm{c}} \leftarrow p_3^{\mathrm{c}} - \left(\dfrac{\partial^2 F}{\partial p_3^2}\right)^{-1} \dfrac{\partial F}{\partial p_3}$.
- Output: $p_1^{\mathrm{m}} \leftarrow p_1^{\mathrm{c}}$ and $p_3^{\mathrm{m}} \leftarrow p_3^{\mathrm{c}}$.

Once the two extreme points are located by Algorithm 3.2 or Algorithm 3.3, Algorithm 3.4 yields paraxial Hamiltonian H_Δ.

Algorithm 3.4

- Input: Δ ($0 < \Delta < 1$), p_1^+, p_1^- and p_1.

- Set $p_1^{\text{lt}} \leftarrow (1-\Delta)p_1^-$; $p_1^{\text{rt}} \leftarrow (1-\Delta)p_1^+$.
- If $p_1^{\text{lt}} \leq p_1 \leq p_1^{\text{rt}}$, then $\widehat{p_1} = p_1$.
- If $p_1 < p_1^{\text{lt}}$, then $\widehat{p_1} = p_1^{\text{lt}}$.
- If $p_1 > p_1^{\text{rt}}$, then $\widehat{p_1} = p_1^{\text{rt}}$.
- $root\_p_3 \leftarrow$ all roots of $F(\widehat{p_1}, p_3) = 0.0$.
- Sort the roots in ascending order: $root\_p_3 \leftarrow \text{sort}(root\_p_3)$.
- Pick out the one for downgoing qP wave:
  - if F is sextic: $\widehat{p_3} \leftarrow root\_p_3(4)$.
  - if F is quartic: $\widehat{p_3} \leftarrow root\_p_3(3)$.
- Output: $H_\Delta(\widehat{p_1}) \leftarrow \widehat{p_3}$.

Supposing that I have two extreme points (p_1^+, p_3^+) and (p_1^-, p_3^-), where $F = 0$ and $\dfrac{\partial F}{\partial p_3} = 0$, the ray tracing equation says that the outward normals at these two extreme points correspond to the rays which point to the horizontal directions (positive or negative, respectively):

$$\begin{aligned}
\frac{dx_1}{dt} &= \left(p_1\frac{\partial F}{\partial p_1} + p_3\frac{\partial F}{\partial p_3}\right)^{-1}\frac{\partial F}{\partial p_1}, \\
\frac{dx_3}{dt} &= \left(p_1\frac{\partial F}{\partial p_1} + p_3\frac{\partial F}{\partial p_3}\right)^{-1}\frac{\partial F}{\partial p_3}, \\
\frac{dp_1}{dt} &= -\left(p_1\frac{\partial F}{\partial p_1} + p_3\frac{\partial F}{\partial p_3}\right)^{-1}\frac{\partial F}{\partial x_1}, \\
\frac{dp_3}{dt} &= -\left(p_1\frac{\partial F}{\partial p_1} + p_3\frac{\partial F}{\partial p_3}\right)^{-1}\frac{\partial F}{\partial x_3}.
\end{aligned} \tag{3.2}$$

Once realizing this, I can design a shooting method to compute the traveltime from the source point to a specific point in homogeneous anisotropic media. Since the group angle is known, the goal is to find the corresponding slowness vector to give the correct group angle. The resultant algorithm follows.

Algorithm 3.5

- Input: $(x_1^{\mathrm{s}}, z_1^{\mathrm{s}})$, $(x_1^{\mathrm{o}}, z_1^{\mathrm{o}})$, (p_1^+, p_3^+) and (p_1^-, p_3^-).
- Set $p_1^{\mathrm{a}} \leftarrow p_1^-$ and $p_1^{\mathrm{b}} \leftarrow p_1^+$.
- Compute: $p_1^{\mathrm{c}} \leftarrow \frac{1}{2}(p_1^{\mathrm{a}} + p_1^{\mathrm{b}})$.
- Compute: $\mathrm{gcos} \leftarrow \dfrac{x_1^o - x_1^s}{\sqrt{(x_1^o - x_1^s)^2 + (x_3^o - x_3^s)^2}}$.
- While $p_1^{\mathrm{a}} < p_1^{\mathrm{c}}$ and $p_1^{\mathrm{c}} < p_1^{\mathrm{b}}$, do
  - $root\_p_3 \leftarrow$ all roots of $F(p_1^{\mathrm{c}}, p_3) = 0.0$.
  - Sort the roots in ascending order: $root\_p_3 \leftarrow \mathrm{sort}(root\_p_3)$.
  - Pick out the one for downgoing qP wave:
    * if F is sextic: $p_3^{\mathrm{c}} \leftarrow root\_p_3(4)$.
    * if F is quartic: $p_3^{\mathrm{c}} \leftarrow root\_p_3(3)$.
  - Compute the group velocity vector at $(p_1^{\mathrm{c}}, p_3^{\mathrm{c}})$:

$$\begin{aligned} v_g^1 &= \left(p_1 \frac{\partial F}{\partial p_1} + p_3 \frac{\partial F}{\partial p_3}\right)^{-1} \frac{\partial F}{\partial p_1} \\ v_g^3 &= \left(p_1 \frac{\partial F}{\partial p_1} + p_3 \frac{\partial F}{\partial p_3}\right)^{-1} \frac{\partial F}{\partial p_3} \end{aligned}$$

  - Compute: $\mathrm{gvel} \leftarrow \dfrac{v_g^1}{\sqrt{(v_g^1)^2 + (v_g^3)^2}}$.
  - If $\mathrm{gvel} \geq \mathrm{gcos}$, then $p_1^{\mathrm{b}} \leftarrow p_1^{\mathrm{c}}$ and $p_1^{\mathrm{c}} \leftarrow 0.5(p_1^{\mathrm{a}} + p_1^{\mathrm{b}})$; else $p_1^{\mathrm{a}} \leftarrow p_1^{\mathrm{c}}$ and $p_1^{\mathrm{c}} \leftarrow 0.5(p_1^{\mathrm{a}} + p_1^{\mathrm{b}})$.
- Compute traveltime: $t = \dfrac{\sqrt{(x_1^o - x_1^s)^2 + (x_3^o - x_3^s)^2}}{\sqrt{(v_g^1)^2 + (v_g^3)^2}}$.

Once again, Algorithm 3.5 is a bisection method which has only linear convergence; however, unlike Algorithm 3.2, it is not entirely straightforward to embed Newton's method into this algorithm, since the mapping from the group angle to the phase angle is not explicit.

Note: Because the take-off angle is the same as the group angle in the homogeneous media, with a few changes Algorithm 3.5 can be modified to solve the nonlinear system (2.46) and (2.47) to obtain the quantity needed in the amplitude computation.

3.2 A new derivation of a first-order Godunov scheme

Equation (2.25) is a nonlinear first-order PDE for traveltime τ. However, traveltime is not unique: when the elastic parameters vary with position, in general many rays pass over at least some points in the subsurface. More than one traveltime may be assigned to each such point. One choice of unique traveltime for each subsurface point is the **least time** ("first arrival time"). It turns out that this first arrival time field is a **solution** of the eikonal equation (in a generalized sense). These assertions were established some time ago (Lions [Lio82]) for isotropic problems, and I surmise that they apply as well to anisotropic problems with a convex slowness surface.

To compute the first-arrival traveltime field by grid-based finite difference schemes, I derive a first-order scheme from ray tracing rather than directly from the eikonal equation. Nonetheless, the end result will be recognizable as a difference approximation to the eikonal equation. Because the use of ray tracing in the derivation inherently honors causality, the resulting difference scheme is upwind, a term more or less synonymous with causality in this setting. I consider the two-dimensional case to illustrate the idea, which means all out-of-plane components vanish in the equations formulated for 3-D media and all rays stay in the x_1x_3 plane. The three-dimensional case is similar.

The first-order finite difference approximation to the qP eikonal equation rests on several approximations; that is, I may approximate locally near a grid point:

1. the group velocity v_g by a constant;

2. the rays by straight line segments;

3. the traveltime by piecewise linear functions of x_1 with nodes at the grid ponit.

Given a Cartesian grid $(m\Delta x_1, n\Delta x_3)$ in two-dimensional space, Figure 3.2, let

$$\tau_m^n \approx \tau(m\Delta x_1, n\Delta x_3), \tag{3.3}$$

be the grid function approximating the traveltime. Near $(m\Delta x_1, n\Delta x_3)$, I define the approximation of derivative τ_{x_1} at $(x_1, n\Delta x_3)$ by

$$\tau_{x_1}^n \approx \begin{cases} D_{x_1}^- \tau_m^n \equiv \dfrac{\tau_m^n - \tau_{m-1}^n}{\Delta x_1} & \text{for } (m-1)\Delta x_1 < x_1 < m\Delta x_1 \ , \\ D_{x_1}^+ \tau_m^n \equiv \dfrac{\tau_{m+1}^n - \tau_m^n}{\Delta x_1} & \text{for } m\Delta x_1 < x_1 < (m+1)\Delta x_1; \end{cases} \tag{3.4}$$

the group velocity is given by

$$v_g^\pm = \frac{\sqrt{\left(\frac{\partial H}{\partial p_1}(D_{x_1}^\pm \tau_m^n)\right)^2 + 1}}{H(D_{x_1}^\pm \tau_m^n) - \frac{\partial H}{\partial p_1}(D_{x_1}^\pm \tau_m^n) D_{x_1}^\pm \tau_m^n}. \tag{3.5}$$

A ray segment meeting the line $x_3 = n\Delta x_3$ at x_1 and passing through $(m\Delta x_1, (n+1)\Delta x_3)$ has length

$$L = \Delta x_3 \sqrt{1 + \left(\frac{x_1 - m\Delta x_1}{\Delta x_3}\right)^2}, \tag{3.6}$$

so that the time predicted at $(m\Delta x_1, (n+1)\Delta x_3)$ under the foregoing assumption is

$$\tau_m^{n+1} \approx \begin{cases} \tau_m^n + (x_1 - m\Delta x_1) D_{x_1}^+ \tau_m^n + \dfrac{L}{v_g^+} & \text{for } m\Delta x_1 \le x_1 \le (m+1)\Delta x_1 \ , \\ \tau_m^n + (x_1 - m\Delta x_1) D_{x_1}^- \tau_m^n + \dfrac{L}{v_g^-} & \text{for } (m-1)\Delta x_1 \le x_1 \le m\Delta x_1. \end{cases} \tag{3.7}$$

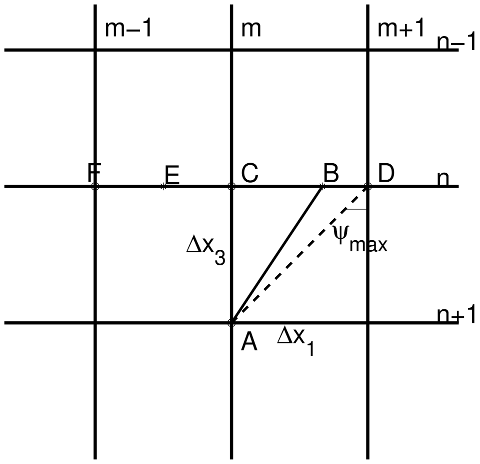

Figure 3.2 Cartesian grid : a possible ray hitting point A

Finally, the ray velocity vector should obey the ray equation (2.19),

$$-\frac{x_1 - m\Delta x_1}{\Delta x_3} = \frac{dx_1}{dx_3} \approx \begin{cases} -\frac{\partial H}{\partial p_1}(D^+_{x_1}\tau^n_m) & \text{for } m\Delta x_1 \le x_1 \le (m+1)\Delta x_1, \\ -\frac{\partial H}{\partial p_1}(D^-_{x_1}\tau^n_m) & \text{for } (m-1)\Delta x_1 \le x_1 \le m\Delta x_1, \end{cases} \tag{3.8}$$

i.e.,

$$x_1 - m\Delta x_1 \approx \begin{cases} \Delta x_3 \frac{\partial H}{\partial p_1}(D^+_{x_1}\tau^n_m) & \text{for } m\Delta x_1 \le x_1 \le (m+1)\Delta x_1 , \\ \Delta x_3 \frac{\partial H}{\partial p_1}(D^-_{x_1}\tau^n_m) & \text{for } (m-1)\Delta x_1 \le x_1 \le m\Delta x_1. \end{cases} \tag{3.9}$$

Substituting expression (3.9) into (3.7) and carrying out the algebra, I arrive at

$$\tau^{n+1}_m = \begin{cases} \tau^n_m + \Delta x_3 H\left(D^+_{x_1}\tau^n_m\right) & \text{for } m\Delta x_1 \le x_1 \le (m+1)\Delta x_1 , \\ \tau^n_m + \Delta x_3 H\left(D^-_{x_1}\tau^n_m\right) & \text{for } (m-1)\Delta x_1 \le x_1 \le m\Delta x_1, \end{cases} \tag{3.10}$$

where x_1 is chosen to satisfy (3.8) if possible.

Next I have to examine the significance of the condition switching the branches of (3.10). If $m\Delta x_1 \le x_1 \le (m+1)\Delta x_1$, i.e., the ray slope is nonpositive, it follows from (3.8) that

$$\frac{\partial H}{\partial p_1}(D^+_{x_1}\tau^n_m) \ \ge \ 0. \tag{3.11}$$

Similarly, the second branch occurs when

$$\frac{\partial H}{\partial p_1}(D_{x_1}^- \tau_m^n) \quad \leq \quad 0. \tag{3.12}$$

When neither of these occur, i.e.,

$$\frac{\partial H}{\partial p_1}(D_{x_1}^+ \tau_m^n) \quad \leq \quad 0 \leq \frac{\partial H}{\partial p_1}(D_{x_1}^- \tau_m^n), \tag{3.13}$$

rays fan away from $(m\Delta x_1, n\Delta x_3)$; that is, this point is a center of rarefaction. Then to good approximation, the ray entering $(m\Delta x_1, (n+1)\Delta x_3)$ is vertical; i.e. along it

$$\frac{\partial H}{\partial p_1} \quad = \quad 0. \tag{3.14}$$

Finally, if both conditions are satisfied, i.e.,

$$\frac{\partial H}{\partial p_1}(D_{x_1}^+ \tau_m^n) \quad \geq \quad 0 \geq \frac{\partial H}{\partial p_1}(D_{x_1}^- \tau_m^n), \tag{3.15}$$

then two rays converge on $(m\Delta x_1, (n+1)\Delta x_3)$, and I should select the least of the two times provided by (3.10).

Because the Hamiltonian H is concave (Appendix A), all four of these options can be combined in the simple formula

$$\tau_m^{n+1} \quad = \quad \tau_m^n + \Delta x_3 H\left(\mathrm{maxmod}(\max(D_{x_1}^- \tau_m^n, 0), \min(D_{x_1}^+ \tau_m^n, 0))\right), \tag{3.16}$$

where the function maxmod returns the larger value in modulus.

The scheme just proposed is identical to the so-called Godunov first-order scheme; see Osher and Sethian [OS88] and Osher and Shu [OS91]. The problem I have solved to obtain this scheme is the so-called Riemann problem for the eikonal equation, in which the initial traveltime data are piecewise linear.

There remains one further detail to take care of: the approximate ray might meet $x_3 = n\Delta x_3$ **outside** the interval $(m-1)\Delta x_1 \leq x_1 \leq (m+1)\Delta x_1$. The difference scheme (3.16) would necessarily become unstable, as the numerical domain of dependence of $(m\Delta x_1, (n+1)\Delta x_3)$ (namely, the three points on $x_3 = n\Delta x_3$ in the scheme (3.16)) would no longer contain in its convex hull the continuum domain of dependence $\{x\}$. In order that this Courant-Friedrichs-Lewy ("CFL") criterion be satisfied with certainty, I limit the slope of ray:

$$\max\left\{\left|\frac{\partial H}{\partial p_1}\left(D^{+}_{x_1}\tau^n_m\right)\right|, \left|\frac{\partial H}{\partial p_1}\left(D^{-}_{x_1}\tau^n_m\right)\right|\right\} \leq \frac{\Delta x_1}{\Delta x_3}. \tag{3.17}$$

By Definition A.3 of H_Δ, for given $\Delta > 0$, there exists $p_{\max}$ such that

$$H_\Delta(p_1) = \begin{cases} H(p_1), & \text{if } p_1 \leq (1-\Delta)p_{\max}; \\ H((1-\Delta)p_{\max}), & \text{else.} \end{cases} \tag{3.18}$$

Furthermore, by Corollary A.2 I need to choose just $\Delta > 0$ such that

$$\frac{\Delta x_1}{\Delta x_3} \geq O(\frac{1}{\Delta}). \tag{3.19}$$

Then I can find $p_{\max}$ needed in the defintion of H_Δ (see Definition A.3). Finally, the resulting difference scheme is

$$\tau^{n+1}_m = \tau^n_m + \Delta x_3 H_\Delta\left(\text{maxmod}(\max(D^{-}_{x_1}\tau^n_m, 0), \min(D^{+}_{x_1}\tau^n_m, 0))\right), \tag{3.20}$$

which is consistent with the **paraxial eikonal equation**

$$p_3 = H_\Delta(p_1). \tag{3.21}$$

Solutions of (3.21) are identical to solutions of the eikonal equation at points whose associated rays make angle $\leq \psi^{\max}_g = \arctan(\frac{\Delta x_1}{\Delta x_3})$ with the vertical ($x_1 = constant$) throughout their length. (For the point source problem, the associated ray is the first-arriving ray connecting the subsurface point with the source point). Thus with this paraxial limitation, the scheme is suitable for computing the traveltime of **downgoing ray fans**.

3.3 ENO and WENO schemes

To compute the first-arrival traveltime field by a grid-based finite difference scheme, in the last section I derived a first-order upwind scheme from ray tracing rather than directly from the eikonal equation. However, because the amplitude involved in the geometrical optics term is related to the second-order derivatives of traveltimes, a first-order accurate amplitude field requires a third-order accurate traveltime field. It is necessary to construct high-order accurate finite-difference schemes. In this section I will use the first-order scheme as a building block to design high-order schemes.

To increase the order of convergence of finite-difference schemes, I employ higher-order Essentially NonOscillatory (ENO) and Weighted ENO (WENO) refinements. ENO schemes were introduced by Osher and Sethian [OS88] and Osher and Shu [OS91] for solving Hamilton-Jacobi equations. WENO schemes were first proposed by Liu et. al. [LOC94] to overcome the drawbacks of ENO's. Jiang and Peng [JP97] made further improvements and extensions for Hamilton-Jacobi equations. Because WENO schemes are extensions of ENO schemes, I will present second- and third-order ENO schemes first.

Given mesh sizes Δx_1, Δx_2 and Δx_3, denote $\tau^n_{m,k}$ as the numerical approximation to the viscosity solution $\tau(x_1^m, x_2^k, x_3^n)$ of equation (2.25) at the grid point (x_1^m, x_2^k, x_3^n). Define the backward ($-$) and forward ($+$) first-order difference quotient approximations to the left and right derivatives of $\tau(x_1, x_2, x_3)$ at the location (x_1^m, x_2^k, x_3^n) with respect to x_1 and x_2 as

$$D^{\pm}_{x_1}\tau^n_{m,k} = \pm\frac{\tau^n_{m\pm 1,k} - \tau^n_{m,k}}{\Delta x_1}, \qquad D^{\pm}_{x_2}\tau^n_{m,k} = \pm\frac{\tau^n_{m,k\pm 1} - \tau^n_{m,k}}{\Delta x_2}. \tag{3.22}$$

The second-order and third-order ENO refinements of $D^{\pm}_{x_1}\tau^n_{m,k}$ (Osher and Sethian [OS88]) are

$$D^{\pm,2}_{x_1}\tau^n_{m,k} = D^{\pm}_{x_1}\tau^n_{m,k} \mp \frac{1}{2}\Delta x_1 \; m(D^{\pm}_{x_1}D^{\pm}_{x_1}\tau^n_{m,k}, D^{-}_{x_1}D^{+}_{x_1}\tau^n_{m,k}), \tag{3.23}$$

$$D_{x_1}^{\pm,3}\tau_{m,k}^n = -\frac{1}{6}(\Delta x_1)^2\ m(D_{x_1}^{\pm}D_{x_1}^{\pm}D_{x_1}^{\pm}\tau_{m,k}^n, D_{x_1}^{+}D_{x_1}^{+}D_{x_1}^{-}\tau_{m,k}^n, D_{x_1}^{+}D_{x_1}^{-}D_{x_1}^{-}\tau_{m,k}^n) + D_{x_1}^{\pm,2}\tau_{m,k}^n, \tag{3.24}$$

where

$$m(x,y) = \min(\max(x,0), \max(y,0)) + \max(\min(x,0), \min(y,0)).$$

ENO refinements for $D_{x_2}^{\pm}\tau_{m,k}^n$ are defined similarly.

The upwind jth order ENO approximations for $\frac{\partial\tau}{\partial x_1}$ and $\frac{\partial\tau}{\partial x_2}$ are

$$\widehat{D}_{x_1}^j\tau = \mathrm{modmax}(\max(D_{x_1}^{-,j}\tau,0), \min(D_{x_1}^{+,j}\tau,0)), \tag{3.25}$$

$$\widehat{D}_{x_2}^j\tau = \mathrm{modmax}(\max(D_{x_2}^{-,j}\tau,0), \min(D_{x_2}^{+,j}\tau,0)), \tag{3.26}$$

where the modmax function returns the larger value in modulus.

The second-order and third-order ENO Runge-Kutta steps are

$$\begin{aligned} \delta_2^1\tau &= \Delta x_3^{\mathrm{cfl}} H_\Delta\left(\widehat{D}_{x_1}^2\tau, \widehat{D}_{x_2}^2\tau\right), \\ \delta_2^2\tau &= \frac{1}{2}\left(\delta_2^1\tau + \Delta x_3^{\mathrm{cfl}} H_\Delta\left(\widehat{D}_{x_1}^2(\tau+\delta_2^1\tau), \widehat{D}_{x_2}^2(\tau+\delta_2^1\tau)\right)\right), \end{aligned} \tag{3.27}$$

and

$$\begin{aligned} \delta_3^1\tau &= \Delta x_3^{\mathrm{cfl}} H_\Delta\left(\widehat{D}_{x_1}^3\tau, \widehat{D}_{x_2}^3\tau\right), \\ \delta_3^2\tau &= \frac{1}{4}\left(\delta_3^1\tau + \Delta x_3^{\mathrm{cfl}} H_\Delta\left(\widehat{D}_{x_1}^3(\tau+\delta_3^1\tau), \widehat{D}_{x_2}^3(\tau+\delta_3^1\tau)\right)\right), \\ \delta_3^3\tau &= \frac{1}{3}\left(2\delta_3^2\tau + 2\Delta x_3^{\mathrm{cfl}} H_\Delta\left(\widehat{D}_{x_1}^3(\tau+\delta_3^2\tau), \widehat{D}_{x_2}^3(\tau+\delta_3^2\tau)\right)\right). \end{aligned} \tag{3.28}$$

The depth step $\Delta x_3^{\mathrm{cfl}}$ must satisfy the stability condition

$$\Delta x_3{}^{\mathrm{cfl}}\left(\max_{p_1,p_2}\sqrt{\left(\frac{\partial H_\Delta}{\partial p_1}\right)^2 + \left(\frac{\partial H_\Delta}{\partial p_2}\right)^2}\right) \le \frac{\Delta x_1 \Delta x_2}{\sqrt{\Delta x_1{}^2 + \Delta x_2{}^2}}, \tag{3.29}$$

with the maximum taken over the relevant range of p_1 and p_2. Since H_Δ is concave (Appendix A), inequality (3.29) reduces to

$$\Delta x_3{}^{\mathrm{cfl}}\left(\max_{\{(p_1^{\mathrm{e}},p_2^{\mathrm{e}}) : 0\le\phi\le 2\pi\}}\sqrt{\left(\frac{\partial H_\Delta}{\partial p_1}\right)^2 + \left(\frac{\partial H_\Delta}{\partial p_2}\right)^2}\right) \le \frac{\Delta x_1 \Delta x_2}{\sqrt{\Delta x_1{}^2 + \Delta x_2{}^2}}, \tag{3.30}$$

where $(p_1^{\mathrm{e}}, p_2^{\mathrm{e}}) = ((1-\Delta)p_{\max}(\phi)\cos\phi, (1-\Delta)p_{\max}(\phi)\sin\phi)$.

The jth-order scheme is then

$$\tau^{n+1} \;=\; \tau^n + \delta_j^j \tau^n \tag{3.31}$$

for $n = 0, 1, 2, \cdots$.

In the upwind framework, second-order ENO schemes are total variation diminishing (TVD); hence they have at least subsequences which converge to weak solutions (Shu [Shu97], LeVeque [LeV90]). There is no known convergence result for ENO schemes of order higher than two, even for smooth solutions (Shu [Shu97]). However, Jiang and Shu [JS96] proved that WENO schemes converge for smooth solutions. In practice, I have observed that the gradient of the take-off angle based on the third-order ENO traveltime is too noisy to lead to an accurate amplitude field; see Chapter 5. To alleviate this phenomenon, instead of ENO third-order refinements, I use WENO third-order refinement (Jiang and Peng [JP97]) in the third-order Runge-Kutta step for traveltimes and WENO second-order refinement (Jiang and Peng [JP97]) in the Runge-Kutta step for take-off angles, which yield an accurate amplitude field (see Chapter 5). To be complete, I present the second- and third-order WENO schemes in the following.

The WENO second-order schemes for $D_{x_1}^{\pm}\tau_{m,k}$ are (Jiang and Peng [JP97])

$$\begin{aligned}
D_{x_1}^{-\mathrm{W},2}\tau_{m,k} &= \frac{1}{2}(D_{x_1}^{+}\tau_{m-1,k} + D_{x_1}^{+}\tau_{m,k}) - \frac{w_-}{2}(D_{x_1}^{+}\tau_{m-2,k} - 2D_{x_1}^{+}\tau_{m-1,k} + D_{x_1}^{+}\tau_{m,k}),\\
D_{x_1}^{+\mathrm{W},2}\tau_{m,k} &= \frac{1}{2}(D_{x_1}^{+}\tau_{m-1,k} + D_{x_1}^{+}\tau_{m,k}) - \frac{w_+}{2}(D_{x_1}^{+}\tau_{m+1,k} - 2D_{x_1}^{+}\tau_{m,k} + D_{x_1}^{+}\tau_{m-1,k}),
\end{aligned}$$

where

$$w_- = \frac{1}{1+2r_-^2}, \qquad r_- = \frac{\delta + (D_{x_1}^{-}D_{x_1}^{-}\tau_{m,k})^2}{\delta + (D_{x_1}^{-}D_{x_1}^{+}\tau_{m,k})^2}, \tag{3.32}$$

$$w_+ = \frac{1}{1+2r_+^2}, \qquad r_+ = \frac{\delta + (D_{x_1}^{+}D_{x_1}^{+}\tau_{m,k})^2}{\delta + (D_{x_1}^{-}D_{x_1}^{+}\tau_{m,k})^2}. \tag{3.33}$$

The WENO third-order schemes for $D^{\pm}_{x_1}\tau_{m,k}$ are (Jiang and Peng [JP97])

$$
\begin{aligned}
D^{\pm \mathrm{W},3}_{x_1}\tau_{m,k} &= \frac{1}{12}\left(-D^{+}_{x_1}\tau_{m-2,k} + 7D^{+}_{x_1}\tau_{m-1,k} + 7D^{+}_{x_1}\tau_{m,k} - D^{+}_{x_1}\tau_{m+1,k}\right) \\
&\pm \Delta x_1 \Phi^{\mathrm{WENO}}\left(D^{-}_{x_1}D^{+}_{x_1}\tau_{m\pm 2,k}, D^{-}_{x_1}D^{+}_{x_1}\tau_{m\pm 1,k}, D^{-}_{x_1}D^{+}_{x_1}\tau_{m,k}, D^{-}_{x_1}D^{+}_{x_1}\tau_{m\mp 1,k}\right),
\end{aligned}
$$

where

$$
\Phi^{\mathrm{WENO}}(a,b,c,d) = \frac{1}{3}w_0(a-2b+c) + \frac{1}{6}(w_2 - \frac{1}{2})(b-2c+d)
$$

with weights defined as

$$
\begin{aligned}
w_0 &= \frac{\alpha_0}{\alpha_0+\alpha_1+\alpha_2}, w_2 = \frac{\alpha_2}{\alpha_0+\alpha_1+\alpha_2}, \\
\alpha_0 &= \frac{1}{(\delta+\beta_0)^2}, \alpha_1 = \frac{1}{(\delta+\beta_1)^2}, \alpha_2 = \frac{1}{(\delta+\beta_2)^2}, \\
\beta_0 &= 13(a-b)^2 + 3(a-3b)^2, \\
\beta_1 &= 13(b-c)^2 + 3(b+c)^2, \\
\beta_2 &= 13(c-d)^2 + 3(3c-d)^2.
\end{aligned}
\tag{3.34}
$$

In the denominators of equations (3.32), (3.33) and (3.34), the small positive number δ is added to avoid dividing by zero. The WENO second- and third- order schemes for $D^{\pm}_{x_2}\tau_{m,k}$ are defined similarly.

3.4 Closing remarks

The algorithms developed in Section 3.1 depend upon an efficient polynomial root finder; in the current implementation the root finder in MATLAB™ has been used to find all the roots. In practice, the problem of finding all the roots of a polynomial equation may be turned into an eigenvalue problem, and plenty of algorithms are available to solve the eigenvalue problem (Golub and Van Loan [GVL96]). On the other hand, since all the roots need to be found at every grid point, a highly efficient root finder is required in practice. Because the traveltime field is mostly smooth, the slowness vector (the gradient of traveltimes) behaves similarly; it follows that the slowness vector at grid point (x_1, x_3) should provide good estimates for those at neighbors $(x_1 \pm \Delta x_1, x_3 \pm \Delta x_3)$. Therefore, a Newton-like method could use roots at (x_1, x_3) as very good initial estimates for roots at $(x_1 \pm \Delta x_1, x_3 \pm \Delta x_3)$. This is a possible approach to constructing an efficient root finder; however, I leave it as a future topic because the current goal is to verify the feasibility of the formulation of the paraxial eikonal equations.

The derivation of a first-order Godunov scheme serves as a tutorial on how the upwind finite-difference scheme works and illustrates how the aperture limitation comes into play in the evolution step.

ENO schemes were initially developed for hyperbolic conservation laws (Harten et. al. [HEOC87]) and later were extended to solve Hamilton-Jacobi equations (Osher and Sethian [OS88], Osher and Shu [OS91]). WENO schemes were developed for hyperbolic conservation laws, using a convex combination of all candidate stencils instead of just one as in the original ENO (Liu et. al. [LOC94]); then Jiang and Shu [JS96] implemented WENO schemes efficiently for hyperbolic conservation laws. Later they were extended to solve Hamilton-Jacobi equations (Jiang and Peng [JP97]). WENO schemes behave like central-difference schemes in regions where the solution is smooth and emulate ENO schemes near the singularities of the solution. Then the problem is whether the central-difference scheme applies to solving the paraxial eikonal equation. Lin and Tadmor [LT98] developed a second-order central Godunov-type scheme for Hamilton-Jacobi equations and presented some numerical results. However, on the one hand, there is no numerical result for using central-difference schemes reported on the eikonal equation with a point source; on the other hand, the amplitude computation needs a third-order finite-difference scheme. These considerations lead to my use of ENO/WENO schemes in the subsequent numerical computations.

Chapter 4

Eikonal Solvers for Transversely Isotropic Solids

In Chapter 3 I developed some numerical algorithms for solving the paraxial eikonal equation in general anisotropic solids. In this Chapter I will apply those numerical algorithms to transversely isotropic solids so as to verify the feasiblity of the algorithms and the convergence order of finite-difference schemes.

Although a general anisotropic solid has 21 independent elastic parameters, the transversely isotropic (TI) solid has only five independent elastic parameters. But it has, nevertheless, the essential anisotropic features that I want to capture; therefore, it is convenient to use TI solids as models to illustrate how the approaches work. In the first place I will consider the simplest case for TI solids, i.e., TI solids with vertical symmetry axes. Then I will construct inclined TI models by rotating VTI models. Because the slowness surface equation for the inclined TI model is a sextic polynomial equation which has the essential features of a general sextic slowness surface and admits no explicit solutions, it is suitable to use the model to test the proposed algorithms. Extensive numerical experiments show that the proposed algorithms are accurate and efficient.

4.1 The paraxial Hamiltonian for VTI solids: simplified

The elastic modulus matrix for transversely isotropic media with vertical symmetry axes (VTI) has five independent components among twelve nonzero components (Musgrave [Mus70], Thomsen [Tho86]). A closed form solution exists in this case for the eigenvalue problem (2.6). The quasi-P and quasi-SV slowness surface for VTI can be represented as a quartic polynomial equation (where the quasi-SH slowness surface is decoupled from the whole slowness surface),

$$G(p_1, p_3) \equiv c_1 p_1^4 + c_2 p_1^2 p_3^2 + c_3 p_3^4 + c_4 p_1^2 + c_5 p_3^2 + 1 = 0, \tag{4.1}$$

where

$$c_1 \equiv a_{11} a_{44}, \tag{4.2}$$

$$c_2 \equiv a_{11} a_{33} + a_{44}^2 - (a_{13} + a_{44})^2, \tag{4.3}$$

$$c_3 \equiv a_{33} a_{44}, \tag{4.4}$$

$$c_4 \equiv -(a_{11} + a_{44}), \tag{4.5}$$

$$c_5 \equiv -(a_{33} + a_{44}). \tag{4.6}$$

In the above formulae, the Voigt recipe is assumed to simplify the elasticity tensor a_{ijkl} to obtain a_{ij} (Thomsen [Tho86]).

Consequently, the slowness surface for the quasi-P wave can be simplified as

$$\tilde{S}(p_1, p_2, p_3) \equiv p_3^2 - \frac{2c}{-b + \sqrt{b^2 - 4ac}} = 0, \tag{4.7}$$

where

$$a \equiv \alpha_0^2 \beta_0^2, \tag{4.8}$$

$$b \equiv 2\alpha_0^2 \beta_0^2 (1 + \delta + (\epsilon - \delta)\frac{\alpha_0^2}{\beta_0^2})(p_1^2 + p_2^2) - \alpha_0^2 - \beta_0^2, \tag{4.9}$$

$$c \equiv ((1 + 2\epsilon)\alpha_0^2 (p_1^2 + p_2^2) - 1)(\beta_0^2 (p_1^2 + p_2^2) - 1). \tag{4.10}$$

Thomsen's parameters ([Tho86]) involved in the above coefficients are defined by

$$\begin{aligned} \alpha_0 &\equiv \sqrt{a_{33}}, \\ \beta_0 &\equiv \sqrt{a_{44}}, \\ \epsilon &\equiv \frac{a_{11} - a_{33}}{2a_{33}}, \\ \delta &\equiv \frac{(a_{13} + a_{44})^2 - (a_{33} - a_{44})^2}{2a_{33}(a_{33} - a_{44})}, \end{aligned} \tag{4.11}$$

where α_0 and β_0 are the vertical sound speeds for qP and qS waves; ϵ and δ are two measures of anisotropy.

Although $\tilde{S}$ is different from S, they are equivalent in the sense that they characterize the same qP slowness surface. Clearly,

$$\frac{\partial \tilde{S}}{\partial p_3} = 2p_3 > 0 \tag{4.12}$$

if

$$p_3 = \sqrt{\frac{2c}{-b+\sqrt{b^2-4ac}}} > 0. \tag{4.13}$$

So the qP eikonal equation for VTI is

$$p_3 = H(p_1, p_2) = \sqrt{\frac{2c}{-b+\sqrt{b^2-4ac}}}. \tag{4.14}$$

To obtain the paraxial Hamiltonian, I need to consider only the case of radial angle $\phi = 0$ in the horizontal slowness space because of the rotational symmetry about the vertical axis. First note that for VTI media, I have

$$\sqrt{p_1^2+p_2^2} = \frac{\sin\theta}{v_{qP}(\theta)}, \tag{4.15}$$

$$p_3 = \frac{\cos\theta}{v_{qP}(\theta)}, \tag{4.16}$$

where θ is the phase angle with the vertical direction, $v_{qP}(\theta)$ is the qP phase velocity for phase angle θ. Secondly, to make $\frac{\partial S}{\partial p_3} = 2p_3 = 0$, p_3 has to be zero, hence the phase angle $\theta = \frac{\pi}{2}$. It follows that

$$p_{\max}(0) = \left(\sqrt{p_1^2+p_2^2}\right)_{\max} = \frac{1}{v_{qP}(\frac{\pi}{2})}. \tag{4.17}$$

Thus

$$H_\Delta(p_1,p_2) = \begin{cases} H(p_1,p_2),\ p=\sqrt{p_1^2+p_2^2} \le \dfrac{(1-\Delta)}{v_{qP}(\frac{\pi}{2})}; \\ H\left(\dfrac{(1-\Delta)\cos\phi}{v_{qP}(\frac{\pi}{2})}, \dfrac{(1-\Delta)\sin\phi}{v_{qP}(\frac{\pi}{2})}\right), \text{ else.} \end{cases} \tag{4.18}$$

Next I want to simplify the above Hamiltonian. For $0 < \Delta < 1$, I apply Intermediate Value Theorem to function $f(\theta) = \dfrac{\sin\theta}{v_{qP}(\theta)}$ in interval $[0, \dfrac{\pi}{2}]$; then there exists $0 < \theta_{\max} < \frac{\pi}{2}$ such that

$$\frac{\sin\theta_{\max}}{v_{qP}(\theta_{\max})} = \frac{(1-\Delta)}{v_{qP}(\frac{\pi}{2})}. \tag{4.19}$$

Substitute the above relation into paraxial Hamiltonian (4.18) and combine two branch statements into one, and I have

$$H_{\theta_{\max}}(p_1, p_2) = \sqrt{\max\left(\frac{2c}{-b+\sqrt{b^2-4ac}}, \frac{\cos^2(\theta_{\max})}{v_{qP}^2(\theta_{\max})}\right)}, \tag{4.20}$$

where I have used the subscript $\theta_{\max}$ to emphasize the dependence of the Hamiltonian on phase angle $\theta_{\max}$. I call $\theta_{\max}$ the maximum phase angle. This Hamiltonian implies that I can set up a maximum phase angle to obtain a paraxial Hamiltonian in VTI.

Finally I have a paraxial eikonal equation for the quasi-P wave in VTI,

$$p_3 = H_{\theta_{\max}}(p_1, p_2) = \sqrt{\max\left(\frac{2c}{-b+\sqrt{b^2-4ac}}, \frac{\cos^2(\theta_{\max})}{v_{qP}^2(\theta_{\max})}\right)}. \tag{4.21}$$

The two derivatives needed in the numerical algorithms satisfy that

$$\frac{\partial H}{\partial p_1} = -\frac{p_1(2\alpha_0^2(1+2\epsilon)\beta_0^2(p_1^2+p_2^2) + Bp_3^2 - \alpha_0^2(1+2\epsilon) - \beta_0^2)}{p_3(2\alpha_0^2\beta_0^2 p_3^2 + B(p_1^2+p_2^2) - \alpha_0^2 - \beta_0^2)}, \tag{4.22}$$

$$\frac{\partial H}{\partial p_2} = -\frac{p_2(2\alpha_0^2(1+2\epsilon)\beta_0^2(p_1^2+p_2^2) + Bp_3^2 - \alpha_0^2(1+2\epsilon) - \beta_0^2)}{p_3(2\alpha_0^2\beta_0^2 p_3^2 + B(p_1^2+p_2^2) - \alpha_0^2 - \beta_0^2)}, \tag{4.23}$$

with

$$B = 2\alpha_0^2(\alpha_0^2(\epsilon-\delta) + \beta_0^2(1+\delta)). \tag{4.24}$$

4.2 Inclined TI solids

To illustrate how the new approach works for a general anisotropic solid, I generate a two-dimensional transversely isotropic model with an inclined symmetry axis.

Consider the quasi-P and quasi-SV slowness surface equation (4.1) for VTI. Rotate oq_1q_2 axes by angle ψ,

$$q_1 = t_{11}p_1 + t_{13}p_3, \tag{4.25}$$

$$q_3 = t_{31}p_1 + t_{33}p_3, \tag{4.26}$$

where $t_{11} = t_{33} = \cos\psi$, $t_{13} = -t_{31} = \sin\psi$.

Substituting the above relation into equation (4.1), I have a quartic polynomial equation in variables p_1, p_3,

$$\begin{aligned} F(p_1, p_3) \equiv\ & w_1p_1^4 + w_2p_1^3p_3 + w_3p_1^2p_3^2 + w_4p_1p_3^3 + w_5p_3^4 \\ & + w_6p_1^2 + w_7p_1p_3 + w_8p_3^2 + w_9 = 0, \end{aligned} \tag{4.27}$$

where

$$w_1 \equiv at_{11}^4 + bt_{11}^2t_{31}^2 + ct_{31}^4, \tag{4.28}$$

$$w_2 \equiv 4at_{11}^3t_{13} + 2b(t_{11}^2t_{31}t_{33} + t_{11}t_{13}t_{31}^2) + 4ct_{31}^3t_{33}, \tag{4.29}$$

$$w_3 \equiv 6at_{11}^2t_{13}^2 + b(t_{11}^2t_{33}^2 + 4t_{11}t_{13}t_{31}t_{33} + t_{13}^2t_{31}^2) + 6ct_{31}^2t_{33}^2, \tag{4.30}$$

$$w_4 \equiv 4at_{11}t_{13}^3 + 2b(t_{11}t_{13}t_{33}^2 + t_{13}^2t_{31}t_{33}) + 4ct_{31}t_{33}^3, \tag{4.31}$$

$$w_5 \equiv at_{13}^4 + bt_{13}^2t_{33}^2 + ct_{33}^4, \tag{4.32}$$

$$w_6 \equiv dt_{11}^2 + et_{31}^2, \tag{4.33}$$

$$w_7 \equiv 2dt_{11}t_{13} + 2et_{31}t_{33}, \tag{4.34}$$

$$w_8 \equiv dt_{13}^2 + et_{33}^2, \tag{4.35}$$

$$w_9 \equiv 1. \tag{4.36}$$

The two partial derivatives are given by

$$\frac{\partial F}{\partial p_1} = 4w_1p_1^3 + 3w_2p_3p_1^2 + 2(w_3p_3^2 + w_6)p_1 + (w_4p_3^2 + w_7)p_3, \tag{4.37}$$

$$\frac{\partial F}{\partial p_3} = 4w_5p_3^3 + 3w_4p_1p_3^2 + 2(w_3p_1^2 + w_8)p_3 + (w_2p_1^2 + w_7)p_1. \tag{4.38}$$

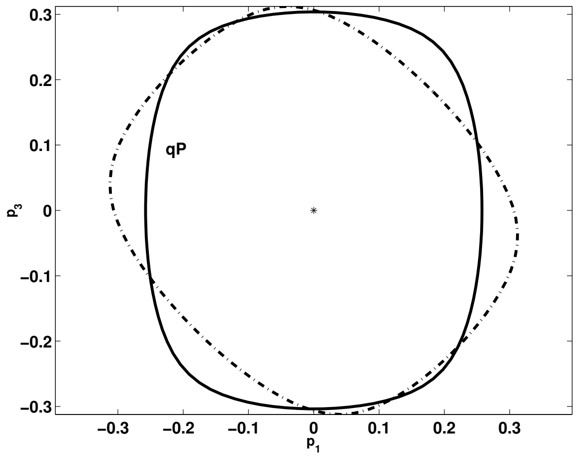

Figure 4.1 The quasi-P slowness surface: unrotated one (solid line) and the one after being rotated 45 degrees (dashed line).

Figure 4.1 shows an original TI quasi-P slowness surface with a vertical symmetry axis and its rotated version.

4.3 Numerical experiments, I: VTI solids

To give some idea of the accuracy obtainable with the difference schemes outlined in Chapter 3, I demonstrate a scheme on smooth VTI models and the (isotropic and anisotropic) Marmousi model; that is, I will solve the paraxial eikonal equation (4.21) by using a second-order ENO scheme. All examples are assumed to be of constant density.

First I have to address the traveltime initialization. Due to the singularity of the traveltime field at the source which will lead to the contamination of global numerical accuracy, to initialize the traveltime I have to use some special techniques, such as the adaptive-grid method (Qian et. al. [QBS99]) and the local uniform mesh refinement (Kim and Cook [KC98]). However, here I assume a homogeneous layer near the source and start the finite difference scheme some distance away from the source. Precisely, with a homogeneous layer near the source I use a nonlinear iteration method to compute the group velocity and directly initialize the traveltime at every grid point on a surface away from the source. This initialization technique, called the analytic method, is a modification of Algorithm 3.5 and is detailed in Appendix B.

4.3.1 2-D VTI

The first example occupies the rectangle $\{-0.5 \text{ km} \leq x_1 \leq 0.5 \text{ km}, 0 \leq x_3 \leq 1 \text{ km} \}$; the source is located at $x_1 = 0.0$ km, $x_3 = 0.0$ km. The four Thomsen's parameters of homogeneous Green River Shale are

$$\begin{aligned} \alpha_0 &= 3.330\text{km/s}, \\ \beta_0 &= 1.768\text{km/s}, \\ \epsilon &= 0.195, \\ \delta &= -0.220. \end{aligned}$$

Because the parameter δ has the same magnitude as ϵ, the near-vertical anisotropic response is dominated by δ (Thomsen [Tho86]); so this example is used to demonstrate not only the accuracy of the second-order scheme, but also the capability of the scheme in capturing the anisotropy of wave propagation. The initial data depth is at $x_3 = 0.24$ km; that is, the initial data for the finite-difference scheme is given at this depth. The maximum phase angle is taken as $\theta_{\max} = 80$ degrees.

The results are shown on Table 4.1, where Δx_1 is the x_1 direction grid sampling, Δx_3 the x_3 direction grid sampling (taken as $\Delta x_3 = 0.01$ km), Abs.Err the maximum absolute error and Rel.Err the maximum relative error (both measured at bottom $x_3 = 1$km). The formulae for the two errors are

$$\text{Abs.Err}(\tau, \Delta x_1) = \max |\tau_{ana} - \tau_{fd}^{\Delta x_1}|, \tag{4.39}$$

Table 4.1 Convergence order of a second-order ENO scheme for VTI

Δx_1	Abs.Err$(\tau, \Delta x_1)$(s)	Rel.Err$(\tau, \Delta x_1)$	α
0.08	7.3754e-04	0.00168	
0.04	2.1380e-04	6.1296e-04	1.45
0.02	5.5932e-05	1.6035e-04	1.93
0.01	1.4162e-05	4.0602e-05	1.98
0.005	3.5643e-06	1.0218e-05	1.99

$$\text{Rel.Err}(\tau, \Delta x_1) = \frac{\max|\tau_{ana} - \tau_{fd}^{\Delta x_1}|}{\max|\tau_{ana}|}, \tag{4.40}$$

where τ_{ana} denotes the traveltime from the analytic method and τ_{fd} the traveltime from the finite-difference scheme. Finally, α is the estimated convergence order:

$$\alpha = \frac{1}{\log 2} \log\left(\frac{\text{Rel.Err}(\tau, 2\Delta x_1)}{\text{Rel.Err}(\tau, \Delta x_1)}\right). \tag{4.41}$$

From this table, both the absolute error and relative error are decreased almost four times as Δx_1 is halved, and the accuracy order α is going to 2 as Δx_1 goes to zero, so this scheme is of second-order accuracy. When $\Delta x_1 = \Delta x_3 = 0.01$ km, the maximum absolute traveltime error at bottom is less than $\frac{1}{50}$ ms.

In the second example, the model occupies the rectangle $\{-0.5$ km $\leq x_1 \leq 0.5$ km, $0 \leq x_3 \leq 1$ km $\}$, and the source is located at $x_1 = 0.0$ km, $x_3 = 0.0$ km. The four elastic parameters are

$$\begin{aligned}
\alpha_0 &= \sqrt{11.0889 + x_1 + x_3}, \\
\beta_0 &= \sqrt{3.1329 + 0.5x_1 + 0.5x_3}, \\
\epsilon &= \frac{4.3247 + x_1 + x_3}{2(11.0889 + x_1 + x_3)}, \\
\delta &= \frac{(4.9477 + x_1 + x_3)^2 - (7.9560 + 0.5x_1 + 0.5x_3)^2}{2(11.0889 + x_1 + x_3)(7.9560 + 0.5x_1 + 0.5x_3)},
\end{aligned}$$

which are perturbations to Thomsen's parameters of homogeneous Green River Shale. To simulate the VTI media, these parameters necessarily satisfy the stress-strain coefficient inequalities in Berryman [Ber79]. This example is designed to test the capability of the scheme in dealing with both vertical and lateral variations.

The grid sampling is $\Delta x_1 = \Delta x_3 = 0.01$ km and the maximum phase angle is taken as $\theta_{\max} = 80$ degrees. Because of vertical and lateral variations of the example near the source, I cannot apply the initialization technique used in the first example. Instead, I use horizontal quasi-P sound speed ($= (1+\epsilon)\alpha_0$) and an adaptive integration method (Stoer and Bulirsch [SB92]) to obtain the traveltime at $x_3 = 0$ km. Figure 4.2 (left) shows the traveltime isochrons for the 2-D model. Because the lateral variation is not symmetric with respect to the source, the isochrons could not reach the same depth at $x_1 = 0.5$ km and $x_1 = -0.5$ km, the isochron of 0.262 s, for example. Also, from the figure we can see that the limitation on the maximum phase angle (artificial plane wave approximation) plays a role when the phase angle is near 90 degrees. Figure 4.2 (right) shows the calibration result for the traveltime at bottom $x_3 = 1.0$ km from the ENO scheme and the ray-tracing method (Cerveny [Cer72]). Because the ray-tracing method cannot yield traveltimes at grid points directly and every traced ray is not guaranteed to pass through the bottom, I have to use a linear interpolation method to extract the traveltime for some points (not necessarily grid points) from the ray-tracing solutions. The ray-tracing method uses the traveltime as a running parameter along the ray; namely, (x_1, x_3, p_1, p_3) are parameterized by traveltime τ. When a ray passes through the bottom $x_3 = 1$ km, I pick out the nearest two points on the ray which embrace the bottom. Then I approximate by linear interpolation the x_1 coordinate and traveltime of the intersection point between the ray and the bottom. In the computation, the ray-tracing method traces rays from phase angle -80 degrees to 80 degrees with a sampling interval of π degrees. Because the ray fan from ray-tracing is rarefying quickly away from the source, most of the intersection points are not at the grid point, so it is not appropriate to assess the accuracy of the ENO scheme and ray-tracing method this way. Nevertheless, they are perfectly consistent with each other (Figure 4.2 (right)). Also, the effect of the lateral variations of the model is evident on the traveltime curves at the bottom.

4.3.2 3-D VTI

The first 3-D VTI example is the homogeneous Green River shale, and the four Thomsen parameters are the same as in the 2D homogeneous case. The model occupies the cube $\{-0.5 \text{ km} \leq x_1 \leq 0.5 \text{ km}, -0.5 \text{ km} \leq x_2 \leq 0.5 \text{ km}, 0 \leq x_3 \leq 1.0 \text{ km} \}$, and the source is located at the center of the surface $x_3 = 0$.

The grid sampling is $\Delta x_1 = \Delta x_2 = \Delta x_3 = 0.02$ km, and the maximum phase angle is taken as $\theta_{\max} = 65$ degrees. I assume the initial homogeneous layer is at 0.1 km; that is, I start the finite difference scheme at 0.1 km. To initialize the traveltime at 0.1 km, I still use the analytic method (Appendix B). Figure 4.3 (left) shows the isochrons at the bottom $x_3 = 1$ km, and the isochrons are circles because of the transverse isotropy. Figure 4.3 (right) shows the vertical traveltime profile at $x_2 = 0.3$ km, and the anisotropic effect is evident. Figure 4.4 shows the traveltime comparison at gridline $x_2 = 0.2$ km and $x_3 = 1.0$ km between the ENO traveltime and the analytic traveltime, and the maximum absolute error is less than 0.19 ms.

The second 3-D VTI example has the same geometry as the first model. The four Thomsen's parameters are

$$
\begin{aligned}
\alpha_0 &= \sqrt{11.0889 + x_3}, \\
\beta_0 &= \sqrt{3.1329 + 0.5 x_3}, \\
\epsilon &= \frac{4.3247 + x_3}{2(11.0889 + x_3)},
\end{aligned}
$$

$$\delta = \frac{(4.9477 + x_3)^2 - (7.9560 + 0.5x_3)^2}{2(11.0889 + x_3)(7.9560 + 0.5x_3)}.$$

For this model, the discretization parameters are the same as that used in the homogeneous model. Because of the vertical variation near the source, the finite difference scheme is started at $x_3 = 0$ km with the initial traveltime assigned by using the horizontal qP sound speed, and the results are shown in Figure 4.5.

These two 3-D examples show that the scheme can be used to compute the first arrival traveltime field of 3-D smooth VTI models.

4.3.3 Isotropic and anisotropic Marmousi models

Because the Marmousi model is well known as a complex velocity model, I test the ENO scheme to see its robustness and stability on the original isotropic and the anisotropic Marmousi model created by Alkhalifah [Alk97]. I take portions of these two models to test the method; that is, the sampling domain is

$$\{4.5\text{km} \leq x_1 \leq 7.5\text{km}, 0 \leq x_3 \leq 2.9875\text{km}\},$$

and the lateral and depth samples are 241 and 240, respectively, with the sampling intervals equal to 12.5 m.

In the computation, the maximum phase angle is taken as $\theta_{\max} = 75$ degrees. The source is located at $x_1 = 6.0$ km, $x_3 = 0.0$ km. For the isotropic Marmousi model, I initialize the traveltime at $x_3 = 0$ km by using the constant surface velocity. For the anisotropic Marmousi model, the traveltime is initialized by using the horizontal sound velocity. The final results are shown in Figure 4.6 for windowed portions of the two models, corresponding to

$$\{5.4\text{km} \leq x_1 \leq 6.8\text{km}, 1.5\text{km} \leq x_3 \leq 2.9875\text{km}\}.$$

Because the vertical velocity in the anisotropic Marmousi model is the same as the isotropic Marmousi model, the portion of the wavefront corresponding to vertical wave propagation is similar (Alkhalifah [Alk97]), which can be seen by subtracting the two traveltime fields, with results shown in Figure 4.7. However, there are still some differences between the two models, especially near the upper-right corner where η (Alkhalifah [Alk97]) is larger than other places, and the maximum traveltime difference is 5.9 ms. Because a second-order finite-difference scheme is used, I believe that these traveltime differences are due to the anisotropic effect rather than to the numerical errors. The above computations show that the scheme can deal with complex geological models.

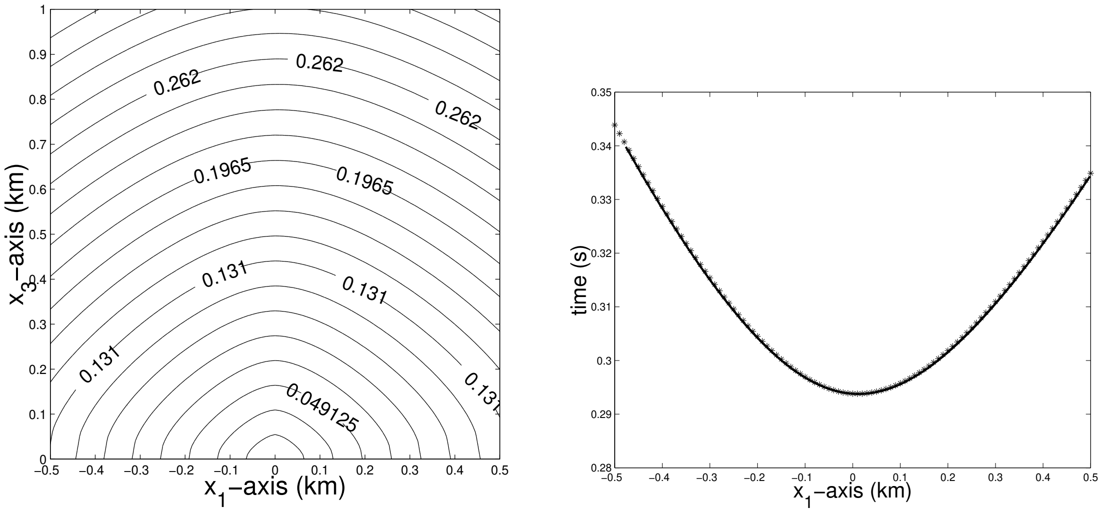

Figure 4.2 Left: traveltime isochrons for a 2-D model with vertical and lateral variations: anisotropic effects and lateral variations on the wave propagation are evident. Right: traveltime comparison at $x_3 = 1.0$ km for the model with vertical and lateral variations: ENO traveltime (*) and Ray-tracing traveltime (-); they are consistent.

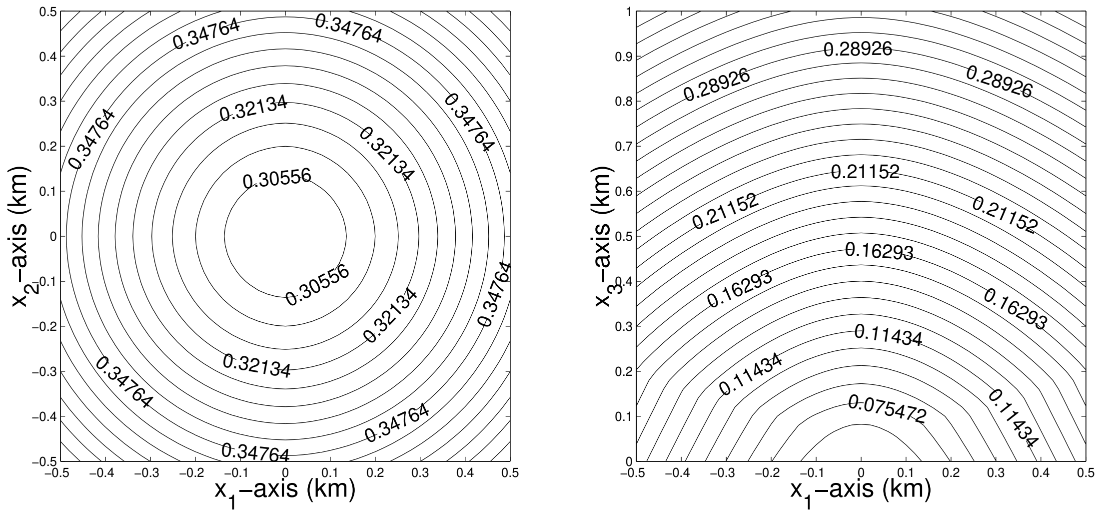

Figure 4.3 A 3-D homogeneous VTI model. The source is located at $x_1 = x_2 = x_3 = 0.0$. Left: the horizontal traveltime slice at $x_3 = 1.0$ km; isochrons are circles because of the transverse isotropy. Right: the vertical traveltime slice at $x_2 = 0.30$ km; at the lower left and right corners, the paraxial modifications have effects on the wave propagation.

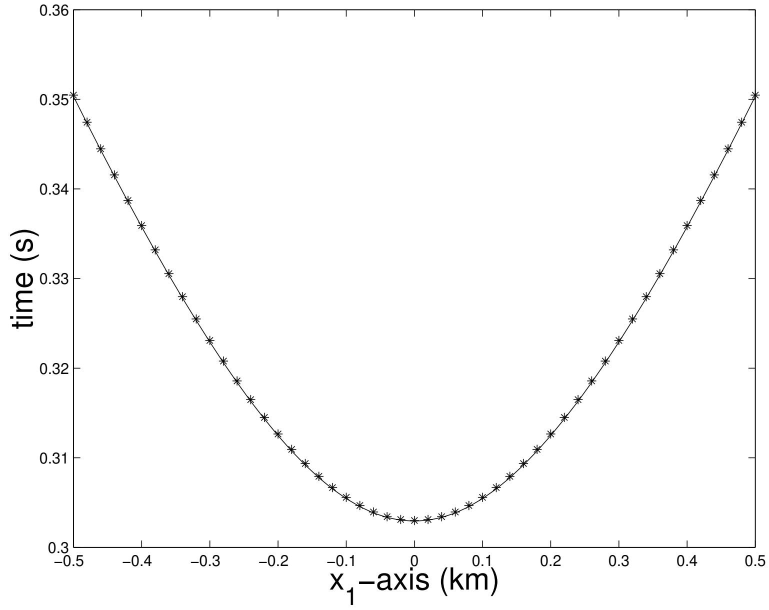

Figure 4.4 Traveltime comparison at gridline $x_2 = 0.2$ km, $x_3 = 1.0$ km for a 3-D homogeneous VTI model: ENO traveltime (*) and Analytic traveltime (-); ENO traveltime has almost the same accuracy as the analytic traveltime.

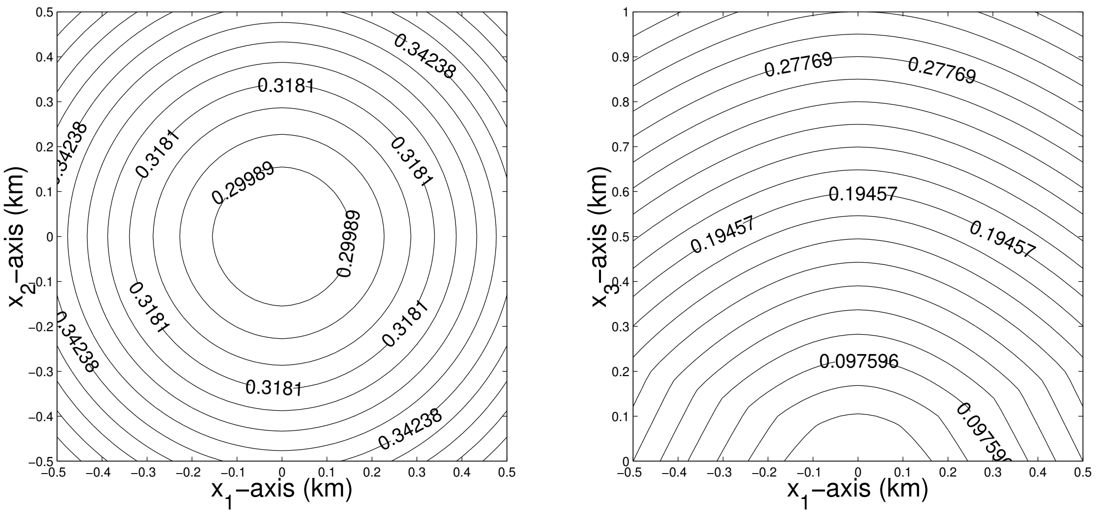

Figure 4.5 A 3-D VTI model with vertical variations. The source is located at $x_1 = x_2 = x_3 = 0.0$. Left: the horizontal traveltime slice at $x_3 = 1.0$ km; isochrons are circles because of the transverse isotropy. Right: the vertical traveltime slice at $x_2 = 0.30$ km; at the lower left and right corners, the paraxial modifications have effects on the wave propagation.

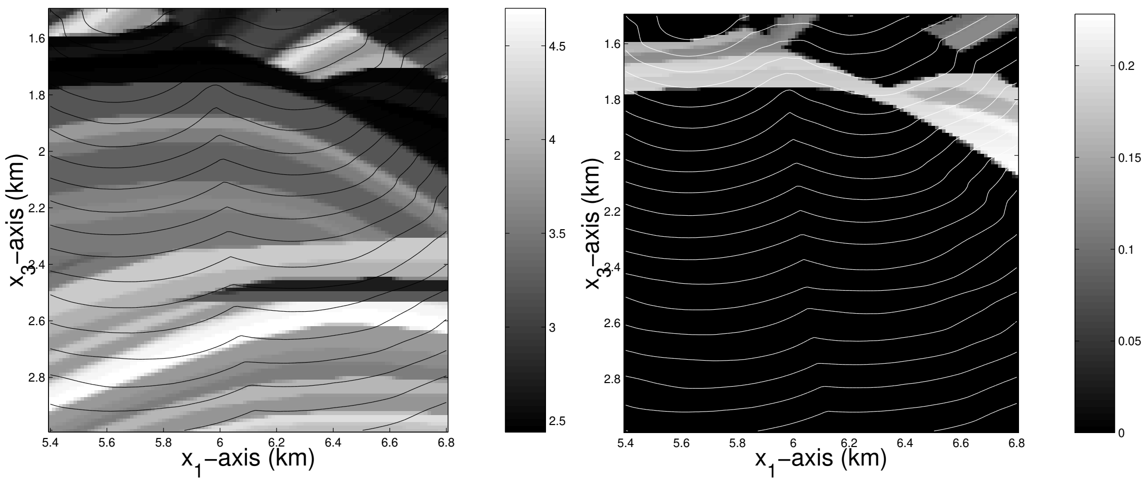

Figure 4.6 Traveltime contours overlaying the model. The source is positioned at $x_1 = 6.0$ km, $x_3 = 0.0$ km. Left: the isotropic Marmousi velocity model with a velocity unit km/s. Right: the anisotropic Marmousi η model.

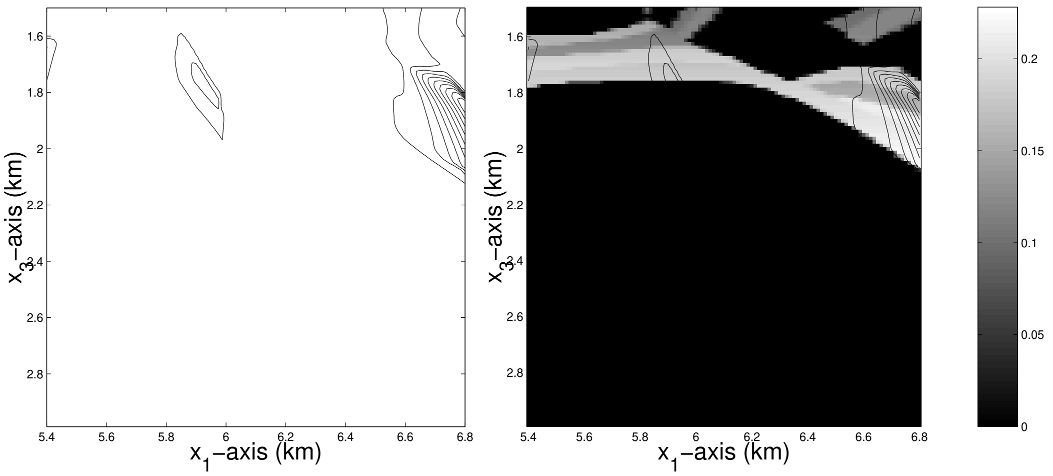

Figure 4.7 Anisotropic effects on the wave propagation. Left: nonzero contours of traveltime differences between the two Marmousi models concentrate on the region where η is larger. Right: contours of traveltime differences overlaying η model. The maximum traveltime difference is 5.9ms.

4.4 Numerical experiments, II: Inclined TI solids

I have designed algorithms to be used for general anisotropic solids. In this section I test the algorithms on the inclined TI solids. As aforementioned, inclined TI solids have the general features to be used in the tests. I will compute the paraxial Hamiltonian by Algorithm 3.4 and solve the paraxial eikonal equation (2.25) by using a second-order ENO/WENO scheme (in Section 3 of Chapter 3). All examples are assumed to be of constant density.

First I have to address the traveltime initialization. Here I assume a homogeneous layer near the source and start the finite difference scheme some distance away from the source. Namely, I use Algorithm 3.5 to compute the group velocity and initialize directly the traveltime at every grid point on a surface away from the source.

The first example occupies the rectangle

$$\{-0.5\text{km} \leq x_1 \leq 0.5\text{km}, 0 \leq x_3 \leq 1\text{km}\};$$

the source is located at $x_1 = 0.0$ km, $x_3 = 0.0$ km. The four Thomsen's parameters of a homogeneous Green River Shale are

$$\begin{aligned} \alpha_0 &= 3.330\text{km/s}, \\ \beta_0 &= 1.768\text{km/s}, \\ \epsilon &= 0.195, \\ \delta &= -0.220. \end{aligned}$$

To obtain a ITI model from the VTI model, the rotation angle ψ is 45 degrees.

Because the parameter δ has the same magnitude as ϵ, the anisotropic response along the new symmetrical axis is dominated by δ (Thomsen [Tho86]); so this example is used to demonstrate not only the accuracy of Algorithm 3.4 and the second-order ENO scheme, but also the capability of the algorithms in capturing the inclined

Table 4.2 Convergence order of a second-order ENO scheme for ITI

Δx_1	Abs.Err$(\tau, \Delta x_1)$(s)	Rel.Err$(\tau, \Delta x_1)$	α
0.04	3.3201e-04	9.5187e-04	
0.02	9.3945e-05	2.6934e-04	1.82
0.01	2.4175e-05	6.9309e-05	1.96
0.005	6.1854e-06	1.7734e-05	1.97
0.0025	1.5602e-06	4.4731e-06	1.99

anisotropy of wave propagation. The initial data depth is at $x_3 = 0.24$ km; that is, the initial data for the finite-difference scheme is given at this depth. The paraxial parameter Δ is taken as 0.02.

The results are shown on Table 4.2, where Δx_1 is the x_1 direction grid sampling, Δx_3 is the x_3 direction grid sampling (taken as $\Delta x_3 = 0.01$ km); Abs.Err is the maximum absolute error and Rel.Err is the maximum relative error, both measured at the bottom. α is the estimated convergence order, where I use the traveltime from Algorithm 3.5 as the exact solution to calibrate the traveltime from the finite-difference scheme. See formulae (4.39), (4.40) and (4.41) for definitions of these three quantities.

From this table, both the absolute error and the relative error are decreased almost four times as Δx_1 is halved, and the accuracy order α is going to 2 as Δx_1 goes to zero, so this scheme is of second-order accuracy. When $\Delta x_1 = \Delta x_3 = 0.01$ km, the maximum absolute traveltime error at bottom is less than $\frac{1}{40}$ ms.

The calibrations for the slowness surface and the traveltime are shown in Figure 4.8. To obtain the extreme points on the slowness surface, Algorithm 3.2 (the bisection method) needs 26 iterations, but Algorithm 3.3 (Newton method) needs only 6 iterations.

Figure 4.9 shows the traveltime coutours from both the analytical and numerical approaches, and the two coutours are almost the same except for a tiny difference along the aperture.

The second example is generated by rotating the model of Zinc (a kind of metal) by the angle $\psi = 30$ degrees. The four elastic parameters are (Musgrave [Mus70], p 280):

$$\begin{aligned} a_{11} &= 15.90, \\ a_{33} &= 6.21, \\ a_{13} &= 4.82, \\ a_{44} &= 4.00; \end{aligned}$$

which can be transformed into Thomsen's parameters,

$$\begin{aligned} \alpha_0 &= 2.492\text{km/s}, \\ \beta_0 &= 2.00\text{km/s}, \\ \epsilon &= 0.7802, \\ \delta &= 2.6562. \end{aligned}$$

According to the notion of Thomsen's weak anisotropy, these parameters show that the anisotropy is strong rather than weak. Therefore, this model will serve as an assay for the algorithms developed in Chapter 3 and will be examined systematically. To do this, I will apply both ENO and WENO second-order schemes (in Section 3 of Chapter 3) to both unrotated and rotated models.

Figure 4.10 (left) shows the slowness surface for Zinc with a vertical symmetry axis, and Figure 4.10 (right) shows the slowness surface after being rotated 30 degrees. To generate these Figures, the extreme points are first located by Algorithm 3.3 (Newton method), and then a number of samplings are made on an interval of p_1. In order to locate the extreme points, Algorithm 3.3 needs one and four iterations for the unrotated and rotated model, respectively.

Figure 4.11 (left) is the traveltime contours computed by the second-order ENO scheme for the VTI (unrotated) Zinc model. Figure 4.11 (right) is the traveltime calibration for the ENO scheme by using Algorithm 3.5, and the calibration shows that the traveltime produced by the two approaches match with each other very well. Similarly, Figure 4.12 (left) and Figure 4.12 (right) show similar results for the second-order WENO scheme. From Figure 4.11 (left) and Figure 4.12 (left), it can be seen that the horizontal velocity is faster than the vertical velocity because $a_{11} > a_{33}$.

Figure 4.13 (left) is the traveltime contours computed by the second-order ENO scheme for the inclined TI (rotated 30 degrees) Zinc model, and the traveltime contours are oscillating on the upper part of the figure. Figure 4.13 (right) is the traveltime calibration for the ENO scheme by using Algorithm 3.5, and the calibration shows that the traveltime produced by the ENO scheme fails to match with the analytical one by Algorithm 3.5. The failure of ENO scheme is because the ENO scheme is very sensitive to the zeros of the solution and its derivatives (Shu [Shu97]). As can be seen on the Figure 4.11 (left), the horizontal component $p_1 = \dfrac{\partial \tau}{\partial x}$ of the slowness vector is almost zero on later wavefronts. After rotation, these zeros will show up along an inclined wavefront, as shown in Figure 4.13 (left). In Figure 4.11, the senstivity did not appear because the symmetry axis of Zinc is along the vertical and is consistent with the grid line. However, it does appear in Figure 4.13 for the inclined TI model.

Figure 4.14 (left) is the traveltime contours computed by the second-order WENO scheme for the inclined TI (rotated 30 degrees) Zinc model, and the traveltime contours are smooth. Figure 4.14 (right) is the traveltime calibration for the WENO scheme by using Algorithm 3.5, and the calibration shows that the traveltime produced by the WENO scheme matchs with the analytical one obtained by Algorithm 3.5. The success of the WENO scheme is because WENO schemes improves ENO schemes by overcoming the drawbacks of ENO schemes, such as the sensitivity to the zeros of the solution and its derivatives (Shu [Shu97]).

4.5 Final comments

Although paraxial Hamiltonians do not have explicit forms for general anisotropic solids, some special cases such as VTI solids admit simplified Hamiltonians because the extreme points of the horizontal slowness surface set are known.

Rotating VTI slowness surface equations to obtain ITI slowness surface equations was inspired by Kim [Kim99]. The sextic slowness surface equation of ITI has the essential features of the slowness surface equation of general anisotropic solids so that it can be used to assay the algorithms developed in Chapter 3.

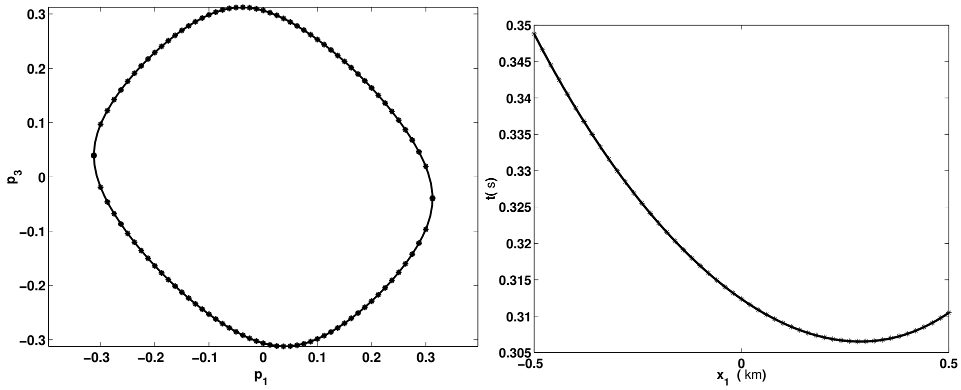

Figure 4.8 A 2-D homogeneous ITI model obtained by rotating VTI model 45 degrees. Left: slowness surface calibration; the analytical slowness surface (solid line) vs. the numerical solution (dashed line) by Algorithm 3.2. Right: the comparison of the traveltimes at the bottom by Algorithm 3.5 (solid line (–)) and the paraxial eikonal solver (star (*)).

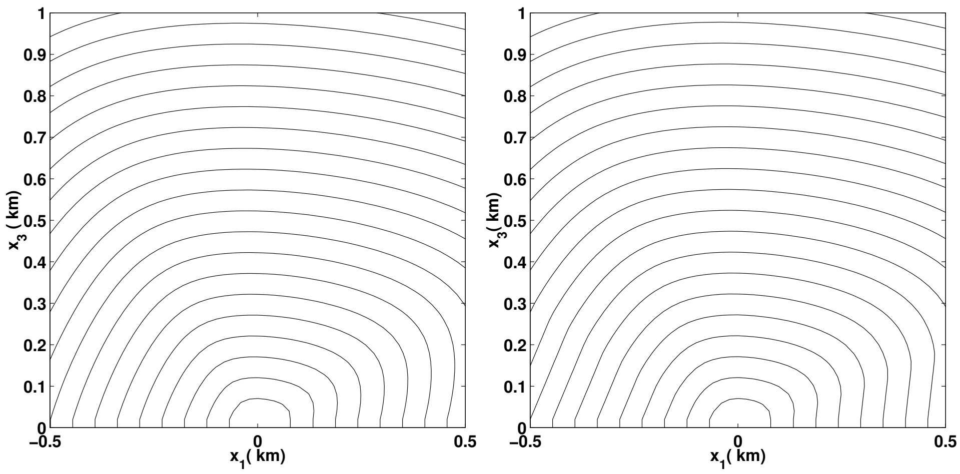

Figure 4.9 A 2-D homogeneous ITI model obtained by rotating VTI 30 degrees. The source is located at $x_1 = x_3 = 0.0$; the initial depth is 0.02km and $\Delta x_1 = \Delta x_3 = 0.02$km. Left: analytical traveltime contours by Algorithm 3.5. Right: contours of the traveltime from the paraxial eikonal solver. The paraxial eikonal solver yields the maximum absolute error 0.84ms and the relative error 0.25 percent at $x_3 = 1$km.

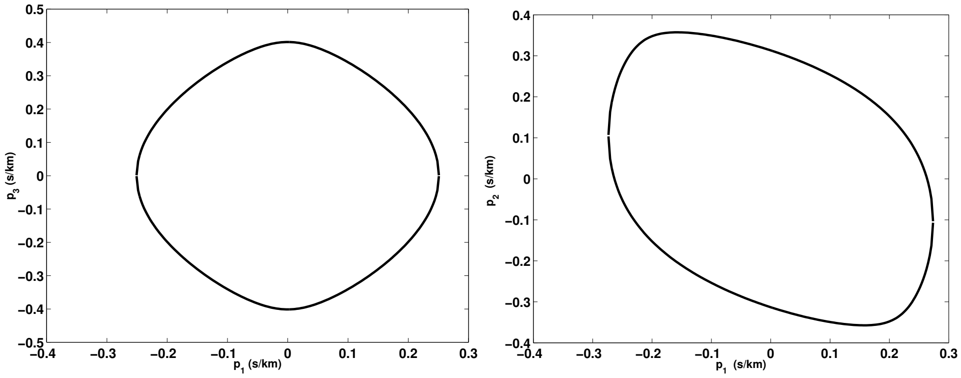

Figure 4.10 The 2-D homogeneous Zinc model. Left: the original VTI slowness surface. Right: the inclined slowness surface with rotation angle 30 degrees. The two slowness surfaces are generated by sampling an interval of p_1 which is determined by Algorithm 3.3.

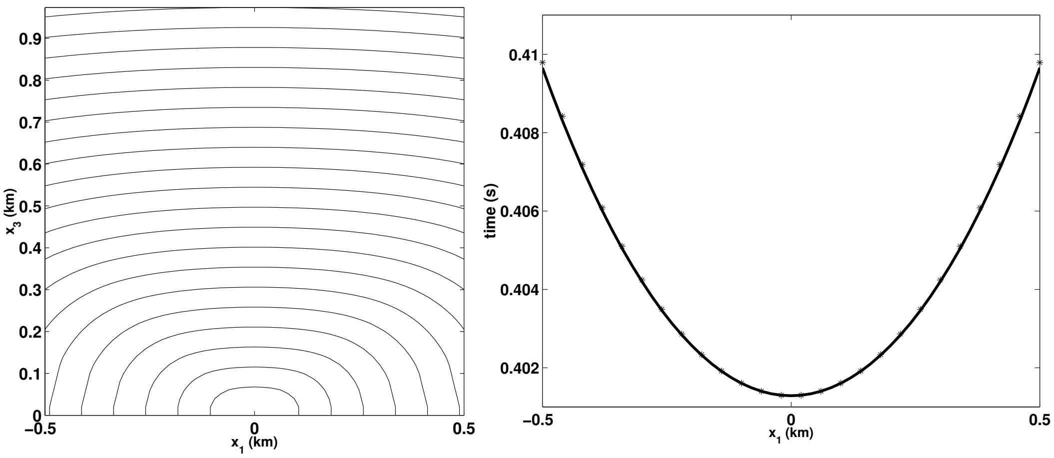

Figure 4.11 The 2-D homogeneous VTI Zinc model with a second-order ENO scheme. The source is located at $x_1 = x_3 = 0.0$; the initial depth is 0.02km and $\Delta x_1 = \Delta x_3 = 0.02$km. Left: traveltime contours by the paraxial eikonal solver with the ENO scheme. Right: the traveltime calibration at $x_3 = 1$km.

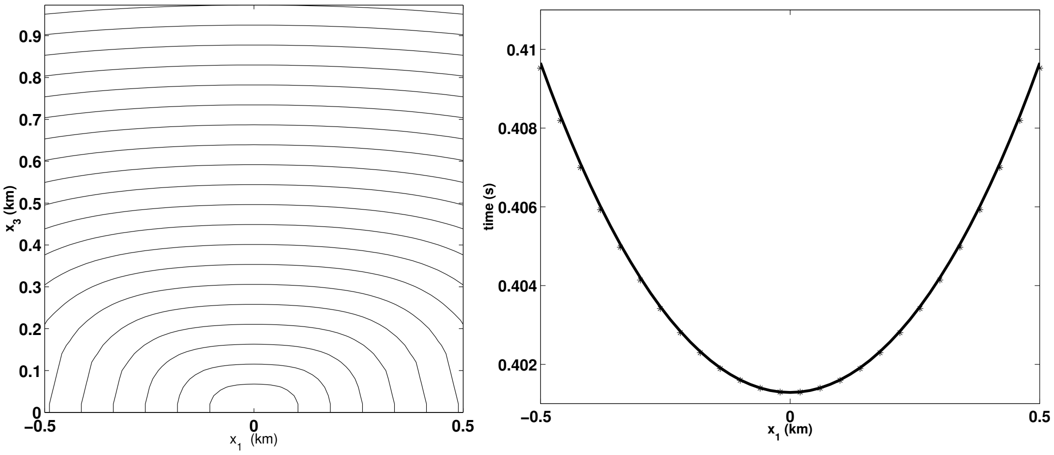

Figure 4.12 The 2-D homogeneous VTI Zinc model with a second-order WENO scheme. The source is located at $x_1 = x_3 = 0.0$; the initial depth is 0.02km and $\Delta x_1 = \Delta x_3 = 0.02$km. Left: traveltime contours by the paraxial eikonal solver with the WENO scheme. Right: the traveltime calibration at $x_3 = 1$km.

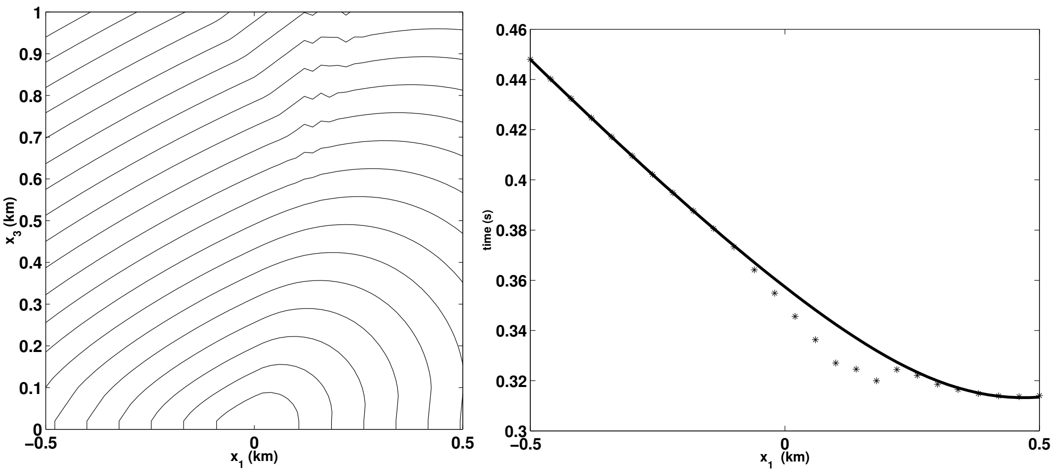

Figure 4.13 The 2-D homogeneous inclined (30 degrees) TI Zinc model with a 2nd-order ENO scheme. The source is located at $x_1 = x_3 = 0.0$; the initial depth is 0.02km and $\Delta x_1 = \Delta x_3 = 0.02$km. Left: traveltime contours by the paraxial eikonal solver with the ENO scheme. Right: the traveltime calibration at $x_3 = 1$km.

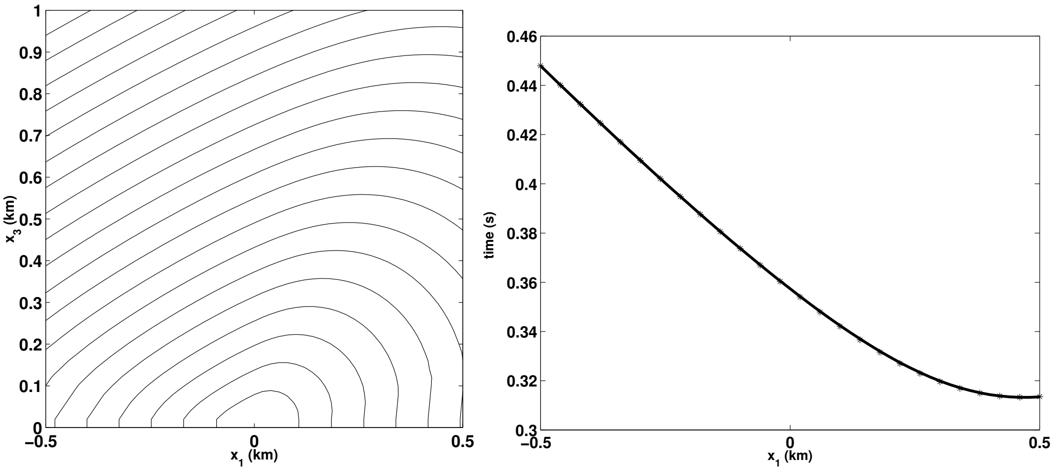

Figure 4.14 The 2-D homogeneous inclined (30 degrees) TI Zinc model with a 2nd-order WENO scheme. The source is located at $x_1 = x_3 = 0.0$; the initial depth is 0.02km and $\Delta x_1 = \Delta x_3 = 0.02$km. Left: traveltime contours by the paraxial eikonal solver with the WENO scheme. Right: the traveltime calibration at $x_3 = 1$km.

Chapter 5

Amplitude Computations by Adaptive Gridding

Extensive numerical experiments in Chapter 4 have shown that the proposed algorithms compute the traveltime (phase function) accurately and efficiently. To construct the geometrical optics term, nevertheless, the amplitude function is needed as well. Because the amplitude function is related to the second-order derivatives of the phase function (i.e., the curvature of the wavefront), the accuracy of the computed amplitude is sensitive to the errors (noises) of the numerical phase function. In other words, the accuracy of the computed amplitude is determined by that of the computed traveltime. Therefore, if the amplitude is required to be of first-order accuracy, the numerical traveltime should be of at least third-order accuracy. However, for point-source problems, the traveltime field has an upwind singularity at the source. To obtain a highly accurate traveltime field, this singularity must be treated appropriately. The "recipe" is adaptive gridding borrowed from numerical methods of ODEs. To better understand the adaptive gridding for the eikonal equation and the dependence of the amplitude upon the traveltime, I will start from the simplest model, i.e., the isotropic solids. Finally, I will treat the VTI model as well.

5.1 Geometrical optics for isotropic solids

Because the isotropic solid is a special case of anisotropic solids, the traveltime field in an isotropic solid also satisfies an eikonal equation. Here I consider the two-dimensional case, so I use x and z rather than x_1 and x_3 to denote the coordinate variables. Denote by (x_s, z_s) the coordinates of a source point, and by (x, z) the coordinates of a general point in the subsurface. The first-arrival traveltime field

$\tau(x,z;x_s,z_s)$ is the viscosity solution of the eikonal equation

$$\left(\frac{\partial\tau}{\partial x}\right)^2+\left(\frac{\partial\tau}{\partial z}\right)^2 \;=\; s^2(x,z) \tag{5.1}$$

with the initial condition

$$\lim\left(\frac{\tau(x,z;x_s,z_s)}{\sqrt{(x-x_s)^2+(z-z_s)^2}}-\frac{1}{v(x,z)}\right) \;=\; 0$$

as $(x,z)\rightarrow(x_s,z_s)$, where v is the velocity, and $s=\dfrac{1}{v}$ is the slowness (Lions [Lio82]).

Since the isotropic solid is a special case of the VTI solid, the paraxial eikonal equation reads (Gray and May [GM94]):

$$\frac{\partial\tau}{\partial z}=H_{\theta_{\max}}\left(\frac{\partial\tau}{\partial x}\right) \;=\; \sqrt{\mathrm{smmax}\left(s^2-\left(\frac{\partial\tau}{\partial x}\right)^2, s^2\cos^2\theta_{\max}\right)}, \tag{5.2}$$

where smmax is a smoothed max function with $a>0$,

$$\mathrm{smmax}(x,a) \;=\; \begin{cases} \frac{1}{2}a & \text{if } x<0,\\ \frac{1}{2}a+2\frac{x^4}{a^3}(1-\frac{4}{5}\frac{x}{a}) & \text{if } 0\le x<\frac{a}{2},\\ x+2\frac{(x-a)^4}{a^3}(1+\frac{4}{5}\frac{x-a}{a}) & \text{if } \frac{a}{2}\le x<a,\\ x & \text{if } x\ge a.\end{cases}$$

Equation (5.2) defines a stable nonlinear evolution in z, suitable for explicit finite-difference discretization. The smoothed max function makes the numerical Hamiltonian smooth enough so that the standard truncation error analysis can be carried out for schemes of up to third-order accuracy. The solution τ is identical to the solution of the eikonal equation provided that the ray makes an angle $\le\theta_{\max}<\frac{\pi}{2}$ with the vertical.

Based on the traveltime computed by solving the paraxial eikonal equation, I can approximate the amplitude field by solving a transport equation. The amplitude satisfies the transport equation (Cerveny et. al. [CMP77]:

$$\nabla\tau\cdot\nabla A+\frac{1}{2}A\nabla^2\tau \;=\; 0. \tag{5.3}$$

The equation (5.3) is a first-order advection equation for the amplitude A. The Laplacian of the traveltime field is involved in this advection equation, which implies that a third-order accurate traveltime field is needed to get a first-order accurate amplitude field (Symes [Sym95], El-Mageed [EM96], El-Mageed et. al. [EMKS97]).

For convenience in the following presentation, I first introduce the ray coordinates. The ray coordinates are defined by $(\tau, \phi) = (\tau(x, z; x_s, z_s), \phi(x, z; x_s, z_s))$, where τ and ϕ are the traveltime and take-off angle of a ray from source point (x_s, z_s) to a general point (x, z) in the subsurface, respectively. In two-dimensional isotropic media with a line source, the amplitude also satisfies the formula (Friedlander [Fri58])

$$\begin{aligned} A(x, z) &= \frac{v(x_s, z_s)}{2\pi\sqrt{2}\sqrt{|J|}} \\ &= \frac{v(x_s, z_s)}{2\pi\sqrt{2}}\sqrt{|\nabla\tau \times \nabla\phi|}, \end{aligned} \tag{5.4}$$

where $J(x, z; x_s, z_s)$ is the Jacobian of the transformation from Cartesian coordinates (x, z) to ray coordinates (τ, ϕ). The Jacobian J can be computed by

$$J = \begin{vmatrix} \frac{\partial x}{\partial \tau} & \frac{\partial z}{\partial \tau} \\ \frac{\partial x}{\partial \phi} & \frac{\partial z}{\partial \phi} \end{vmatrix} = \begin{vmatrix} \frac{\partial \tau}{\partial x} & \frac{\partial \tau}{\partial z} \\ \frac{\partial \phi}{\partial x} & \frac{\partial \phi}{\partial z} \end{vmatrix}^{-1} = \frac{1}{\nabla\tau \times \nabla\phi}, \tag{5.5}$$

where $\nabla\phi$ and $\nabla\tau$ are the gradients of the takeoff angle and the traveltime, respectively.

Since the take-off angle ϕ is constant along any ray,

$$\nabla\tau \cdot \nabla\phi = \frac{\partial \tau}{\partial x}\frac{\partial \phi}{\partial x} + \frac{\partial \tau}{\partial z}\frac{\partial \phi}{\partial z} = 0. \tag{5.6}$$

That is, for an isotropic solid, the wavefront normal $\nabla\tau$ is tangential to the ray and thus is pointing to the ray velocity direction; the gradient $\nabla\phi$ is tangential to the wavefront. Equation (5.6) is slightly easier to solve numerically than equation (5.3) because no second-order traveltime derivatives are explicitly involved in the equation

(5.6). Having solved equation (5.6) for ϕ, one produces the amplitude A through (5.4).

Since the typical seismic source is a point source, I need to compensate for the out-of-plane radiation in the two-dimensional (2-D) line-source amplitude formula. The 2-D amplitude with a point source (2.5-D amplitude) can be computed by

$$A(x,z) \quad = \quad \frac{v(x_s,z_s)}{4\pi}\sqrt{\tau_{yy}|\nabla\tau\times\nabla\phi|}, \tag{5.7}$$

where the out-of-plane curvature τ_{yy} satisfies another advection equation (Symes et. al. [SVST94]):

$$\frac{\partial\tau}{\partial x}\frac{\partial\tau_{yy}}{\partial x}+\frac{\partial\tau}{\partial z}\frac{\partial\tau_{yy}}{\partial z}+\tau_{yy}^2=0. \tag{5.8}$$

Supposing that the amplitude is required to be first-order accurate, then the two gradients $\nabla\tau$ and $\nabla\phi$ involved in the amplitude formulae should have at least first-order accuracy. However, because $\nabla\phi$ depends on second-order derivatives of traveltime τ, it implies that to get a first-order accurate $\nabla\phi$, the traveltime τ itself should have at least third-order accuracy. The final conclusion is that a third-order traveltime solver is required to get first-order accurate amplitudes, as noted before.

Zhang [Zha93] used equation (5.7) in polar coordinates to compute the geometrical spreading factor, but his computation of the takeoff angle was based on the first-order traveltime field. Consequently, the gradient of take-off angle computed by his scheme was inaccurate. Vidale and Houston [VH90] encountered a similar difficulty.

5.2 High-order WENO Runge-Kutta schemes

As presented in Chapter 3, ENO and WENO schemes are used for the following reasons: (1) stable schemes of arbitrarily high-order accuracy exist, permitting accurate solutions on coarse grids (a factor which is critical to the mesh refinement or coarsening); (2) versions exist in any dimension so that the methodology can be straightforwardly extended to the three-dimensional case.

All of these schemes take the form of recursive depth stepping rules,

$$\tau \leftarrow \tau + \delta_j^j \tau, \tag{5.9}$$

$$z \leftarrow z + \Delta z. \tag{5.10}$$

Here δ_j^j is a nonlinear update operator expressing the WENO-Runge-Kutta rule of order j, depending on Δz, Δx and the slowness field s, and defining a difference scheme of formal jth-order accuracy. The detailed forms of δ_j^j $(j = 2, 3)$ have been shown in Chapter 3.

Similarly, I solve the advection equation for the takeoff angle ϕ and the out-of-plane curvature τ_{yy} by using WENO schemes; see Appendix C for details.

5.3 Adaptive gridding for the upwind singularity at sources

To initialize our algorithm, the user supplies a local error tolerance ε; σ_1 and σ_2 are two user-defined positive functions of ε which are used to control the coarsening and refinement. For example, take $\sigma_1 = 0.1\varepsilon$ and $\sigma_2 = \varepsilon$. I use the 2nd and 3rd order eikonal solvers [equations (3.27) and (3.28] for the two-dimensional case) and estimate the truncation error of the 2nd-order scheme as $e_2 = \max|\delta_2^2\tau - \delta_3^3\tau|$ over the current depth. So long as $\sigma_1(\varepsilon) \leq e_2 \leq \sigma_2(\varepsilon)$ at every point of the current depth level, simply proceed to the next step; it is well known and explained in Gear [Gea71] that an efficient adaptive stepping requires rather loose control of the local error. When $e_2 < \sigma_1(\varepsilon)$, the step is increased by a factor of two, i.e., $\Delta z \leftarrow 2\Delta z$, and the τ update and e_2 are recomputed. Similarly, when $e_2 > \sigma_2(\varepsilon)$, the step is decreased by a factor of two. As soon as the local error is once again within the tolerance interval, the depth-stepping is continued. A very important point is that I retain the 3rd-order (a more accurate one) computation of τ at the end of each depth step as the actual update, discarding the 2nd-order computation, which is used only in step control.

The usual step adjustment in ODE solvers would change Δz by a factor computed from the asymptotic form of the truncation error (Stoer and Bulirsch [SB92], p 449). This is impractical for a PDE application because it would require an arbitrary adjustment of the spatial grid (i.e., the x-grid in the difference scheme) and, therefore, expensive interpolation. Scaling Δz by a factor of two, however, implies that the stability may be maintained by scaling Δx by the same factor. For coarsening, this means simply throwing out every other grid point, i.e., no interpolation at all, which dramatically reduces the floating point operations required. Since the typical behavior of the traveltime field is to become smoother as one moves away from the source, the truncation errors tend in general to decrease. Therefore, most of the grid adjustments are coarsenings and very little or no interpolation is required. Since the slowness field comes in a gridded form, an interpolation is always required to supply estimates of slowness at the points appearing in the WENO-Runge-Kutta formula. A local quadratic interpolation in x and z is used, the third-order accuracy of which is compatible with that of the difference scheme.

Since the traveltime field is nonsmooth at the source point, the truncation error analysis on which the adaptive step selection criterion is based is not valid there. Therefore, it is necessary to produce a smooth initial traveltime field. I do this by estimating the largest $z_{\text{init}} > 0$ at which the constant velocity traveltime is in error by less than $\sigma_2(\varepsilon)$. Details of the z_{init} calculation are given in Appendix D. Having initialized τ at z_{init}, the algorithm invokes adaptive gridding. Since z_{init} is quite small, τ changes rapidly, resulting in a large number of grid refinements at the outset. However, no interpolation is performed, as τ is given analytically on $z = z_{\text{init}}$. This initially very fine grid is rapidly coarsened as the depth stepping proceeds.

In the current implementation, I maintain a data structure for the computational grid that is independent of the output grid; the desired quantities are calculated on the computational grid and interpolated back to the output grid. As a safeguard against pathological program behaviors, such as the number of grid refinements being very large, a maximum number of permitted grid refinements, MAXREF, is specified.

A simplified algorithm framework is as follows:

- Input ε, x_s, z_s, $\theta_{\max}$, Δz, MAXREF.
- Initialize Δx, τ, $z = z_{\text{init}}$, REF $= 0$.
- Do while $z <$ target depth,
  - compute $e_2 = \max |\delta_2^2 \tau - \delta_3^3 \tau|$ over the current depth level z ;
  - if $e_2 \le \sigma_1(\varepsilon)$ and REF > 0,
    * $\Delta z \leftarrow 2\Delta z$,
    * $\Delta x \leftarrow 2\Delta x$,
    * REF $\leftarrow$ REF $- 1$,
    * upsample τ (throw out every other point).
  - else if $e_2 \ge \sigma_2(\varepsilon)$ and REF $\le$ MAXREF,
    * $\Delta z \leftarrow \Delta z/2$,
    * $\Delta x \leftarrow \Delta x/2$,
    * REF $\leftarrow$ REF $+ 1$,
    * downsample τ (interpolate)
  - else
    * $z \leftarrow z + \Delta z$,
    * $\tau \leftarrow \tau + \delta_3^3 \tau$.

- end if

- end do

This description leaves out the output step of the algorithm: a full implementation monitors the depth level of the next set of output points and quadratically interpolates the traveltime field onto them as soon as z passes this depth, using the current and last two depth levels of τ. Local quadratic interpolation preserves the third-order accuracy of the computed τ.

To avoid unnecessary computations, the algorithm updates τ only within the triangle $\{(x,z) : |x - x_s| \leq |z - z_s| \tan\theta_{\max}\}$. All rays with takeoff angles less than $\theta_{\max}$ must lie inside this triangle, and it is only along such rays that the paraxial eikonal equation produces correct first-arrival times. Output points outside the triangle are assigned $\tau = \mathrm{MAX.FLOAT}$. Since times at output points which are inside the triangle but not lying on rays with takeoff angles less than $\theta_{\max}$ also receive erroneous time values, they must be washed out of any subsequent computations. For high frequency asymptotics computations, this masking is most easily accomplished by zeroing the geometrical amplitude at such points.

5.4 Numerical experiments, I: isotropic solids

To illustrate how the adaptive-gridding approach works, I test the method on a constant velocity model, $v = 1\mathrm{km/s}$, with two-dimensional geometry

$$\{(x,z) : -0.5\mathrm{km} \leq x \leq 0.5\mathrm{km}, 0 \leq z \leq 1.0\mathrm{km}\},$$

in which case the behaviors of traveltime fields and amplitude fields are well understood.

In the constant velocity case, all the desired quantities have obvious analytical solutions to compare against the computed solutions. I compare the results obtained by fixed- and adaptive- grid algorithms. Both algorithms use a third-order WENO scheme to compute τ: the adaptive-grid scheme uses a second-order ENO scheme for local truncation error estimation. The ouput grid is 51×51 with $\Delta x = \Delta z = 0.02$. For adaptive-grid algorithms, MAXREF is set to be 5 with the coarsest grid 17×17, $\sigma_1 = 0.1\varepsilon$ and $\sigma_2 = \varepsilon$.

Table 5.1 shows the traveltime error and computation cost by the fixed grid, and Table 5.2 shows the traveltime error and computation cost by the adaptive grid, where Flops denote the number of floating point operations. The error is the maximum absolute error at the bottom row of the gridpoints ($z = 1$km). Because the computed portion of this depth level (-0.5km$\leq x \leq 0.5$km) lies entirely within the computation aperture ($\theta_{\max} = 78$ degrees), it consists of accurately computed τ values. From the two tables, it is easy to see that to reach the same level of accuracy, the adaptive-gridding approach requires an order of magnitude lower computational cost than does the fixed-gridding approach.

Figure 5.1 shows the traveltime contours produced by the two approaches. No difference can be seen from the figure because, on the one hand, the fixed-gridding algorithm still has first-order accuracy, and on the other hand, the resolution of the graphics is limited. Figure 5.2 shows contours of τ_x computed by two approaches. It can be seen that τ_x by the fixed grid is oscillating, but τ_x by the adaptive grid traveltime solver is convergent. Similar phenomena are observed for τ_z, as shown in Figure 5.3. Because the fixed-gridding approach produces only a first-order accurate

Table 5.1 Fixed-grid eikonal solver: a constant velocity model

dx	Abs.Err(τ, dx)(s)	$Flops$
0.01	0.001232	261,590
0.00125	0.000219	16,632,765

Table 5.2 Adaptive-grid eikonal solver: a constant velocity model

ε	Abs.Err(τ, dx)(s)	$Flops$
0.000025	0.001041	39,815
0.00000169	0.000160	928,770

traveltime field, the resultant traveltime derivatives have only zero-order accuracy and exhibit oscillations which do not decrease in magnitude as the grid is refined, as shown in Figure 5.2 (left) and Figure 5.3 (left). However, the adaptive-gridding approach yields far more accurate traveltime fields; thus the traveltime derivatives are still accurate, as shown in Figure 5.2 (right) and Figure 5.3 (right).

Now I discuss the takeoff angle and its derivatives. Figure 5.4 shows contours of the takeoff angle ϕ by two approaches. Because the coefficients in the advection equation for takeoff angles depend on the traveltime gradient, the accuracy of ϕ is decided by the utilized traveltime solver. Since the first-order traveltime field from the fixed-gridding approach results in inaccurate $\nabla\tau$, the resultant takeoff angle is inaccurate, as shown in Figure 5.4 (left). However, the takeoff angle based on the traveltime field from the adaptive-gridding approach is accurate, as shown in Figure 5.4 (right). Figure 5.5 shows ϕ_x by the two approaches. Because the takeoff angle based on the traveltime field from the fixed-gridding approach is inaccurate, the resultant derivatives ϕ_x are divergent, as shown in Figure 5.5 (left). However, the adaptive-gridding approach produces accurate traveltime gradients, which leads to the convergent ϕ_x, as shown in Figure 5.5 (right). Similar observations hold for ϕ_z, as shown in Figure 5.6.

To further illustrate the differences of the accuracy between two approaches, Figures 5.7 and 5.8 show the distribution of relative errors along the depth direction for ϕ_x and ϕ_z. The error along the depth direction is defined as

$$e(z) \quad = \quad \frac{\max_{-0.5\leq x\leq 0.5} |f^{\mathrm{comp}}(x,z) - f^{\mathrm{ana}}(x,z)|}{\max_{-0.5\leq x\leq 0.5} |f^{\mathrm{ana}}(x,z)|} \tag{5.11}$$

where f^{comp} is the computed solution, and f^{ana} the analytic solution. For instance, substituting f with ϕ_x in Equation (5.11), I get the error distribution for ϕ_x along the depth direction. From Figure 5.7 and Figure 5.8, I can conclude that the adaptive-gridding approach produces much more accurate $\nabla\phi$ than does the fixed-gridding approach. The resultant amplitudes with a line source based on $\nabla\tau$ and $\nabla\phi$ by the two approaches are shown in Figure 5.9. The amplitude in Figure 5.9 (left) is divergent by the fixed-gridding approach, but the amplitude in Figure 5.9 (right) is accurate by the adaptive-gridding approach. Note the episodic nature of the convergence for the adaptive-gridding algorithms. Because I have allowed the local error estimate to vary by an order of magnitude before adjusting the grid and then permitted only step changes by factors of 2, the error exhibits "sticky," discontinuous behaviour.

Finally, Figure 5.10 shows the computational results for the out-of-plane curvature τ_{yy} and the amplitude field with a point source by the adaptive-gridding approach. The computed τ_{yy} is accurate and the resultant amplitude is convergent.

To test the robustness of the new adaptive-gridding WENO approach on synthetic models, I have embedded the new adaptive-grid traveltime and amplitude solver in 2-D Kirchhoff prestack migration and inversion code (Symes et. al. [SVST94]). Figure 5.11 shows the impulse response of the inversion by an ENO third-order eikonal solver, where the Beylkin determinant required by the inversion is computed by using the information from traveltimes and takeoff angles. The impulse response is not smooth because the numerical derivative τ_x generated by ENO schemes is not guaranteed to be continuous. Figure 5.12 shows the impulse response of the inversion for a WENO third-order eikonal solver, where the Beylkin determinant required by the inversion is computed by using the information from traveltimes and takeoff angles. The impulse response is smooth as expected because the numerical derivative τ_x generated by WENO schemes is continuous.

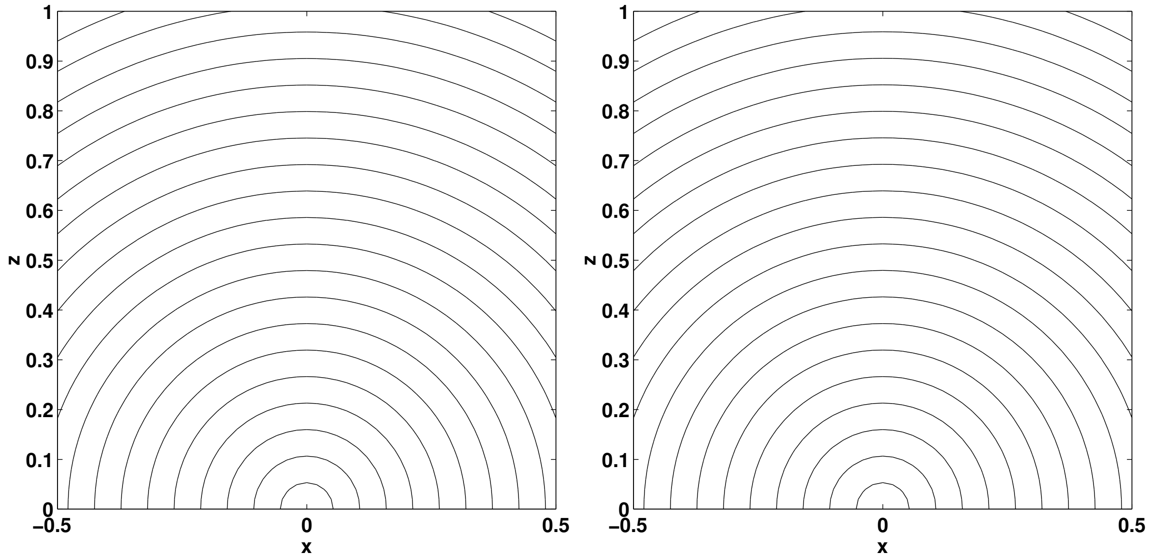

Figure 5.1 Traveltime contours for a constant velocity model. Left: fixed grid. Right: adaptive grid.

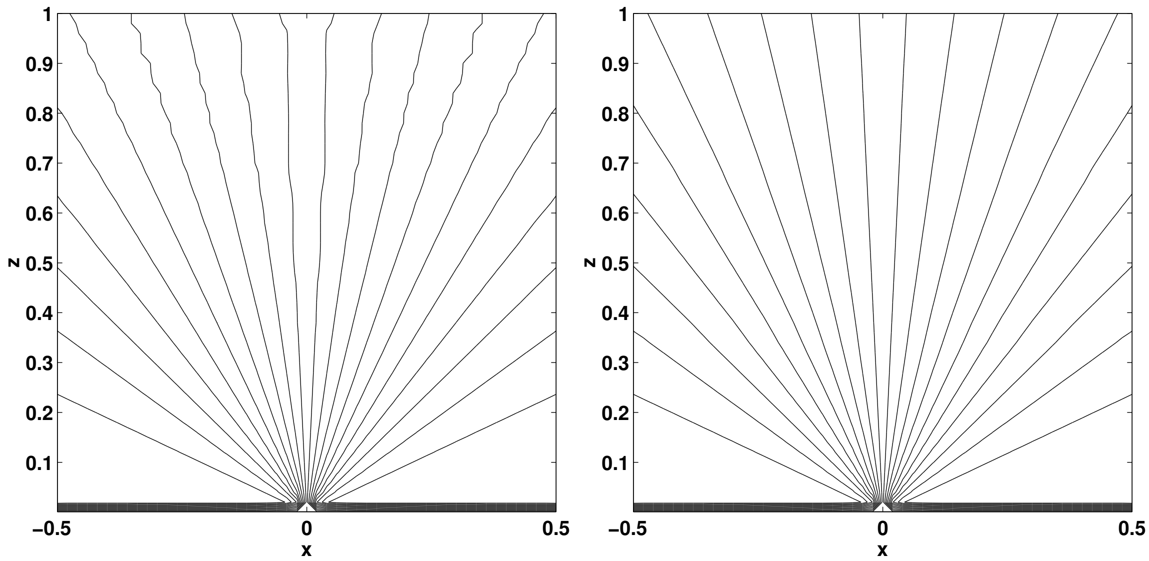

Figure 5.2 τ_x for a constant velocity model. Left: τ_x by fixed grid is oscillating. Right: τ_x by adaptive grid is convergent.

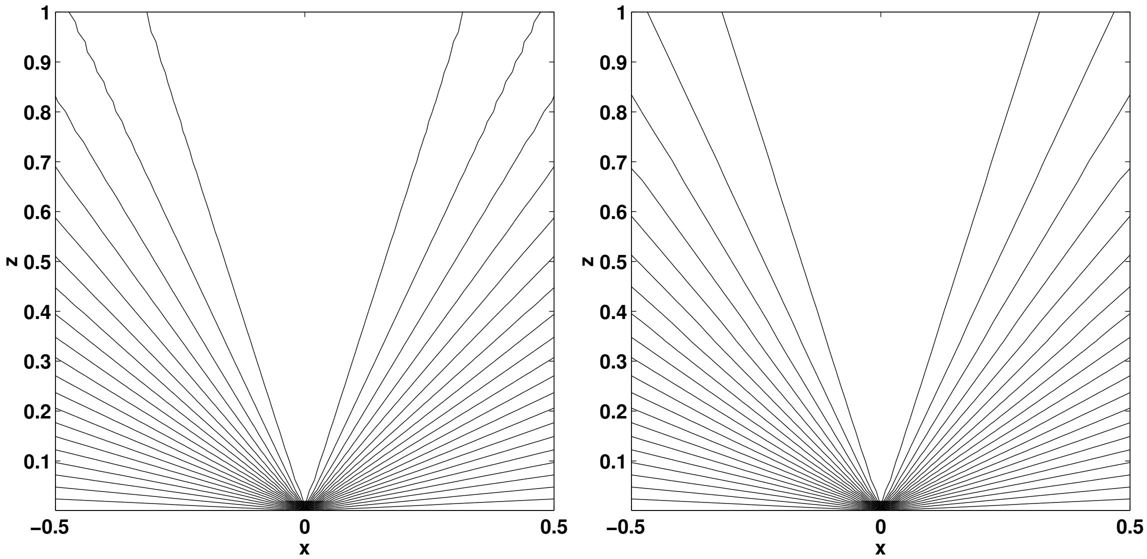

Figure 5.3 τ_z for a constant velocity model. Left: τ_z by fixed grid is oscillating. Right: τ_z by adaptive grid is convergent.

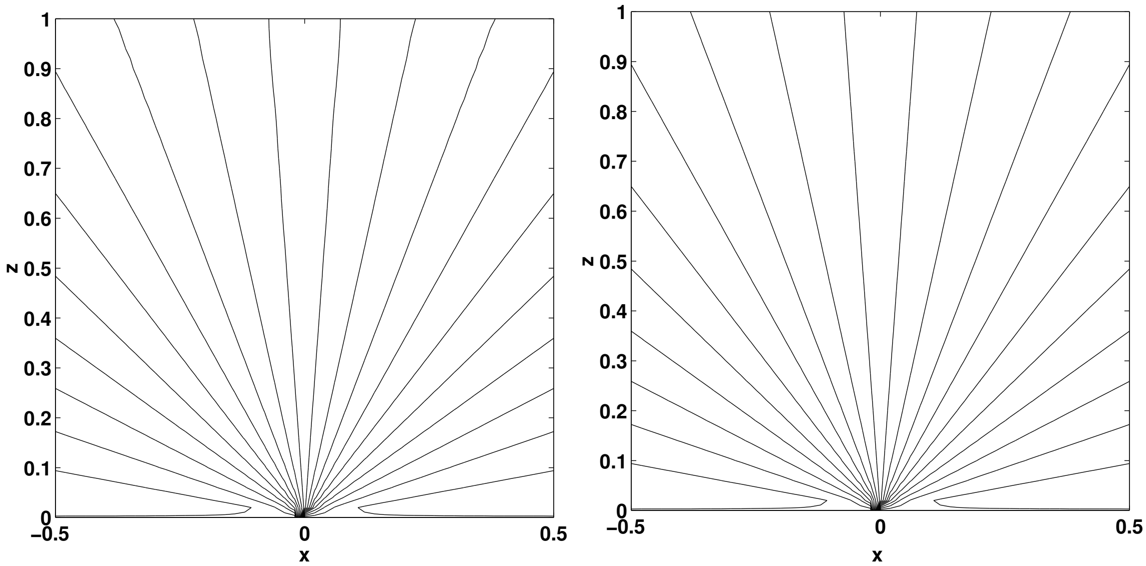

Figure 5.4 Takeoff angle ϕ for a constant velocity model. Left: ϕ by fixed grid is not accurate enough to be differentiated; notice the tiny oscillation on the upper part of the figure. Right: ϕ by adaptive grid is accurate enough to be differentiated.

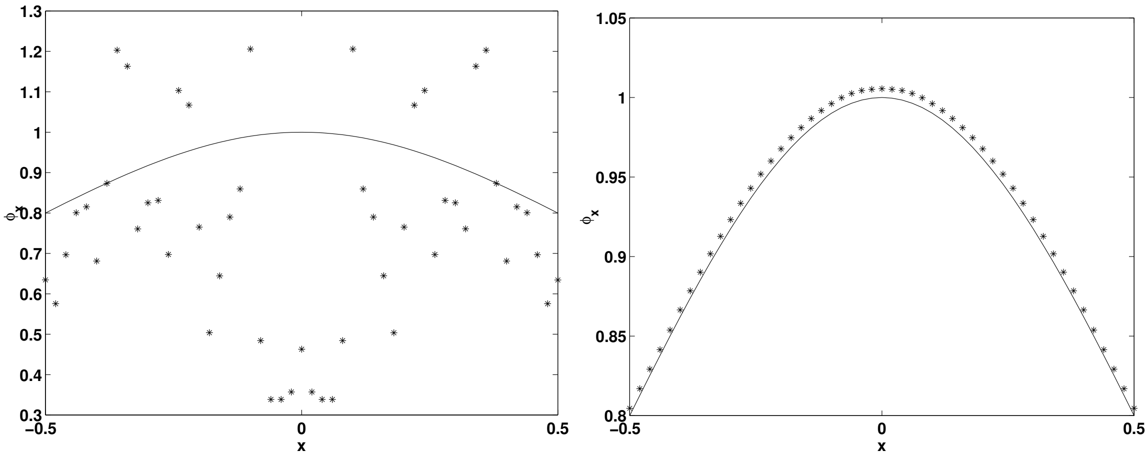

Figure 5.5 ϕ_x at $z = 1$ for a constant velocity model. Left: fixed grid; solid line (-): true solution; star (*): computed solution. Right: adaptive grid; solid line (-): true solution; star (*): computed solution.

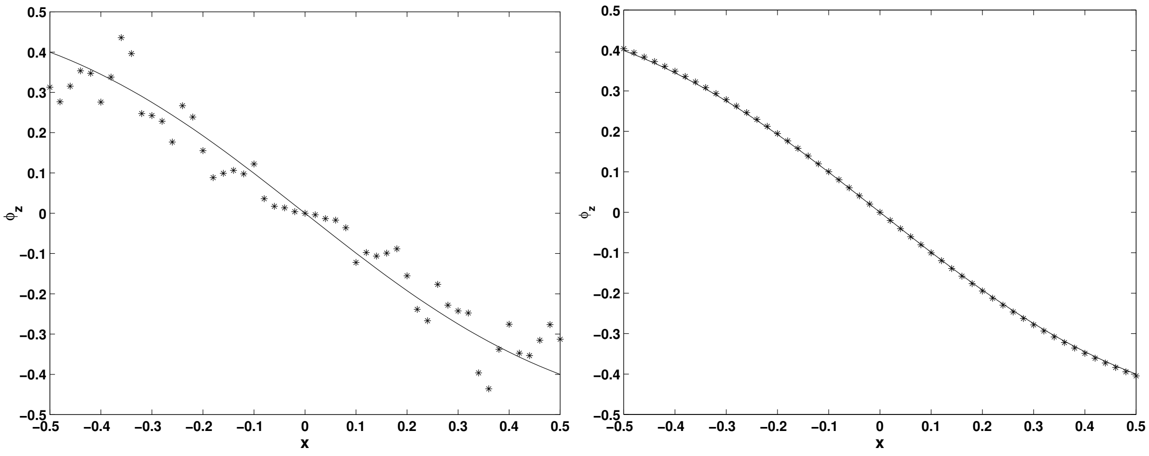

Figure 5.6 ϕ_z at $z = 1$ for a constant velocity model. Left: fixed grid; solid line (-): true solution; star (*): computed solution. Right: adaptive grid; solid line (-): true solution; star (*): computed solution.

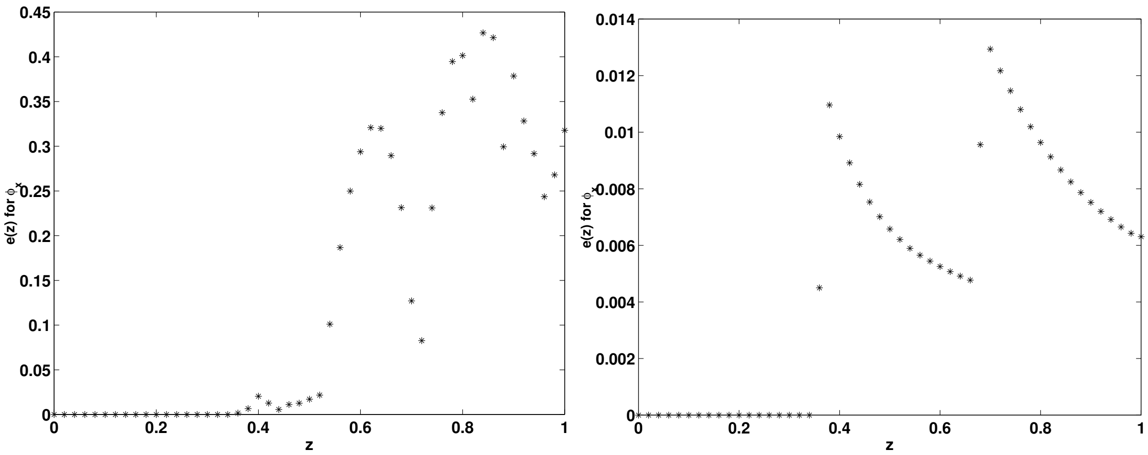

Figure 5.7 Relative errors in ϕ_x. Left: fixed grid, maximum relative error is almost 45 percent. Right: adaptive grid, maximum relative error is less than 1.5 percent.

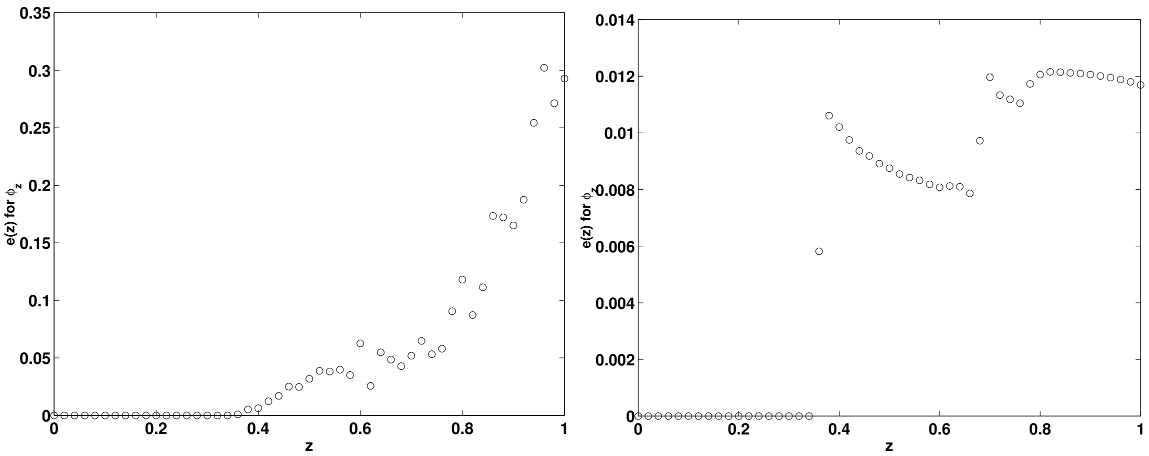

Figure 5.8 Relative errors in ϕ_z. Left: fixed grid, maximum relative error is almost 30 percent. Right: adaptive grid, maximum relative error is less than 1.5 percent.

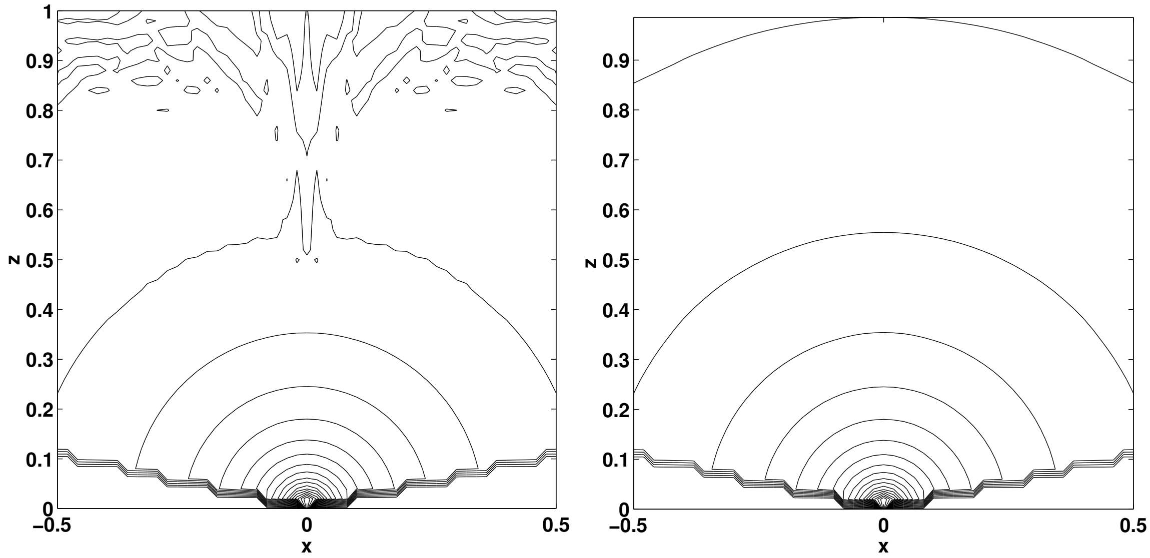

Figure 5.9 2-D amplitude with a line source for a constant velocity model. Left: the amplitude by fixed grid is divergent. Right: the amplitude by adaptive grid is convergent.

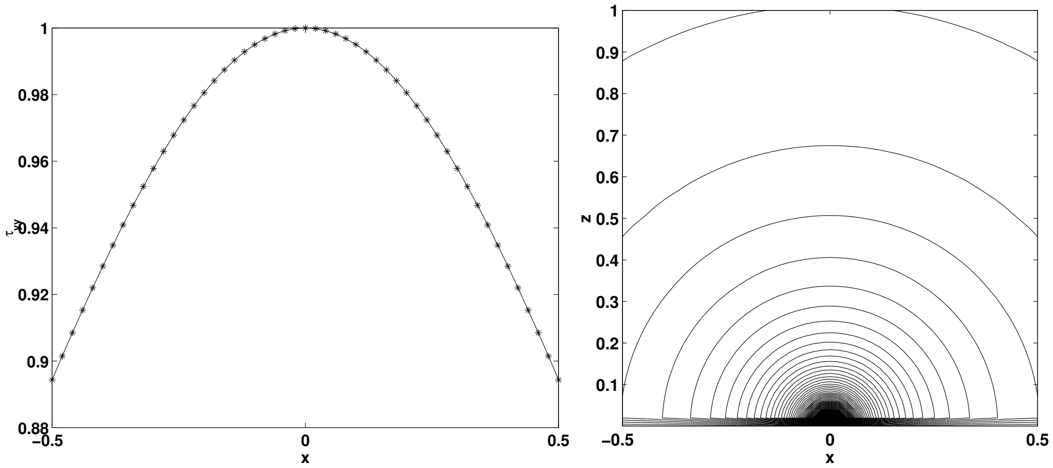

Figure 5.10 Left: τ_{yy} at $z = 1$ for a constant velocity model by adaptive grid; solid line (-): true solution; star (*): computed solution. Right: 2-D amplitude with a point source for a constant velocity model by adaptive grid.

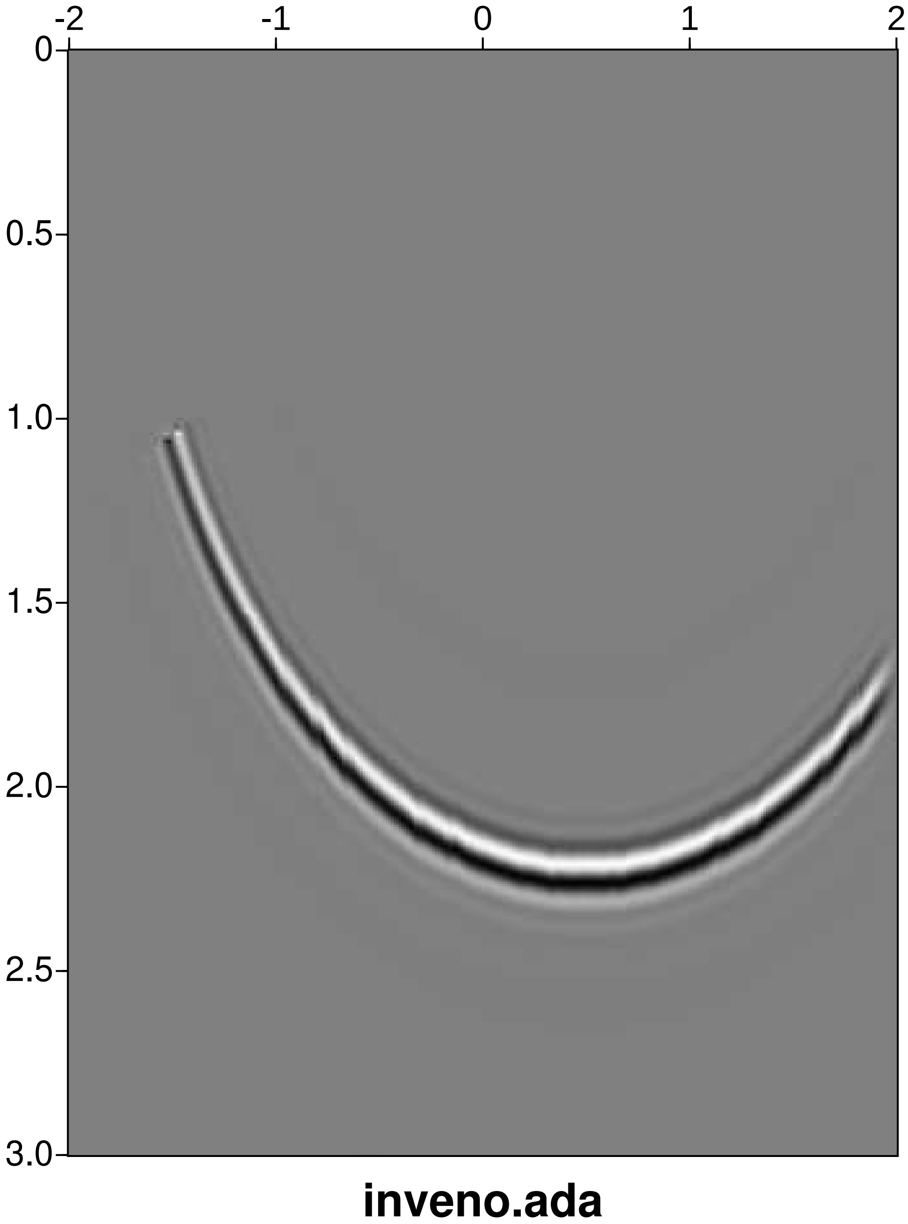

Figure 5.11 The impulse response by inversion with the adaptive-gridding ENO traveltime-amplitude solver. The response is not smooth because the numerical derivative τ_x generated by ENO schemes is not guaranteed to be continuous.

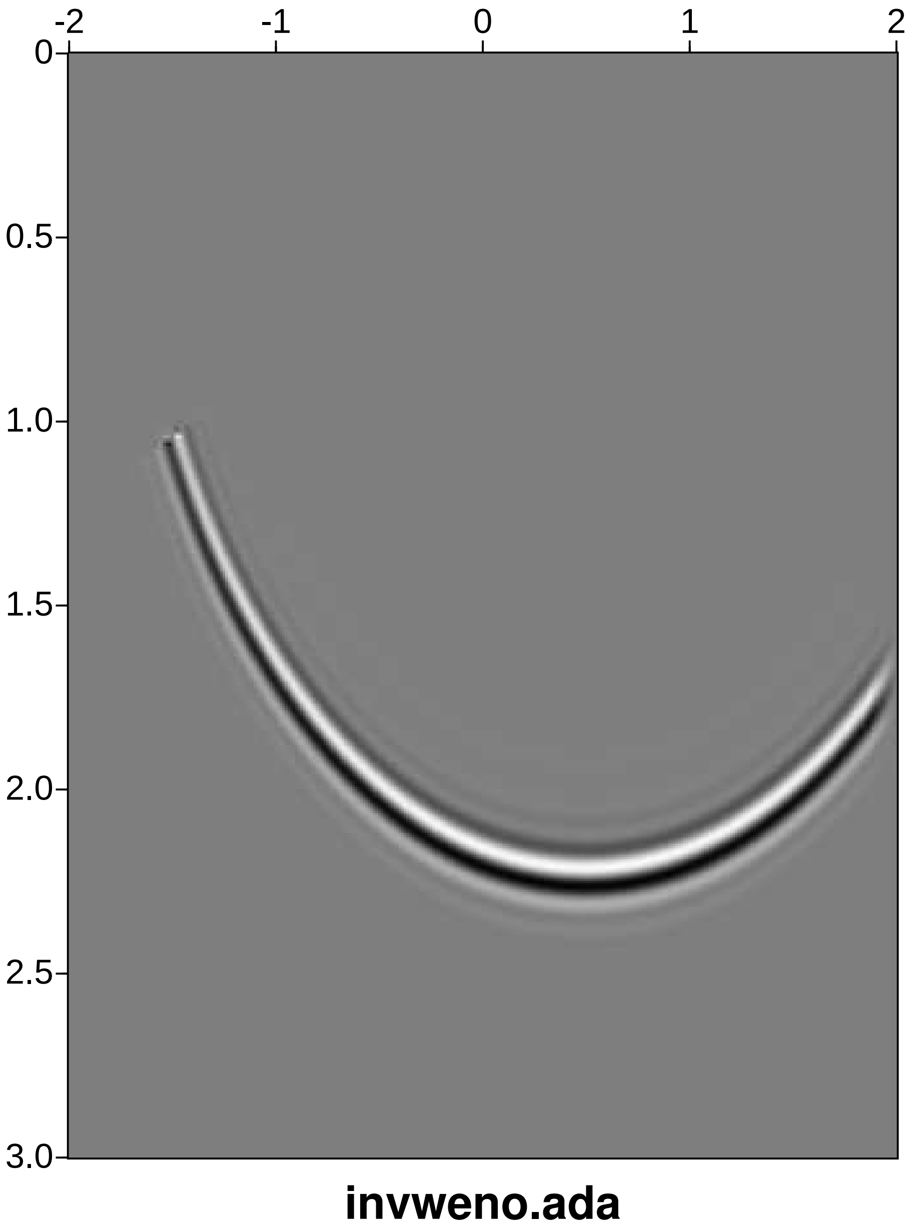

Figure 5.12 The impulse response by inversion with the adaptive-gridding WENO traveltime-amplitude solver. The response is smooth as expected because the numerical derivative τ_x generated by WENO schemes is continuous.

5.5 Geometrical optics for 2-D VTI solids

A paraxial eikonal equation for VTI is already presented in Chapter 4. To be suitable for using adaptive gridding, a smoothed version of equation (4.21) for 2-D VTI is utilized:

$$\frac{\partial\tau}{\partial z} = H_{\theta_{\max}}\left(\frac{\partial\tau}{\partial x}\right) = \sqrt{\mathrm{smmax}\left(\frac{2c}{-b+\sqrt{b^2-4ac}}, \frac{\cos^2(\theta_{\max})}{v_{qP}^2(\theta_{\max})}\right)}, \tag{5.12}$$

where

$$a \equiv \alpha_0^2\beta_0^2, \tag{5.13}$$

$$b \equiv 2\alpha_0^2\beta_0^2\left(1+\delta+(\epsilon-\delta)\frac{\alpha_0^2}{\beta_0^2}\right)\left(\frac{\partial\tau}{\partial x}\right)^2 - \alpha_0^2 - \beta_0^2, \tag{5.14}$$

$$c \equiv \left((1+2\epsilon)\alpha_0^2\left(\frac{\partial\tau}{\partial x}\right)^2 - 1\right)\left(\beta_0^2\left(\frac{\partial\tau}{\partial x}\right)^2 - 1\right), \tag{5.15}$$

with α_0, β_0, ϵ and δ being Thomsen's parameters [Tho86].

As presented in Chapter 2, a certain Jacobian from Cartesian coordinates to ray coordinates is needed in the amplitude computation. Here the ray coordinates are defined by

$$(\tau, q_1) = (\tau(x,z;x_s,z_s), q_1(x,z;x_s,z_s)), \tag{5.16}$$

where τ and q_1 are the traveltime and take-off angle of a ray from source point (x_s, z_s) to a general point (x, z) in the subsurface, respectively.

In two-dimensional anisotropic media with line sources, the amplitude satisfies the formula

$$\begin{aligned} A(x,z) &= \frac{R\left(q_1(x,z;x_s,z_s)\right)}{\sqrt{|J|}} \\ &= R\left(q_1(x,z;x_s,z_s)\right)\sqrt{|\nabla\tau \times \nabla q_1|}. \end{aligned} \tag{5.17}$$

In equation (5.17), R is the radiation pattern of the source and $J(x,z;x_s,z_s)$ is the Jacobian of the transformation from Cartesian coordinates (x, z) to ray coordinates

(τ, q_1). The Jacobian J can be computed by

$$J = \begin{vmatrix} \dfrac{\partial x}{\partial \tau} & \dfrac{\partial z}{\partial \tau} \\ \dfrac{\partial x}{\partial q_1} & \dfrac{\partial z}{\partial q_1} \end{vmatrix} = \frac{1}{\nabla \tau \times \nabla q_1}, \tag{5.18}$$

where ∇q_1 and $\nabla \tau$ are the gradients of the takeoff angle and the traveltime, respectively.

As derived in Chapter 2, the take-off angle q_1 satisfies an advection equation, which written in evolution form in depth is

$$\frac{\partial q_1}{\partial z} = -\frac{v_1}{v_3}\frac{\partial q_1}{\partial x}, \tag{5.19}$$

where for 2-D VTI

$$\begin{aligned} v_1 &= p_1(2\alpha_0^2(1+2\epsilon)\beta_0^2 p_1^2 + Bp_3^2 - \alpha_0^2(1+2\epsilon) - \beta_0^2)/D, & (5.20) \\ v_3 &= p_3(2\alpha_0^2\beta_0^2 p_3^2 + Bp_1^2 - \alpha_0^2 - \beta_0^2)/D, & (5.21) \end{aligned}$$

with

$$\begin{aligned} p_1 &= \frac{\partial \tau}{\partial x}, & (5.22) \\ p_3 &= \frac{\partial \tau}{\partial z}, & (5.23) \\ B &= 2\alpha_0^2(\alpha_0^2(\epsilon - \delta) + \beta_0^2(1+\delta)), & (5.24) \\ D &= 2 - (\alpha_0^2(1+\epsilon) + \beta_0^2)p_1^2 - (\alpha_0^2 + \beta_0^2)p_3^2. & (5.25) \end{aligned}$$

As in the isotropic case, I will use the adaptive-gridding approach for solving the paraxial eikonal equation (5.12). The technique for solving equation (5.6) shown in Appendix C could be modified to solve equation (5.19) as well, so the detail is omitted here.

5.6 Numerical experiments, II: VTI solids

To show that the adaptive-gridding strategy is efficient and accurate for anisotropic media as well, I demonstrate some numerical experiments for a two-dimensional VTI soild.

To compute the traveltime, the adaptive-gridding approach is used for solving the paraxial eikonal equation (5.12). To initialize the traveltime in homogeneous media, I use a modification of Algorithm 3.5, presented in Appendix B. Note that in the homogeneous anisotropic media the take-off angle and its derivatives have analytic forms, which I can use to calibrate the numerical results for the simple homogeneous media.

The example occupies the rectangle $\{-0.5 \text{ km} \leq x \leq 0.5 \text{ km}, 0 \leq z \leq 1 \text{ km} \}$; the source is located at $x_1 = 0.0$ km, $x_3 = 0.0$ km. The four Thomsen's parameters of homogeneous Green River Shale are

$$\begin{aligned} \alpha_0 &= 3.330\text{km/s}, \\ \beta_0 &= 1.768\text{km/s}, \\ \epsilon &= 0.195, \\ \delta &= -0.220. \end{aligned}$$

Because the parameter δ has the same magnitude as ϵ, the near-vertical anisotropic response is dominated by δ (Thomsen [Tho86]); hence I use this example to demonstrate not only the accuracy of the adaptive-gridding approach, but also the capability of the approach in capturing the anisotropy of wave propagation.

The grid sampling size is $\Delta x = \Delta z = 0.01$km. The adaptive-gridding approach has a computational grid which is independent of the output grid. For the adaptive gridding, MAXREF is set to 5 with the coarsest grid 17×17, and the error tolerance is set to be 0.0001. To simplify the implementation for weak VTI media, I set the radiation pattern of the source to be constant (as stated in Chapter 2, I need to solve a nonlinear equation to get the anisotropic radiation pattern of the source, and it is left as a future topic). The computational results are shown in Figures 5.12 to 5.18.

Figure 5.12 (left) is the traveltime contours of the 2-D VTI model, and the anisotropic effects on the wave propogation are evident. Figure 5.12 (right) is the traveltime calibration at the bottom $z = 1$km for the adaptive-gridding approach by using a simplified version of Algorithm 3.5, presented in Appendix B; the comparison shows that the traveltimes by different approaches match very well.

Figure 5.13 (left) is the contours of derivatives $\frac{\partial \tau}{\partial x}$ computed by the adaptive-gridding approach. Figure 5.13 (right) is the calibration result for $\frac{\partial \tau}{\partial x}$. The analytical solution is computed by using the algorithm presented in Appendix B, and the two computed derivatives match very well. Similar observations hold for derivatives $\frac{\partial \tau}{\partial z}$; see Figure 5.14.

Now I will discuss the computational results for the takeoff angle and its derivatives. Figure 5.15 (left) is the contours for the takeoff angles by the adaptive-gridding approach; the contours are straight lines because the rays in homogeneous anisotropic media are still straight. The analytical solution for takeoff angles has an explicit form now, therefore the calibration in Figure 5.15 (right) shows that the takeoff angle computed by the adaptive-gridding approach is accurate.

Figure 5.16 (left) is the contours of derivatives $\frac{\partial q_1}{\partial x}$ computed by the adaptive-gridding approach. Figure 5.16 (right) is the calibration result at the bottom $z = 1$km for the adaptive-gridding approach by using the analytical solution. Because $q_1 = 0$ is a sonic point where the accuracy of numerical derivatives $\frac{\partial q_1}{\partial x}$ is poor, this inaccuracy is observed near the apex in Figure 5.16 (right). Away from the sonic point, the adaptive-gridding solution and analytic solution match very well. Figure 5.17 (left) is the contours of derivatives $\frac{\partial q_1}{\partial z}$ computed by the adaptive-gridding approach.

Figure 5.17 (right) is the calibration result at the bottom $z = 1$km for the adaptive-gridding approach by using the analytical solution, and the result demonstrates that the numerical derivatives $\dfrac{\partial q_1}{\partial z}$ is accurate.

Finally, Figure 5.18 shows the amplitude field computed by the adaptive-gridding WENO approach. The amplitude field is smooth as expected.

The computational results have shown that the adaptive-gridding approach works very well for the traveltime and amplitude computation of the VTI solid. I expect that the approach can handle the traveltime and amplitude computation of the general anisotropic media as well.

5.7 Closing comments

The adaptive-gridding strategy requires an *a posteriori* estimate of the local truncation error to perform grids adjustment. Since the traveltime field, the solution of an eikonal equation, behaves in a predictable way as established in Belfi and Symes [BS98], a pair of finite-difference schemes of different orders can effectively predict the local errors. However, for general nonlinear partial differential equations, it is not a simple task to obtain an *a posteriori* error estimate; see Cockburn [Coc98] for the discussion on nonlinear hyperbolic conservation laws.

Numerical experiments showed that the new method yields an efficiency gain of more than an order of magnitude in computational time. Adaptive gridding does not altogether eliminate the "magic number" feature, for which other approaches were criticized in the introductory chapter of this dissertation; however, the "magic number" here is the local-error tolerance ε. In principle, the local-error tolerance ε is proportional to the (global) error in the computed solution, but the relation is complex (as the numerical example shows) and not a by-product of the algorithm. Nonetheless I maintain that the simplicity and homogeneity of the algorithm, and

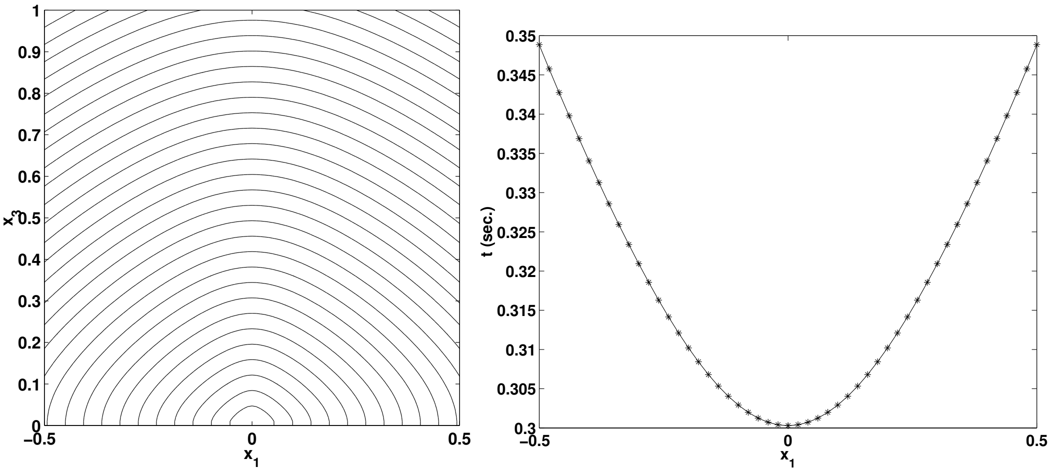

Figure 5.13 Left: traveltime contours for a 2-D VTI model by the adaptive-gridding approach: anisotropic effects on the wave propagation are evident. Right: traveltime comparison at $z = 1.0$ km for the model: adaptive-gridding traveltimes (*) and analytic traveltimes (-) match very well.

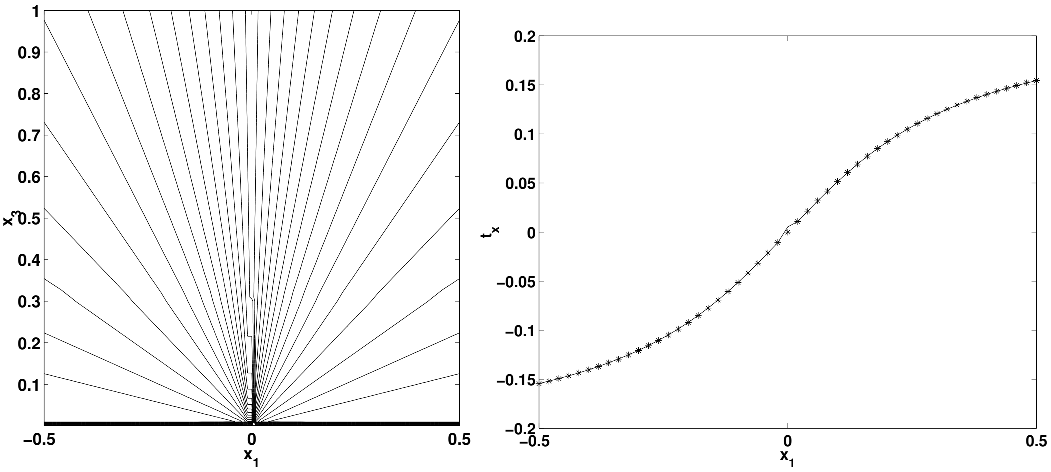

Figure 5.14 Left: contours of $\dfrac{\partial \tau}{\partial x}$ for a 2-D VTI model by the adaptive-gridding approach. Right: comparisons of $\dfrac{\partial \tau}{\partial x}$ at $z = 1.0$ km for the model: the adaptive-gridding solution (*) and analytic solution (-) match very well.

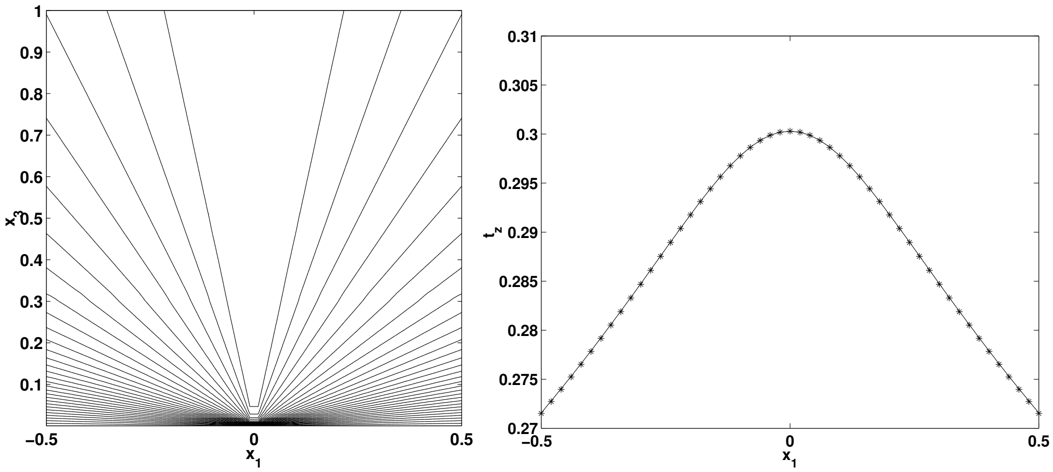

Figure 5.15 Left: contours of $\frac{\partial \tau}{\partial z}$ for a 2-D VTI model by the adaptive-gridding approach. Right: comparisons of $\frac{\partial \tau}{\partial z}$ at $z = 1.0$ km for the model: the adaptive-gridding solution (*) and analytic solution (-) match very well.

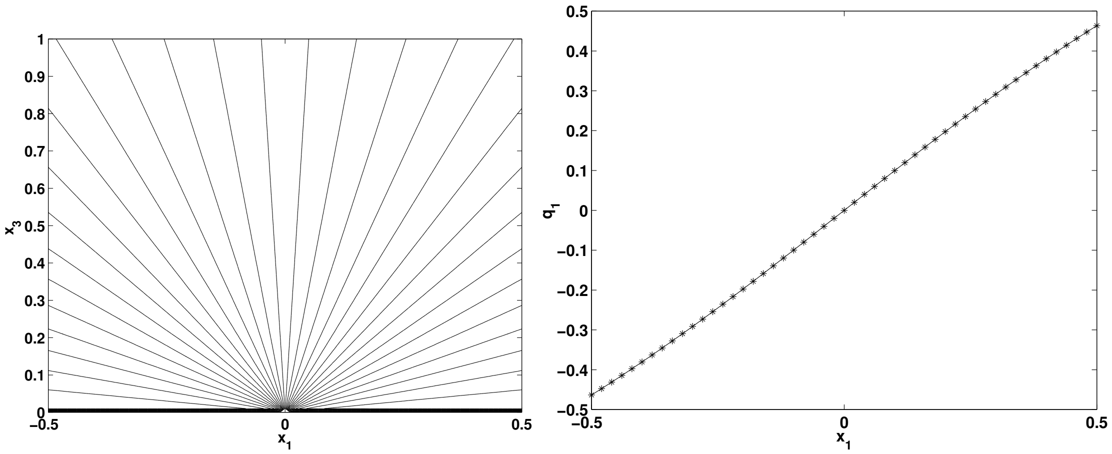

Figure 5.16 Left: take-off angles for a 2-D VTI model by the adaptive-gridding approach: the contours are straight along the ray. Right: take-off angle calibration at $z = 1.0$ km for the model: the adaptive-gridding solution (*) and analytic solution (-) match very well.

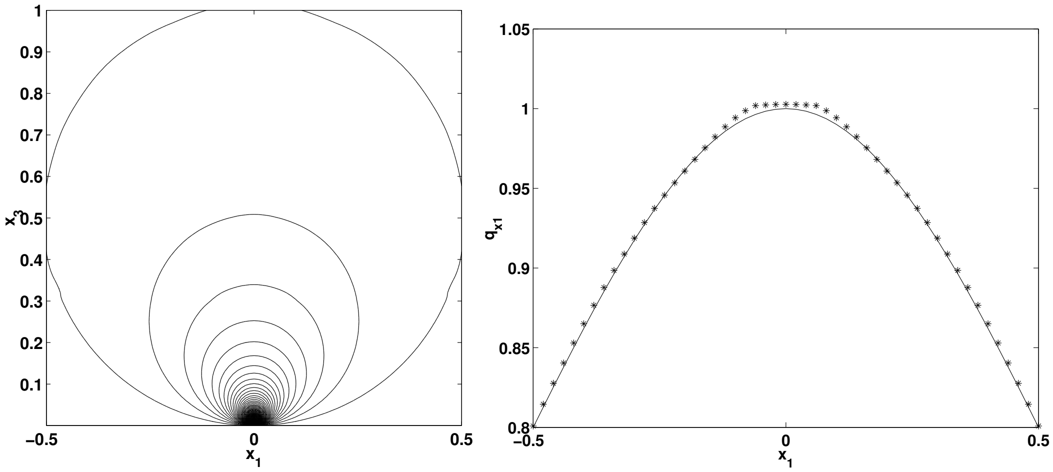

Figure 5.17 Left: contours of $\frac{\partial q_1}{\partial x}$ for a 2-D VTI model by the adaptive-gridding approach. Right: calibrations of $\frac{\partial q_1}{\partial x}$ at $z = 1.0$ km for the model. Since $q_1 = 0$ is a sonic point where the accuracy of numerical derivatives $\frac{\partial q_1}{\partial x}$ is poor, this inaccuracy is observed near the apex. Away from the sonic point, the adaptive-gridding solution (*) and analytic solution (-) match very well.

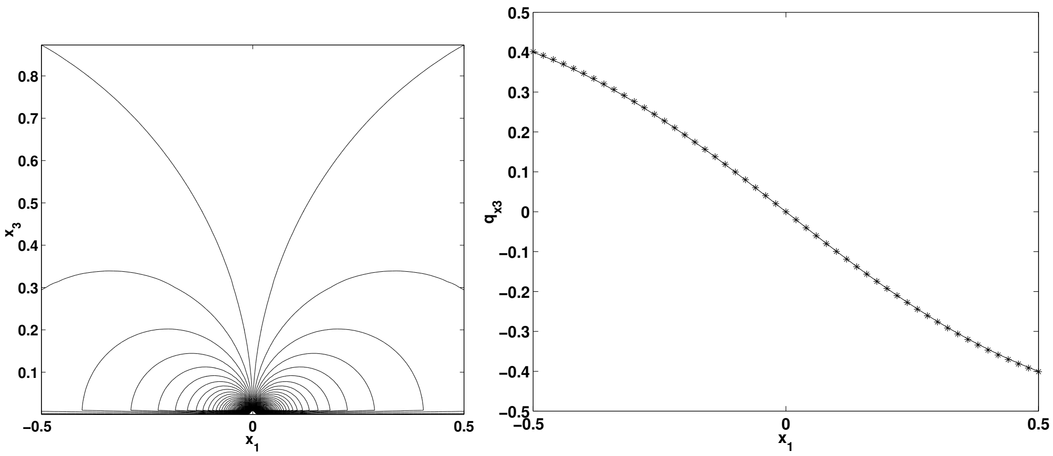

Figure 5.18 Left: contours of $\frac{\partial q_1}{\partial z}$ for a 2-D VTI model by the adaptive-gridding approach. Right: calibrations of $\frac{\partial q_1}{\partial z}$ at $z = 1.0$ km for the model: the adaptive-gridding solution (*) and analytic solution match very well.

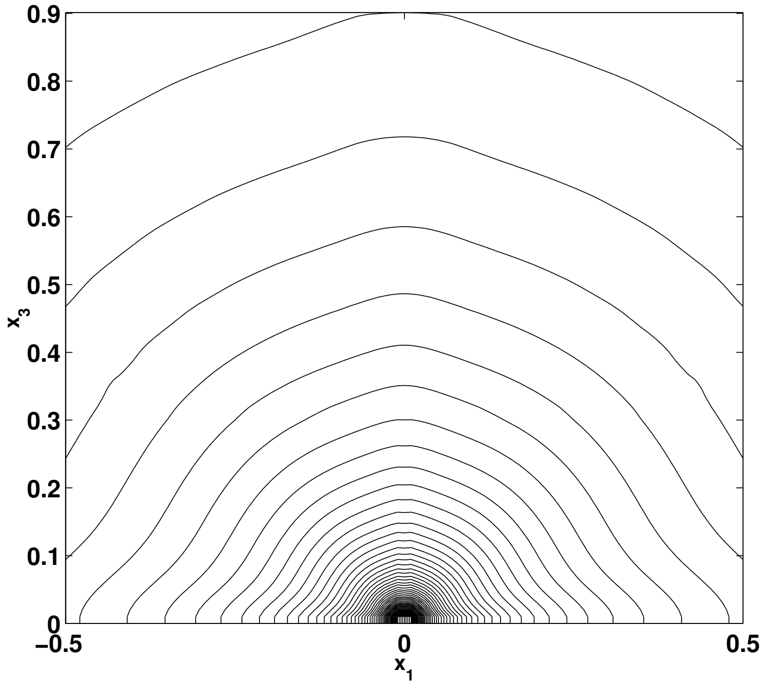

Figure 5.19 Amplitude contours for a 2-D VTI model by the adaptive-gridding WENO approach.

the direct if not apparent relation between ε and the global solution error, make the adaptive-gridding scheme easier to use than its alternatives. Also, the considerable success of the variable-step selection methods for ODEs (Gear [Gea71]), which have the same indirect error control feature, supports this contention.

At the outset of implementing the adaptive-gridding approach for amplitudes, I used a third-order ENO schemes for solving the eikonal equation, which led to an inaccurate amplitude field. The reason is that the third-order ENO scheme does not produce a smooth flux, though the Hamiltonian was smoothed to some degree. So I turned to WENO schemes, which yield the desired amplitude field.

Chapter 6

Conclusions

From the inception, the objective of this dissertation has been to use upwind finite-difference schemes to compute traveltimes and amplitudes in anisotropic solids, which are needed in constructing the geometrical optics term for anisotropic solids. Because of the theoretical work on the viscosity solution which is related to the first-arrival traveltime, the specific objective of this dissertation is to develop theories and numerical methods for constructing the geometrical optics term of quasi-P waves in general anisotropic solids.

To that end, the first chapter not only overviewed the geometrical optics and the asymptotic method for PDEs but also identified two difficulties associated with developing upwind finite-difference methods for traveltimes and amplitudes in anisotropic solids. The first difficulty is the lack of a built-in reliable indicator of the ray velocity direction, and the second one is the upwind singularity of the traveltime field at the source. To overcome the first difficulty, I proposed a paraxial eikonal equation which has a built-in reliable indicator of the ray velocity direction. To eliminate the second difficulty, I proposed an adaptive-gridding WENO approach.

Chapter 2 presented the theories of the geometrical optics for quasi-P waves in anisotropic solids. Section 2.1 applied the high frequency asymptotics to the linear elastic wave equations to derive the eikonal equation for traveltimes and the transport equation for amplitudes. With the eikonal equation in place, in section 2.2 I constructed the paraxial eikonal equation for the quasi-P wave traveltime by making use of the convexity of the slowness surface, which has a built-in reliable indicator of the ray velocity direction. In addition, the existence of the construction was proved in Appendix A. Based on the paraxial eikonal equation, the amplitude formula in Cartesian coordinates was derived from the one in ray coordinates (Section 2.3). To compute the auxiliary quantities needed in the amplitude formula, I derived two new advection equations for ray parameters (Section 2.3). The paraxial eikonal equation and the two new advection equations provide sound foundations for the following algorithm development.

The focus of Chapter 3 was developing the numerical methods of the geometrical optics for quasi-P waves in anisotropic solids. The centerpiece of the chapter was Section 3.1. In this section, I presented algorithms for computing the paraxial Hamiltonian needed in solving the paraxial eikonal equation, along with a new algorithm for initializing traveltimes in finite-difference schemes. Section 3.2 served as a tutorial and gave a new derivation of a first-order Godunov scheme by using a local paraxial ray-tracing technique. Based on the first-order Godunov scheme, Section 3.3 explored the construction of high-order ENO Runge-Kutta and WENO Runge-Kutta finite-difference schemes, which are used to solve the paraxial eikonal equation for traveltimes and the advection equation for take-off angles.

Chapter 4 applied the theories and numerical methods developed in Chapters 2 and 3 to solving the paraxial eikonal equation in transversely isotropic (TI) solids. To appreciate the construction of the paraxial eikonal equation, in Section 4.1 I simplified a paraxial Hamiltonian for TI solids with a vertical symmetry axis (VTI) by using the maximum phase angle condition. To obtain a general slowness surface, in Section 4.2 I built an inclined TI (ITI) model by rotating a VTI model. In Section 4.3, extensive numerical experiments were performed to verify the feasibility of the theory and the efficiency and accuracy of the numerical algorithms, including examples for 2-D VTI solids, 3-D VTI solids, and isotropic and anisotropic Marmousi models. Because of the generality of inclined TI solids, Section 4.4 consisting of numerical examples for ITI solids was specialized in illustrating the efficiency and accuracy of the algorithms developed in Chapter 3 for general anisotropic solids. The numerical examples demonstrated that the theories developed in Chapter 2 are feasible and the numerical algorithms described in Chapter 3 are accurate and efficient in capturing the anisotropic wave propagation.

In Chapter 5, the adaptive-gridding WENO approach was proposed to treat the upwind singularity at the point source and compute the amplitude function for both isotropic and anisotropic solids. It started with formulating the geometrical optics term for isotropic solids (Section 5.1), including the paraxial eikonal equation for traveltimes and the advection equation for take-off angles. Section 5.2 briefly mentioned the high-order WENO schemes for traveltimes and take-off angles, with details presented in Chapter 3 and Appendix C. In Section 5.3, I plunged into the details of the adaptive-gridding WENO approach for the upwind singularity at the source, including an algorithm framework. To illustrate the adaptive-gridding WENO approach, Section 5.4 presented some numerical experiments to show that the approach is efficient and accurate. In Section 5.5 and 5.6, the adaptive-gridding WENO approach was applied to computing the traveltime and amplitude in VTI solids, along with some examples showing that the approach works for anisotropic solids as well. The numerical examples showed that the adaptive-gridding WENO approach yields accurate amplitude fields for both isotropic and anisotropic solids.

The theoretical and numerical results from Chapter 2 to Chapter 5 illustrated that (i) the paraxial eikonal equation has a built-in reliable indicator of the quasi-P ray direction so that it can be used safely for extrapolating the traveltime field by using upwind finite difference schemes; (ii) the adaptive-gridding-WENO approach can treat efficiently the upwind singularity of the traveltime field at the source and can yield an accurate amplitude field as well. Hence, the theories and methods developed in this dissertation provide tools for constructing the geometrical optics term of the quasi-P wave in general anisotropic solids.

6.1 Contributions

The first contribution of this dissertation is the introduction and algorithmic development of paraxial eikonal equations for quasi-P waves. The second contribution is the use of adaptive-gridding WENO strategy in treating the upwind singularity at the point source when computing the amplitude field.

6.2 Future work

There are several directions which merit further investigation:

1. The central hypothesis of the dissertation is that the first-arrival traveltime in anisotropic solids is a viscosity solution of a nonlinear partial differential equation. It is necessary to verify this hypothesis by using the viscosity theory (Crandall and Lions [CL83] [CL84]).

2. The current research concerns only the computation of quasi-P traveltimes by finite-difference schemes. Because of cusps in the quasi-transverse (quasi-S) wave propagation, it is unclear how to compute the related traveltimes on Cartesian coordinates by finite-difference schemes, though there are some attempts in this direction; see Steinhoff et. al. [SFW00], Ruuth et. al. [RMO99].

3. The paraxial eikonal equation introduced in this dissertation produces only a limited aperture traveltime field along x_3-direction. A natural question to ask is how to generate a full aperture traveltime field. Notice that the methodology presented here can be used to formulate the paraxial eikonal equation in other

directions as well. Then based upon these paraxial formulations of eikonal equations and Fermat's principle, the down-and-out (DNO) technology, first introduced by Dellinger and Symes [DS97] and then extended by Kim and Cook [KC99], may be used to generate the full aperture traveltime field. This possibility is left as a future topic.

4. This dissertation is interested only in first-arrival traveltimes and related amplitudes. If one wants to capture caustics, the situation is totally different and the amplitude formula presented in the dissertation does not hold. Benamou and Solliec [BS99] have formulated an Eulerian method for capturing the caustics in isotropic solids; therefore, it is promising and challenging to capture caustics in anisotropic solids using an Eulerian method.

5. The purpose of constructing the geometrical optics term is providing tools for seismic imaging; hence it is natural to embed the anisotropic traveltime-amplitude solver in the Kirchhoff inversion/migration codes to see how it works in practice.

6. The 2-D version of the adaptive-gridding WENO traveltime-amplitude solver yields an efficiency gain of more than an order of magnitude in computational time. Because all the difference schemes presented in the dissertation are for the three-dimensional case, there is no difficulty in implementing a 3-D version of the adaptive-gridding traveltime-amplitude solver for both isotropic and anisotropic solids. Moreover, the efficiency gain in computational cost is expected to be even more dramatic in 3-D cases.

7. With the anisotropic traveltime-amplitude solver in hand, it is attractive to extend differential semblance optimization (DSO) for the velocity analysis in

isotropic media to the velocity analysis in anisotropic media (Symes [Sym90], Symes and Carazzone [SC91], Chauris and Noble [CN99]) in that the velocity of the medium is one of the ultimate goals in the seismic inversion.

Appendix A

Some Results from Convexity

Assuming that the slowness surface S is C^1, bounded, closed and strictly convex, I prove the following results.

Theorem A.1 For any given

$$(p_1^*, p_2^*) \in \{(p_1, p_2) : \exists p_3 \quad s.t. \quad S(p_1, p_2, p_3) = 0\}, \tag{A.1}$$

draw the straight line passing through (p_1^*, p_2^*) and parallel to p_3 axis in the (p_1, p_2, p_3) space, then there exist at most two intersection points (p_1^*, p_2^*, p_3^1) and (p_1^*, p_2^*, p_3^2). The outward normals at the two intersection points have p_3 components of opposite signs.

Proof: Consider 2-D case; 3-D similar. By strict convexity of the slowness surface, for p_1^* given, there are at most two intersection points. Without loss of generality, for p_1^* given, assume that there exist p_3^1 and p_3^2 such that $S(p_1^*, p_3^1) = S(p_1^*, p_3^2) = 0$, Figure 2.2.

Let $p_3^1 > p_3^2$. For $p_3 \in [p_3^2, p_3^1]$, define two functions

$$f(p_3) \quad = \quad \sup\{\alpha : S(\alpha, p_3) = 0, \alpha \geq p_1^*\}, \tag{A.2}$$

$$g(p_3) \quad = \quad \inf\{\alpha : S(\alpha, p_3) = 0, \alpha \leq p_1^*\}. \tag{A.3}$$

Both f and g are well defined and convex (or concave) by convexity of S, and one of them must satisfy that

$$f(p_3^1) \quad = \quad p_1^* = f(p_3^2) \tag{A.4}$$

or

$$g(p_3^1) \quad = \quad p_1^* = g(p_3^2). \tag{A.5}$$

Without loss of generality, suppose f satisfies the above constraint, then its graph corresponds to a section of slowness surface S.

By Rolle's mean theorem, there exists a $\xi \in (p_3^2, p_3^1)$ such that

$$\frac{df}{dp_3}(\xi) \quad = \quad 0. \tag{A.6}$$

However, $\dfrac{df}{dp_3}$ is strictly monotonic by strict convexity of f, so

$$\frac{df}{dp_3}(p_3^1)\frac{df}{dp_3}(p_3^2) \quad < \quad 0. \tag{A.7}$$

Assuming that $\dfrac{df}{dp_3}(p_3^1) < 0$ and $\dfrac{df}{dp_3}(p_3^2) > 0$, they define the tangents at those two points; see Figure 2.2. It follows that the outward normal at (p_1^*, p_3^1) has acute angle with positive p_3 direction, so it has positive p_3 component. Similarly, the outward normal at (p_1^*, p_3^2) has negative p_3 component.

By Theorem 1, the following function is well defined.

Definition A.1 For $(p_1, p_2) \in \{(p_1, p_2) : \exists p_3 \text{ s.t. } S(p_1, p_2, p_3) = 0\}$, define $p_3 = H(p_1, p_2)$ satisfying that

$$S(p_1, p_2, H(p_1, p_2)) = 0, \qquad \frac{\partial S}{\partial p_3}(p_1, p_2, H(p_1, p_2)) \geq 0. \tag{A.8}$$

Theorem A.2 2-D case. Suppose $\partial\Omega = \{(p_1, p_3) : S(p_1, p_3) = 0\}$ is a bounded closed set. Under the assumption of Theorem 1, the following two sets are both nonempty:

$$F \quad = \quad \{p_1^* : \exists p_3^1, p_3^2 \Rightarrow f(p_3^1) = p_1^* = f(p_3^2)\}, \tag{A.9}$$

$$G \;=\; \{p_1^* : \exists p_3^1, p_3^2 \Rightarrow g(p_3^1) = p_1^* = g(p_3^2)\}, \tag{A.10}$$

where p_1^* satisfies that there exist p_3^1 and p_3^2 such that

$$S(p_1^*, p_3^1) \;=\; S(p_1^*, p_3^2) = 0, \tag{A.11}$$

and f and g are defined in Theorem 1. Moreover, $\inf F \leq \sup G$.

Proof: Obviously, at least one of them is nonempty. Without loss of generality, let F be nonempty. Suppose G is empty, it means that all the $p_1 \in \{p_1 : \exists p_3$ s.t. $S(p_1, p_3) = 0\}$ is in F. Because F is a closed bounded set, $\beta = \inf F > -\infty$. For $p_1^* = \beta$, $\exists$ p_3^1 and p_3^2 such that $\dfrac{df}{dp_3}$ is strictly monotonic in $[p_3^2, p_3^1]$, hence S can not be closed, which is a contradiction; it follows that G is nonempty. Moreover, if $\inf F > \sup G$, S consists of two branches which are not connected; therefore, it cannot be a closed convex set. It follows that $\inf F \leq \sup G$.

Theorem A.3 2-D case. Under the assumption of Theorem 1 and Theorem 2, among all (p_1, p_3) such that

$$S(p_1, p_3) = 0, \qquad \frac{\partial S}{\partial p_3}(p_1, p_3) \geq 0, \tag{A.12}$$

there are $p_1^{\min}$, $p_1^{\max}$ such that

$$S(p_1^{\min}, H(p_1^{\min})) = 0, \qquad \frac{1}{|\nabla S|}\frac{\partial S}{\partial p_3}(p_1^{\min}, H(p_1^{\min})) = 0, \tag{A.13}$$

$$S(p_1^{\max}, H(p_1^{\max})) = 0, \qquad \frac{1}{|\nabla S|}\frac{\partial S}{\partial p_3}(p_1^{\max}, H(p_1^{\max})) = 0. \tag{A.14}$$

For $0 < \Delta < 1$ and $p_1 \in [(1-\Delta)p_1^{\min}, (1-\Delta)p_1^{\max}]$,

$$\frac{1}{|\nabla S|}\frac{\partial S}{\partial p_3}(p_1, H(p_1)) \;\geq\; O(\Delta) > 0. \tag{A.15}$$

Proof: By Theorem 1 and $F \neq \emptyset$, for $\forall p_1^* \in F$, $\exists f$ such that $\frac{df}{dp_3} \leq 0$ and $\frac{df}{dp_3}$ is strictly decreasing in $[\xi, p_3^1]$, where $\frac{df}{dp_3}(\xi) = 0$. Define $p_1^{\max} = f(\xi)$, then $\xi = H(p_1^{\max})$, so (A.14) holds. By strict monotonicity of function f in $[\xi, p_3^1]$, for $p_1 = (1-\Delta)p_1^{\max}$, there exists $\eta \in (\xi, p_3^1)$ such that

$$f(\eta) = (1-\Delta)p_1^{\max} \quad , \quad \sigma = \frac{df}{dp_3}(\eta) < 0. \tag{A.16}$$

Then the outward normal at $(f(\eta), \eta)$ is $(\frac{1}{\sqrt{1+\sigma^2}}, \frac{|\sigma|}{\sqrt{1+\sigma^2}})$. Because $\frac{df}{dp_3}$ is strictly decreasing, $\frac{df}{dp_3}(p_3) \leq \frac{df}{dp_3}(\eta) < 0$ if $p_3 \geq \eta$. Furthermore, for $p_1 \in F$ and $p_1 \leq (1-\Delta)p_1^{\max}$,

$$\frac{1}{|\nabla S(p_1, H(p_1))|}\frac{\partial S}{\partial p_3}(p_1, H(p_1)) \quad \geq \quad O(\Delta) > 0. \tag{A.17}$$

Similarly, by $G \neq \emptyset$, there exists $p_1^{\min}$ such that (A.13) holds. Also, for $p_1 \in G$, $p_1 \geq (1-\Delta)p_1^{\min}$,

$$\frac{1}{|\nabla S(p_1, H(p_1))|}\frac{\partial S}{\partial p_3}(p_1, H(p_1)) \quad \geq \quad O(\Delta) > 0. \tag{A.18}$$

Finally, by $\inf F \leq \sup G$, for $p_1 \in [(1-\Delta)p_1^{\min}, (1-\Delta)p_1^{\max}]$ we have

$$\frac{1}{|\nabla S(p_1, H(p_1))|}\frac{\partial S}{\partial p_3}(p_1, H(p_1)) \quad \geq \quad O(\Delta) > 0. \tag{A.19}$$

Definition A.2 2-D Hamiltonian H_Δ. Given $\Delta > 0$, $p_1^{\min}$, $p_1^{\max}$ defined as in Theorem 3, for $\forall p_1 \in R^1$, define function H_Δ:

$$H_\Delta(p_1) = \begin{cases} H(p_1) & \text{if } p_1 \in [(1-\Delta)p_1^{\min}, (1-\Delta)p_1^{\max}], \\ H\left((1-\Delta)p_1^{\min}\right) & \text{else if } p_1 < (1-\Delta)p_1^{\min}, \\ H((1-\Delta)p_1^{\max}) & \text{else if } p_1 > (1-\Delta)p_1^{\max}. \end{cases} \tag{A.20}$$

Theorem A.4 Suppose S is C^2. The Hamiltonian H_Δ is concave, C^2 in the interval $((1-\Delta)p_1^{\min}, (1-\Delta)p_1^{\max})$ and C^0 in R.

Proof: Only need to consider H_Δ in the interval $((1-\Delta)p_1^{\min},(1-\Delta)p_1^{\max})$. By

$$S(p_1,p_3) \;=\; S(p_1,H(p_1))=0, \tag{A.21}$$

take the derivative twice with respect to p_1 in the above,

$$\begin{pmatrix} 1 \\ \frac{\partial H}{\partial p_1} \end{pmatrix}^T \begin{pmatrix} \frac{\partial^2 S}{\partial p_1 \partial p_1} & \frac{\partial^2 S}{\partial p_1 \partial p_3} \\ \frac{\partial^2 S}{\partial p_1 \partial p_3} & \frac{\partial^2 S}{\partial p_3 \partial p_3} \end{pmatrix} \begin{pmatrix} 1 \\ \frac{\partial H}{\partial p_1} \end{pmatrix} + \frac{\partial S}{\partial p_3}\frac{\partial^2 H}{\partial p_1 \partial p_1} \;=\; 0. \tag{A.22}$$

The Hessian matrix in the above is positive definite by S strictly convex and $\frac{\partial S}{\partial p_3} > 0$, so we have $\frac{\partial^2 H}{\partial p_1 \partial p_1} < 0$. It follows that H is concave in $((1-\Delta)p_1^{\min},(1-\Delta)p_1^{\max})$. H_Δ is constant outside $((1-\Delta)p_1^{\min},(1-\Delta)p_1^{\max})$, so it is concave.

Theorem A.5 3-D case. Given $\Delta > 0$, for any radial plane $p_2 = kp_1$ cutting through slowness surface S, two intersection points $(p_1^{\min}, kp_1^{\min}) = (p_1^{\min}(k), kp_1^{\min}(k))$ and $(p_1^{\max}, kp_1^{\max}) = (p_1^{\max}(k), kp_1^{\max}(k))$ exist such that

$$S(p_1^{\min}, kp_1^{\min}, H(p_1^{\min}, kp_1^{\min})) \;=\; 0, \tag{A.23}$$

$$\frac{1}{|\nabla S|}\frac{\partial S}{\partial p_3}(p_1^{\min}, kp_1^{\min}, H(p_1^{\min}, kp_1^{\min})) \;=\; 0, \tag{A.24}$$

$$S(p_1^{\max}, kp_1^{\max}, H(p_1^{\max}, kp_1^{\max})) \;=\; 0, \tag{A.25}$$

$$\frac{1}{|\nabla S|}\frac{\partial S}{\partial p_3}(p_1^{\max}, kp_1^{\max}, H(p_1^{\max}, kp_1^{\max})) \;=\; 0. \tag{A.26}$$

For $p_1 \in [(1-\Delta)p_1^{\min}(k),(1-\Delta)p_1^{\max}(k)]$ and $p_2 = kp_1$,

$$\frac{1}{|\nabla S|}\frac{\partial S}{\partial p_3}(p_1,p_2,H(p_1,p_2)) \;\geq\; O(\Delta) > 0. \tag{A.27}$$

Proof: When $k = 0$ or $k = \infty$, the Theorem reduces to the 2D case, which is proved in Theorem 3. Otherwise we can rotate the axes of the coordinates by orthogonal transformation

$$M = \begin{pmatrix} \frac{1}{\sqrt{1+k^2}} & \frac{k}{\sqrt{1+k^2}} & 0 \\ -\frac{k}{\sqrt{1+k^2}} & \frac{1}{\sqrt{1+k^2}} & 0 \\ 0 & 0 & 1 \end{pmatrix} \tag{A.28}$$

such that the new $op_1^{'}$ lies in the plane $p_2 = kp_1$ and $op_2^{'}$ is perpendicular to it. Thus we have reduced the 3-D problem to a 2-D problem in $op_1^{'}p_3$ coordinate plane. By Theorem 3, there exists $p_1^{'\min}$ and $p_1^{'\max}$ such that

$$S'(p_1^{'\min}, H'(p_1^{'\min})) = 0, \qquad \frac{1}{|\nabla S'|}\frac{\partial S'}{\partial p_3}(p_1^{'\min}, H'(p_1^{'\min})) = 0, \tag{A.29}$$

$$S'(p_1^{'\max}, H'(p_1^{'\max})) = 0, \qquad \frac{1}{|\nabla S'|}\frac{\partial S'}{\partial p_3}(p_1^{'\max}, H'(p_1^{'\max})) = 0, \tag{A.30}$$

where $S^{'}$ and $H^{'}$ are intersections of the slowness surface S and Hamiltonian H with $op_1'p_3$ plane (or radial plane $p_2 = kp_1$), respectively.

Performing the inverse transform to pull the above result back to original coordinates, we have an interval $[p_1^{\min}, p_1^{\max}]$, where $p_1^{\min} = \frac{1}{\sqrt{1+k^2}}p_1^{'\min}$ and $p_1^{\max} = \frac{1}{\sqrt{1+k^2}}p_1^{'\max}$, such that for $p_2 = kp_1$ Theorem 5 holds.

It is convenient to parameterize the horizontal plane (p_1, p_2) by polar coordinates

$$(p_1, p_2) = (p\cos\phi, p\sin\phi), \tag{A.31}$$

and I can summarize Theorem 5 into a Corollary.

Corollary A.1 For each planar angle ϕ, the family of planes with outwrad normal $(\cos\phi, \sin\phi, 0)$ is tangent to the slowness surface at the point

$$\mathbf{p} = (p_{\max}(\phi)\cos\phi, p_{\max}(\phi)\sin\phi, p_3(\phi)), \tag{A.32}$$

which is unique and satisfies

$$S(p_{\max}(\phi)\cos\phi, p_{\max}(\phi)\sin\phi, p_3(\phi)) \quad = \quad 0, \tag{A.33}$$

$$\frac{1}{|\nabla S|}\frac{\partial S}{\partial p_3}(p_{\max}(\phi)\cos\phi, p_{\max}(\phi)\sin\phi, p_3(\phi)) \quad = \quad 0. \tag{A.34}$$

For $0 < \Delta < 1$, $p \leq (1-\Delta)p_{\max}(\phi)$ and $(p_1, p_2) = (p\cos\phi, p\sin\phi)$, we have

$$\frac{1}{|\nabla S|}\frac{\partial S}{\partial p_3}(p_1, p_2, H(p_1, p_2)) \quad \geq \quad O(\Delta) > 0. \tag{A.35}$$

Proof: The uniqueness follows from the strict convexity of the slowness surface.

Remark: By the method of characteristics, we can see that Theorem 5 just puts a positive lower bound for the third component of the normalized ray direction; namely, the group angle of the ray with the vertical axis never goes near 90 degrees.

Definition A.3 Three-dimensional Hamiltonian H_Δ. Given $\Delta > 0$, for any

$$(p_1, p_2) \quad = \quad (p\cos\phi, p\sin\phi),$$

there exists $p_{\max}(\phi)$ as in Corollary 1; define function H_Δ:

$$H_\Delta\left(p_1, p_2\right) = \begin{cases} H\left(p_1, p_2\right), \text{ if } p \leq (1-\Delta)p_{\max}(\phi); \\ H\left((1-\Delta)p_{\max}(\phi)\cos\phi, (1-\Delta)p_{\max}(\phi)\sin\phi\right), \text{ else.} \end{cases} \tag{A.36}$$

Corollary A.2 Under the assumption of Corollary 1, the inequality

$$\sqrt{\left(\frac{\partial H_\Delta}{\partial p_1}\right)^2 + \left(\frac{\partial H_\Delta}{\partial p_2}\right)^2} \quad \leq \quad O(\frac{1}{\Delta}) \tag{A.37}$$

holds.

Proof: By using ray equations (2.16), (2.19) and (2.20), we have

$$\frac{\partial S}{\partial p_1} = -\frac{\frac{\partial H}{\partial p_1}}{H - p_1\frac{\partial H}{\partial p_1} - p_2\frac{\partial H}{\partial p_2}}, \tag{A.38}$$

$$\frac{\partial S}{\partial p_2} = -\frac{\frac{\partial H}{\partial p_2}}{H - p_1\frac{\partial H}{\partial p_1} - p_2\frac{\partial H}{\partial p_2}}, \tag{A.39}$$

$$\frac{\partial S}{\partial p_3} = \frac{1}{H - p_1\frac{\partial H}{\partial p_1} - p_2\frac{\partial H}{\partial p_2}}. \tag{A.40}$$

The inequality follows by using Corollary 1.

Appendix B

Initialization of Traveltimes in VTI

Assuming that the VTI medium is homogeneous, I only need to consider the 2-D case because of the transverse isotropy with respect to the vertical symmetry axis. Given source point (x_1^s, x_3^s) and target point (x_1^o, x_3^o), I will try to find the traveltime between these two points. Suppose $x_1^o - x_1^s > 0$ and $x_3^o - x_3^s > 0$, then the group angle ϕ at (x_1^o, x_3^o) satisfies that $\tan\phi = \dfrac{x_3^o - x_3^s}{x_1^o - x_1^s}$ and $\phi = \phi(\theta)$ where θ is the phase angle at (x_1^o, x_3^o). I can find the phase angle by a bisection iterative method just like Algorithm 3.5 in Chapter 3, and then I can compute the group velocity from the raytracing equation. Finally the traveltime follows from the group velocity. The following algorithm is a simplified version of Algorithm 3.5.

- Input: (x_1^s, x_3^s), (x_1^o, x_3^o) and $\alpha_0, \beta_0, \epsilon, \delta$.
- Set $x_1 = x_1^o - x_1^s$, $x_3 = x_3^o - x_3^s$, $\vec{n}_1 = (1, 0)^T$, $\vec{n}_2 = (0, 1)^T$;
- Compute $\vec{n} = \frac{1}{2}(\vec{n}_1 + \vec{n}_2)$; $\vec{n} = \dfrac{\vec{n}}{|\vec{n}|}$.
- do
  - Compute $(v_g^1, v_g^3)^T = \vec{F}(\vec{n}, \alpha_0, \beta_0, \epsilon, \delta)$.
  - if $\dfrac{v_g^3}{v_g^1} \geq \dfrac{x_3}{x_1}$, $\vec{n}_2 = \vec{n}$; else $\vec{n}_1 = \vec{n}$;
  - Compute $\vec{n} = \frac{1}{2}(\vec{n}_1 + \vec{n}_2)$; $\vec{n} = \dfrac{\vec{n}}{|\vec{n}|}$.
- until $(n_1(2) \geq n(2)$ or $n(2) \geq n_2(2))$
- Compute traveltime $t = \dfrac{\sqrt{x_1^2 + x_3^2}}{\sqrt{(v_g^1)^2 + (v_g^3)^2}}$.

In the above algorithm, I use the raytracing equation ($\vec{F}$ denotes the righthand side):

$$v_g^1 = p_1(2\alpha_0^2(1+2\epsilon)\beta_0^2 p_1^2 + Ap_3^2 - \alpha_0^2(1+2\epsilon) - \beta_0^2)/D, \tag{B.1}$$

$$v_g^3 = p_3(2\alpha_0^2\beta_0^2 p_3^2 + Ap_1^2 - \alpha_0^2 - \beta_0^2)/D, \tag{B.2}$$

with

$$A = 2\alpha_0^2(\alpha_0^2(\epsilon-\delta) + \beta_0^2(1+\delta)), \tag{B.3}$$

$$D = 2 - (\alpha_0^2(1+\epsilon) + \beta_0^2)p_1^2 - (\alpha_0^2 + \beta_0^2)p_3^2; \tag{B.4}$$

p_1, p_3 can be computed from the phase velocity and phase normal $\vec{n}$.

Appendix C

WENO Schemes for Advection Equations

Recall the advection equation for the takeoff angle,

$$\frac{\partial \tau}{\partial x}\frac{\partial \phi}{\partial x} + \frac{\partial \tau}{\partial z}\frac{\partial \phi}{\partial z} \quad = \quad 0. \tag{C.1}$$

To match with the evolution form of the eikonal equation in depth, I formulate the advection equation as an evolution equation in depth as well, i.e.,

$$\frac{\partial \phi}{\partial z} \quad = \quad -\left(\frac{\partial \tau}{\partial z}\right)^{-1}\frac{\partial \tau}{\partial x}\frac{\partial \phi}{\partial x}. \tag{C.2}$$

To fully take advantage of the accuracy of traveltimes produced by the WENO Runge-Kutta third-order scheme for the eikonal equation and simplify the implementation, I embed the third-order scheme for equation (C.2) into the third-order scheme for the eikonal equation.

At first, introduce the approximations for x-derivative and z-derivative of τ in the above advection equation:

$$\frac{\partial \tau}{\partial x} \approx D_x[\tau] \quad = \quad \max(D_x^{-\mathrm{W},3}\tau, 0) + \min(D_x^{+\mathrm{W},3}\tau, 0), \tag{C.3}$$

$$\frac{\partial \tau}{\partial z} \quad \approx \quad H(\widehat{D}_x^3\tau). \tag{C.4}$$

Next, define the upwind difference approximation for $\frac{\partial \phi}{\partial x}$. Because the choice of stencil in ENO schemes is too sensitive to the zeros of solution (Liu et. al. [LOC94], Jiang and Shu [JS96], I use WENO schemes to approximate the derivative $\frac{\partial \phi}{\partial x}$.

Because the coefficient of the discretized advection equation has only second-order accuracy, which is computed from the eikonal equation by a third-order WENO scheme, I use a second-order WENO scheme to approximate the derivatives $\dfrac{\partial\phi}{\partial x}$. The second-order WENO scheme is based on the second-order ENO stencils, so it does not give rise to any new complexities in the coding. See Chapter 3 for details.

The second-order WENO schemes for $\dfrac{\partial\phi}{\partial x}$ are (Jiang and Peng [JP97]):

$$
\begin{aligned}
(\frac{\partial\phi}{\partial x})_i^k \approx (D_x^{-\mathrm{W},2}\phi)_i^k &= \frac{1}{2}(D_x^+\phi_{i-1}^k + D_x^+\phi_i^k) - \frac{w_-}{2}(D_x^+\phi_{i-2}^k - 2D_x^+\phi_{i-1}^k + D_x^+\phi_i^k)\\
(\frac{\partial\phi}{\partial x})_i^k \approx (D_x^{+\mathrm{W},2}\phi)_i^k &= \frac{1}{2}(D_x^+\phi_{i-1}^k + D_x^+\phi_i^k) - \frac{w_+}{2}(D_x^+\phi_{i+1}^k - 2D_x^+\phi_i^k + D_x^+\phi_{i-1}^k)
\end{aligned}
$$

where

$$
\begin{aligned}
w_- &= \frac{1}{1+2r_-^2}, \qquad r_- = \frac{\delta + (D_x^- D_x^- \phi_i^k)^2}{\delta + (D_x^- D_x^+ \phi_i^k)^2},\\
w_+ &= \frac{1}{1+2r_+^2}, \qquad r_+ = \frac{\delta + (D_x^+ D_x^+ \phi_i^k)^2}{\delta + (D_x^- D_x^+ \phi_i^k)^2}
\end{aligned}
$$

and δ is a small positive constant to avoid the denominators from becoming zero.

Now I define the upwind WENO difference for $\dfrac{\partial\phi}{\partial x}$ which corresponds to the upwind direction of $\dfrac{\partial\tau}{\partial x}$ as follows:

$$
D_x^{\mathrm{up}}\phi_i^k = \begin{cases} D_x^{-\mathrm{W},2}\phi_i^k & \text{if } D_x[\tau]_i^k \geq 0,\\ D_x^{+\mathrm{W},2}\phi_i^k & \text{else.}\end{cases} \tag{C.5}
$$

Finally, I can formulate the third-order WENO Runge-Kutta scheme for the advection equation as

$$
\begin{aligned}
\delta_3^1\phi &= \Delta z\Psi(\widehat{D}_x^3\tau, \phi),\\
\delta_3^2\phi &= \frac{1}{4}\left(\delta_3^1\phi + \Delta z\Psi(\widehat{D}_x^3(\tau + \delta_3^1\tau), \phi + \delta_3^1\phi)\right),\\
\delta_3^3\phi &= \frac{1}{3}\left(2\delta_3^2\phi + 2\Delta z\Psi(\widehat{D}_x^3(\tau + \delta_3^2\tau), \phi + \delta_3^2\phi)\right),
\end{aligned} \tag{C.6}
$$

where

$$
\Psi(\tau,\phi) = -\frac{D_x[\tau]D_x^{up}\phi}{H(\widehat{D}_x^3(\tau))}. \tag{C.7}
$$

The third-order scheme for ϕ is then

$$\phi^{k+1} \quad = \quad \phi^k + \delta_3^3 \phi^k \tag{C.8}$$

for $k = 0, 1, 2, \cdots$. But this scheme is really a second-order scheme, because the coefficients have only second-order accuracy.

With a few changes, the above scheme can be modified to solve the advection equation for τ_{yy}, the out-of-plane curvature.

Appendix D

Estimate the Initial Step

To initialize the traveltime for finite-difference schemes, I assumed that the velocity near the source is constant and equal to the source velocity. Now I desire to analyse the traveltime error caused by this assumption and furthermore compute an *a priori* estimate of the initial step.

Assuming that the source is at origin, consider the two-dimensional ray-tracing equation. By the method of characteristics, I have

$$\dot{x} = v^2 p, \tag{D.1}$$

$$\dot{z} = v^2 q, \tag{D.2}$$

$$\dot{p} = -\frac{1}{v}\frac{\partial v}{\partial x}, \tag{D.3}$$

$$\dot{q} = -\frac{1}{v}\frac{\partial v}{\partial z}, \tag{D.4}$$

where the dot $\cdot$ denotes the differentiation with respect to time t along the ray; $p = \dfrac{\partial \tau}{\partial x}$ and $q = \dfrac{\partial \tau}{\partial z}$.

Denote the group angle as θ, then we have

$$\dot{x} = v \sin\theta, \tag{D.5}$$

$$\dot{z} = v \cos\theta; \tag{D.6}$$

furthermore, equations (D.1) and (D.2) yield

$$p = \frac{\sin\theta}{v(x,z)}, \tag{D.7}$$

$$q = \frac{\cos\theta}{v(x,z)}. \tag{D.8}$$

Differentiate equation (D.7) with respect to time t and simplify the resultant equation, then I have

$$\dot{\theta} = -\cos\theta\frac{\partial v}{\partial x} + \sin\theta\frac{\partial v}{\partial z}. \tag{D.9}$$

Now I introduce polar coordinates, i.e.,

$$x = r\sin\psi, \tag{D.10}$$

$$z = r\cos\psi. \tag{D.11}$$

Differentiating equations (D.10) and (D.11) with respect to time t and solving for $\dot{r}$ and $\dot{\psi}$, I have

$$\dot{r} = v\cos(\theta-\psi), \tag{D.12}$$

$$\dot{\psi} = \frac{v}{r}\sin(\theta-\psi). \tag{D.13}$$

Next I want to estimate $(\theta-\psi)$. First of all, I have $|\theta-\psi| < \pi$, since for the downward wave propagation both θ and ψ lie in the interval $(-\frac{\pi}{2}, \frac{\pi}{2})$. Define

$$a(t) = \dot{\theta}, \tag{D.14}$$

$$b(t) = \frac{vt}{r}\frac{\sin(\theta-\psi)}{(\theta-\psi)}, \tag{D.15}$$

then by (D.9) and (D.13) I have an ordinary differential equation for $(\theta-\psi)$,

$$\dot{\theta}-\dot{\psi} = a(t) - \frac{b(t)}{t}(\theta-\psi); \tag{D.16}$$

its solution is

$$\theta-\psi = \int_0^t d\tau a(\tau)\exp\left(-\int_\tau^t d\sigma\frac{b(\sigma)}{\sigma}\right). \tag{D.17}$$

Because $b(t) \geq 0$ and the function a is bounded by $a_{\max}$, which is equal to the supremum of the length of gradient of the velocity, i.e., $|a| \leq a_{\max}$, equation (D.17) yields an estimate for $\theta-\psi$,

$$|\theta-\psi| \leq a_{\max}t. \tag{D.18}$$

Now I can get an approximate relative error estimate for the traveltime. Denote t_0 as the approximation to the exact traveltime t when using the constant velocity v_0 at the source as the approximation to the exact velocity v. Since

$$\dot{t_0} = \frac{\dot{r}}{v_0} \quad = \quad \frac{v}{v_0} \cos{(\theta - \psi)}, \tag{D.19}$$

we have

$$\dot{t_0} - \dot{t} \quad = \quad (\frac{v}{v_0} - 1) \cos{(\theta - \psi)} + \cos{(\theta - \psi)} - 1; \tag{D.20}$$

furthermore,

$$|\dot{t_0} - \dot{t}| \quad \leq \quad \left| \frac{v}{v_0} - 1 \right| + |\cos{(\theta - \psi)} - 1|. \tag{D.21}$$

Noticing that if $|\dot{t_0} - \dot{t}| \leq \varepsilon$, then $|t_0 - t| \leq \varepsilon t$. So let's specify that

$$\left| \frac{v}{v_0} - 1 \right| \quad \leq \quad \frac{\varepsilon}{2} \tag{D.22}$$

and

$$|\cos(\theta - \psi) - 1| \quad \leq \quad \frac{\varepsilon}{2}. \tag{D.23}$$

Expanding v at the origin (the source) by Taylor theorem with remainder, I have

$$v(x, z) \quad = \quad v_0 + \frac{\partial v}{\partial x}(\zeta_1, \eta_1)x + \frac{\partial v}{\partial z}(\zeta_2, \eta_2)z, \tag{D.24}$$

where (ζ_1, η_1) and (ζ_2, η_2) lie in

$$D \quad = \quad \{(\zeta, \eta) : \min(x, 0) \leq \zeta \leq \max(x, 0), 0 \leq \eta \leq z\}. \tag{D.25}$$

Consequently,

$$|v(x, z) - v_0| \leq \sqrt{2} r \sup\{|\nabla v(\zeta, \eta)| : |\zeta| \leq |x|, 0 \leq \eta \leq z\} \tag{D.26}$$

by Cauchy inequality.

Because I am only bounding the error inside the aperture,

$$|x| \le z \tan\theta_{\max}, \qquad r \le \frac{z}{\cos\theta_{\max}}; \tag{D.27}$$

it follows that

$$\begin{aligned} \left|\frac{v - v_0}{v_0}\right| &\le \frac{\sqrt{2}r}{v_0}\sup\{|\nabla v(\zeta,\eta)| : |\zeta| \le z\tan\theta_{\max}, 0 \le \eta \le z\} \\ &\le \frac{\sqrt{2}r}{v_0}\sup\{|\nabla v(\zeta,\eta)| : |\zeta| \le z_{\max}\tan\theta_{\max}, 0 \le \eta \le z_{\max}\} \\ &\le \frac{\sqrt{2}zB}{v_0\cos\theta_{\max}}, \end{aligned} \tag{D.28}$$

where $z_{\max}$ is the maximum depth and

$$B = \sup\{|\nabla v(\zeta,\eta)| : |\zeta| \le z_{\max}\tan\theta_{\max}, 0 \le \eta \le z_{\max}\}. \tag{D.29}$$

For (D.22) to hold, by (D.28) z should be chosen such that

$$z \le z_1 = \frac{v_0\varepsilon\cos\theta_{\max}}{2\sqrt{2}B}. \tag{D.30}$$

Finally I choose z so that (D.23) holds, and a lemma is needed to do so.

Lemma 1 Along a ray segment $\{(x(\tau), z(\tau)) : 0 \le \tau \le t\}$, the following inequality holds:

$$t \le \frac{r}{v_{\min}}, \tag{D.31}$$

where $r = \sqrt{x^2(t) + z^2(t)}$; $v_{\min}$ is the minimum velocity along the ray segment.

Proof: Denote the true ray path as s and its length $|s|$, and the straight ray path as l and its length $|l|$ which is equal to r. In addition, l is used to approximate the true ray path s. Then by Fermat's principle, I have

$$t = \int_s d\sigma\frac{1}{v} \le \int_l d\sigma\frac{1}{v} \le \int_l d\sigma\frac{1}{v_{\min}} = \frac{r}{v_{\min}}. \tag{D.32}$$

Using (D.18) and Lemma 1, I have

$$\begin{aligned} |\cos(\theta-\psi)-1| &= \left|-2\sin^2\frac{(\theta-\psi)}{2}\right| \\ &\leq \frac{(\theta-\psi)^2}{2} \\ &\leq \frac{r^2 a_{\max}^2}{v_{\min}^2} \\ &\leq \frac{r^2 B^2}{v_{\min}^2}, \end{aligned}$$

where I have used the relation $a_{\max} \leq B$ inside the aperture. Hence to make (D.23) hold implys that

$$z \leq z_2 = \sqrt{\frac{\varepsilon}{2}}\frac{v_{\min}\cos\theta_{\max}}{B}. \tag{D.33}$$

So for error tolerance ε, z_{init} should be chosen such that

$$z_{\text{init}} = \min(z_1, z_2). \tag{D.34}$$

Although both z_1 and z_2 depend on B (the bound of gradient of velocity model), there are at least two ways to estimate B. One way is simply setting B to be a big number which is larger than the actual value; the other way is computing the gradient of velocity model from the given discretized model. Both ways will produce a reasonable initial step.

Bibliography

[Alk97] T. Alkhalifah. Anisotropic Marmousi data set. In *SEP95*. Stanford University. (http://sepwww.stanford.edu/sep/tariq/), 1997.

[And96] J. E. Anderson. *Imaging in transversely isotropic media with a vertical symmetry axis*. PhD thesis, Center for Wave Phenomena, Colorado School of Mines, Golden, CO80401-1887, 1996.

[BB90] G. Beylkin and R. Burridge. Linearized inverse scattering problem of acoustics and elasticity. *Wave Motion*, 12:15–22, 1990.

[BdHMS98] R. Burridge, M.V. de Hoop, D. Miller, and C. Spencer. Multiparameter inversion in anisotropic media. *Geophys. J. Int.*, 134:757–777, 1998.

[Ber79] J. G. Berryman. Long-wave elastic anisotropy in transversely isotropic media. *Geophysics*, 44:896–917, 1979.

[Bey85] G. Beylkin. Imaging of discontinuities in the inverse scattering problem by inversion of a causal generalized radon transform. *J. Math. Phys.*, 26:99–108, 1985.

[BL97] M. Berger and R. J. LeVeque. Adaptive mesh refinement using wave-propagation algorithms for hyperbolic systems. In *Preprint*. Courant Institute, 1997.

[BO84] M. Berger and J. Oliger. Adaptive mesh refinement for hyperbolic partial differential equations. *J. Comput. Phys.*, 53:484–512, 1984.

[BS98] C. Belfi and W. W. Symes. An adaptive ENO algorithm for the eikonal equation. In *Annual Report, The Rice Inversion Project. (http://www.trip.caam.rice.edu/)*. Rice University, 1998.

[BS99] J. Benamou and I. Solliec. A Eulerian method for capturing caustics. In *Preprint, INRIA*. 1999.

[BW64] M. Born and E. Wolf. *Principles of optics*. The Macmillan Company, 1964.

[Cer72] V. Cerveny. Seismic rays and ray intensities in inhomogeneous anisotropic media. *Geophys. J. R. Astr. Soc.*, 29:1–13, 1972.

[CH62] R. Courant and D. Hilbert. *Methods of mathematical physics*, volume II. John Wiley-Sons, 1962.

[CL83] M. G. Crandall and P. L. Lions. Viscosity solutions of Hamilton-Jacobi equations. *Trans. Amer. Math. Soc.*, 277:1–42, 1983.

[CL84] M. G. Crandall and P. L. Lions. Two approximations of solutions of Hamilton-Jacobi equations. *Math. Comp.*, 43:1–19, 1984.

[CMP77] V. Cerveny, I. A. Molotkov, and I. Psencik. *Ray method in seismology.* Univerzita Karlova press, 1977.

[CN99] H. Chauris and M. Noble. 2-D velocity macro model estimation from seismic reflection data by local Differential Semblance Optimization: applications on synthetic and real data. In *Preprint.* Centre de Recherche en Geophysique, 1999.

[Coc98] B. Cockburn. A simple introduction to error estimation for nonlinear hyperbolic conservation laws. In *Preprint, School of Mathematics, University of Minnesota.* 1998.

[Cor83] S. Cornbleet. Geometrical optics reviewed: A new light on an old subject. *Proc. IEEE*, 71:471–502, 1983.

[CS98] A. Cherrett and S. Singh. Traveltime and polarisation tomography in 3-D anisotropic media. In *68th SEG Annual Internat. Mtg. Expanded Abstracts*, pages 1859–1862. Soc. Expl. Geophys., 1998.

[Del91] J. Dellinger. *Anisotropic Seismic Wave Propagation.* PhD thesis, Stanford University, Stanford, CA94305, 1991.

[dHB97] M. V. de Hoop and N. Bleistein. Generalized radon transform inversions for reflectivity in anisotropic elastic media. *Inverse Problems*, 13:669–690, 1997.

[dHSB99] M.V. de Hoop, C. Spencer, and R. Burridge. The resolving power of seismic amplitude data: An anisotropic inversion/migration approach. *Geophysics*, 64:852–873, 1999.

[DS83] J.E. Dennis, Jr. and R.B. Schnabel. *Numerical Methods for Unconstrained Optimization and Nonlinear Equations.* Prentice-Hall, Englewood Cliffs, 1983.

[DS97] J. Dellinger and W. W. Symes. Anisotropic finite-difference traveltimes using a Hamilton-Jacobi solver. In *67th SEG Annual Internat. Mtg. Expanded Abstracts*, pages 1786–1789. Soc. Expl. Geophys., 1997.

[DT95] W. Debski and A. Tarantola. Information on elastic parameters obtained from the amplitudes of reflected waves. *Geophysics*, 60:1426–1436, 1995.

[Eat93] D. Eaton. Finite difference traveltime calculation for anisotropic media. *Geophys. J. Int.*, 114:273–280, 1993.

[EM96] M. A. El-Mageed. *3D First arrival traveltimes and amplitudes via Eikonal and Transport Finite differences solvers.* PhD thesis, Department of Computational and Applied mathematics, Rice University, Houston, TX77251-1892, 1996.

[EMKS97] M. A. El-Mageed, S. Kim, and W. W. Symes. 3-D Kirchhoff migration using finite difference traveltimes and amplitudes. In *Annual Report. The Rice Inversion Project. (http://www.trip.caam.rice.edu/).* Rice University, 1997.

[Eva94] L. C. Evans. *Partial differential equations.* Berkeley Mathematics Lecture Notes, 1994.

[Fed68] F. I. Fedorov. *Theory of elastic waves in crystals.* Plenum press, 1968.

[FKN98] A. A. Fuki, Y. A. Kravtsov, and O. N. Naida. *Geometrical optics of weakly anisotropic media.* Gordon and Breach Science Publishers, 1998.

[Fri58] F. Friedlander. *Sound pulses.* Cambridge University Press, 1958.

[Gea71] C. W. Gear. *Numerical initial value problems in ordinary differential equations.* Englewood Cliffs, N. J.: Prentice-Hall, 1971.

[GM94] S. Gray and W. May. Kirchhoff migration using eikonal equation traveltimes. *Geophysics*, 59:810–817, 1994.

[GVL96] G. H. Golub and C. F. Van Loan. *Matrix computations.* Johns Hopkins University Press, 1996.

[HEOC87] A. Harten, B. Engquist, S. J. Osher, and S. Chakravarthy. Uniformly high order essentially non-oscillatory schemes, III. *J. Comput. Phys.*, 71:231–303, 1987.

[JP97] G. S. Jiang and D. P. Peng. Weighted ENO schemes for Hamilton-Jacobi equations. In *CAM97-29, UCLA*. 1997.

[JS96] G. S. Jiang and C. W. Shu. Efficient implementation of weighted ENO schemes. *J. Comput. Phys.*, 126:202–228, 1996.

[KC98] S. Kim and R. Cook. Second-order finite difference traveltimes in three dimensions. In *Annual Report, The Rice Inversion Project. (http://www.trip.caam.rice.edu/).* Rice University, 1998.

[KC99] S. Kim and R. Cook. 3-D traveltime computation using second-order ENO scheme. *Geophysics*, 64:1867–1876, 1999.

[Kim99] S. Kim. Eikonal solvers for anisotropic traveltimes. In *69th SEG Annual Internat. Mtg. Expanded Abstracts*, pages 1875–1878. Soc. Expl. Geophys., 1999.

[KL95] J. B. Keller and R. M. Lewis. Asymptotic methods for partial differential equations: the reduced wave equation and Maxwell's equations. *Surveys in Applied Mathematics*, 1:1–82, 1995.

[LeV90] R. J. LeVeque. *Numerical methods for conservation laws*. Birkhauser-Verlag, 1990.

[Lio82] P. L. Lions. *Generalized solutions of Hamilton-Jacobi equations*. Pitman Advanced Publishing Program, 1982.

[LOC94] X. D. Liu, S. J. Osher, and T. Chan. Weighted Essentially NonOscillatory schemes. *J. Comput. Phys.*, 115:200–212, 1994.

[LT98] C. T. Lin and E. Tadmor. L^1-stability and error estimates for approximate Hamilton-Jacobi solutions. In *CAM98-21, UCLA*. 1998.

[Mor89] P. Mora. Inversion = migration + tomography. *Geophysics*, 54:1575–1586, 1989.

[Mus70] M. J. P. Musgrave. *Crystal acoustics*. Holden-Day, 1970.

[OS88] S. J. Osher and J. A. Sethian. Fronts propagating with curvature dependent speed: algorithms based on Hamilton-Jacobi formulations. *J. Comput. Phys.*, 79:12–49, 1988.

[OS91] S. J. Osher and C. W. Shu. High-order Essentially NonOscillatory schemes for Hamilton-Jacobi equations. *SIAM J. Num. Anal.*, 28:907–922, 1991.

[PC92] R. Pratt and C. Chapman. Traveltime tomography in anisotropic media -II: Application. *Geophys. J. Int.*, 109:20–37, 1992.

[Per92] V. Pereyra. Two-point ray tracing in general 3-D media. *Geophysical Prospecting*, 40:267–287, 1992.

[QBS99] J. L. Qian, C. D. Belfi, and W. W. Symes. Adaptive finite difference method for traveltime and amplitude. In *69th SEG Annual Internat. Mtg. Expanded Abstracts*, pages 1763–1766. Soc. Expl. Geophys., 1999.

[QLO+92] F. Qin, Y. Luo, K. B. Olsen, W. Cai, and G. T. Schuster. Finite difference solution of the eikonal equation along expanding wavefronts. *Geophysics*, 57:478–487, 1992.

[QS93] F. Qin and G. T. Schuster. First-arrival traveltime calculation for anisotropic media. *Geophysics*, 58:1349–1358, 1993.

[RK86] M. Reshef and D. Kosloff. Migration of common shot gathers. *Geophysics*, 51:324–331, 1986.

[RMO99] S. J. Ruuth, B. Merriman, and S. J. Osher. A fixed grid method for capturing the motion of self-intersecting interfaces and related PDEs. In *CAM99-22, UCLA*. 1999.

[SB92] J. Stoer and R. Bulirsch. *Introduction to numerical analysis*. Springer-Verlag, New York, second edition, 1992.

[SC88] P. M. Shearer and C. H. Chapman. Ray tracing in anisotropic media with a linear gradient. *Geophysical Journal*, 94:575–580, 1988.

[SC91] W. W. Symes and J. J. Carazzone. Velocity inversion by differential semblance optimization. *Geophysics*, 56:654–663, 1991.

[Sch95] W. A. Jr. Schneider. Robust and efficient upwind finite-difference traveltime calculations in three dimensions. *Geophysics*, 60:1108–1117, 1995.

[Set99a] J. A. Sethian. Fast marching methods. *SIAM Review*, 41:199–235, 1999.

[Set99b] J. A. Sethian. *Level set methods*. Cambridge Univ. Press, second edition, 1999.

[SFW00] J. Steinhoff, M. Fan, and L. Wang. A new Eulerian method for the computation of propagating short acoustic and electromagnetic pulses. *J. Comput. Phys.*, 157:683–706, 2000.

[Shu97] C. W. Shu. Essentially non-oscillatory and weighted essentially non-oscillatory schemes for hyperbolic conservation laws. In *ICASE No.97-65, NASA Langley Research Center*. 1997.

[SK94] W. W. Symes and M. Kern. Inversion of reflection seismograms by differential semblance analysis: algorithm structures and synthetic examples. *Geophysical Prospecting*, 42:565–614, 1994.

[SP99] J. A. Sethian and A. M. Popovici. 3-D traveltime computation using the fast marching method. *Geophysics*, 64:516–523, 1999.

[SRBK92] W. A. Jr. Schneider, K. Ranzinger, A. Balch, and C. Kruse. A dynamic programming approach to first arrival traveltime computation in media with arbitrarily distributed velocities. *Geophysics*, 57:39–50, 1992.

[SVST94] W. W. Symes, R. Versteeg, A. Sei, and Q. H. Tran. Kirchhoff simulation, migration and inversion using finite difference traveltimes and amplitudes. In *Annual Report, The Rice Inversion Project. (http://www.trip.caam.rice.edu/)*. Rice University, 1994.

[Sym90] W. W. Symes. Velocity inversion: A case study in infinite-dimensional optimization. *Math. Programming*, 48:71–102, 1990.

[Sym95] W. W. Symes. Mathematics of reflection seismology. In *Annual Report, The Rice Inversion Project. (http://www.trip.caam.rice.edu/)*. Rice University, 1995.

[Tar86] A. Tarantola. A strategy for nonlinear elastic inversion of seismic reflection data. *Geophysics*, 51:1893–1903, 1986.

[Tay96] M. E. Taylor. *Partial differential equations: basic theory*. Springer, 1996.

[Tho86] L. Thomsen. Weak elastic anisotropy. *Geophysics*, 51:1954–1966, 1986.

[TT95] I. Tsvankin and L. Thomsen. Inversion of reflection traveltimes for transverse isotropy. *Geophysics*, 60:1095–1107, 1995.

[VH90] J. E. Vidale and H. Houston. Rapid calculation of seismic amplitudes. *Geophysics*, 55:1504–1507, 1990.

[Vid88] J. Vidale. Finite-difference calculation of travel times. *Bull., Seis. Soc. Am.*, 78:2062–2076, 1988.

[vTS91] J. van Trier and W. W. Symes. Upwind finite-difference calculation of traveltimes. *Geophysics*, 56:812–821, 1991.

[Whi99] B. S. White. Wave action on currents with vorticity. *J. Fluid Mech.*, 386:329–344, 1999.

[Zha93] L. Zhang. *Imaging by the wavefront propagation method*. PhD thesis, Stanford University, Stanford, CA94305, 1993.